

1

CAMPINAS STATE UNIVERSITY

2

DOCTORAL THESIS

3

---

4 **Search of Z and Higgs boson decaying into  $\Upsilon + \gamma$**   
5 **in pp collisions at CMS/LHC**

---

6

7 *Author:*

Felipe Torres da Silva de Araujo

*Supervisor:*

Dr. José Augusto Chinellato

*Co-Supervisor:*

Dr. Alberto Franco de Sá Santoro

8

*A thesis submitted in fulfillment of the requirements  
for the degree of Doctor of Physics*

9

*in the*

10

Graduate Program of  
"Gleb Wataghin" Institute of Physics

11

12

13

August 20, 2020

14 “Sometimes science is a lot more art than science. A lot of people don’t get that.”

15

Rick Sanchez

16 “Então, que seja doce. Repito todas as manhãs, ao abrir as janelas para deixar entrar o sol ou o  
17 cinza dos dias, bem assim, que seja doce. Quando há sol, e esse sol bate na minha cara amassada do  
18 sono ou da insônia, contemplando as partículas de poeira soltas no ar, feito um pequeno universo;  
19 repito sete vezes para dar sorte: que seja doce que seja doce que seja doce e assim por diante. Mas,  
20 se alguém me perguntasse o que deverá ser doce, talvez não saiba responder. Tudo é tão vago como  
21 se fosse nada.”

22

Caio Fernando Abreu

23 CAMPINAS STATE UNIVERSITY

24 *Abstract*

25 "Gleb Wataghin" Institute of Physics

26 Doctor of Physics

27 **Search of Z and Higgs boson decaying into  $\Upsilon + \gamma$  in pp collisions at CMS/LHC**

28 by Felipe Torres da Silva de Araujo

29 Searches for Standard Model Higgs and Z bosons decaying to a  $\Upsilon(1S, 2S, 3S)$  and a photon, with  
30 subsequent decay of the  $\Upsilon(1S, 2S, 3S)$  to  $\mu^+ \mu^-$  are presented. The analyses is performed using  
31 data recorded by CMS detector from proton-proton collisions at center-of-mass energy of 13 TeV  
32 corresponding to an integrated luminosity of  $35.86 \text{ fb}^{-1}$ . We put a limit, 95% confidence level, on  
33  $H \rightarrow \Upsilon(1S, 2S, 3S) + \gamma$  decay branching fraction at  $(6.8, 7.1, 6.0) \times 10^{-4}$  and on  $Z \rightarrow \Upsilon(1S, 2S, 3S) +$   
34  $\gamma$  decay branching fraction at  $(2.6, 2.3, 1.3) \times 10^{-6}$ . Contributions to operation, maintenance and  
35 R&D of Resistive Plate Chambers (RPC) of CMS are also presented. **EXPANDIR**

DRAFT

### *Acknowledgements*

<sup>37</sup> I would like to thank:

- 38 • the Campinas State University for providing the institutional support for this study;

39 • the Rio de Janeiro State University for the cooperation with Campinas State University in

40 their high-energy physics program. This was a key factor for this study;

41 • the National Council for Scientific and Technological Development (CNPq) for the financial

42 support for this work;

43 • the European Laboratory for Particle Physics (CERN) for the construction and operation of

44 the Large Hadron Collider (LHC);

45 • the Compact Muon Solenoid (CMS) collaboration for the construction, operation and provi-

46 sion of the instrumental means for this study.

DRAFT

# 47 Contents

48	<b>Abstract</b>	iii
49	<b>Acknowledgements</b>	v
50	<b>1 Introduction</b>	1
51	<b>2 Rare Z and Higgs decays to quarkonia</b>	3
52	2.1 Standard Model and Local Gauge Invariance . . . . .	3
53	2.2 Recent results . . . . .	6
54	<b>3 Experimental Setup</b>	9
55	3.1 Tracker . . . . .	9
56	3.2 Electromagnetic Calorimeter . . . . .	9
57	3.3 Hadronic Calorimeter . . . . .	9
58	3.4 Muon System . . . . .	10
59	3.4.1 DT . . . . .	10
60	3.4.2 CSC . . . . .	10
61	3.4.3 RPC . . . . .	10
62	3.4.4 GEN . . . . .	10
63	3.5 Trigger and Data Acquisition . . . . .	10
64	3.6 Simulation, reconstruction and computing . . . . .	10
65	3.7 Particle Flow Algorithm . . . . .	11
66	<b>4 Physics Analysis</b>	13
67	4.1 Datasets and simulated events . . . . .	13
68	4.1.1 Data samples . . . . .	13
69	4.1.2 Simulated datasets . . . . .	13
70	4.2 Contribution of the $\Upsilon(nS)$ polarisation . . . . .	15
71	4.3 Kinematical studies using MC generator . . . . .	16
72	4.4 Event selection . . . . .	20
73	4.5 Trigger and physics object selection (Group I) . . . . .	20
74	4.5.1 Trigger . . . . .	20
75	4.5.2 Muon Identification . . . . .	20
76	4.5.3 Photon Identification . . . . .	22
77	4.5.4 Kinematical distributions . . . . .	22
78	4.6 Kinematical selection (Group II) . . . . .	32
79	4.7 Event categorization and yields . . . . .	40
80	4.7.1 R9 reweighting . . . . .	40
81	4.7.2 Event counting and yields . . . . .	40
82	4.8 Background modeling . . . . .	42
83	4.9 Signal modeling . . . . .	49
84	4.10 Systematic uncertainties . . . . .	55
85	4.10.1 Uncertainties on the predicted yields . . . . .	55

86	4.10.2 Uncertainties that affect the signal fits . . . . .	56
87	4.11 Modeling Cross checks . . . . .	59
88	<b>5 Results and conclusion</b>	<b>65</b>
89	5.1 The $CL_s$ formalism for upper limits setting at CMS . . . . .	65
90	5.2 Branching fraction upper limits . . . . .	67
91	<b>6 CMS Resistive Plate Chambers - RPC</b>	<b>71</b>
92	6.1 Resistive Plate Chambers . . . . .	71
93	6.1.1 Principles and operation modes . . . . .	71
94	6.2 CMS Resistive Plate Chambers . . . . .	73
95	6.2.1 Performance . . . . .	75
96	6.3 Contribution to the CMS RPC project . . . . .	78
97	6.3.1 RPC Operation - Shifts and Data Certification . . . . .	78
98	6.4 RPC Online Software . . . . .	79
99	6.4.1 iRPC R&D . . . . .	80
100	6.4.2 LS2 and the RPC Standard Maintenance . . . . .	86
101	HV maintenance . . . . .	86
102	LV and control maintenance . . . . .	87
103	Detector commissioning . . . . .	88
104	<b>7 Conclusion</b>	<b>91</b>
105	<b>Bibliography</b>	<b>93</b>

# <sup>106</sup> List of Figures

<sup>107</sup>	2.1	Elementary particles of the Standard Model, with their masses charges and spin. Those particles can be divided in two classes: boson (the interaction/force carriers) and the fermions, which are divided in three generations. Source: [1]. . . . .	<sup>110</sup>	4
<sup>111</sup>	2.2	Example of leading order diagrams for the indirect (top) and direct (bottom) production mechanisms. In the diagrams, the h can also be understood as a Z boson. . . . .	<sup>112</sup>	6
<sup>113</sup>	2.3	Expected relative variation of the branching ratio for the $H \rightarrow \Upsilon(nS) + \gamma$ to $k_b$ , where $k_b = g(Hb\bar{b})/g(Hb\bar{b})_{SM}$ is the ratio for the observed and expected Yukawa coupling oh $Hb\bar{b}$ . [6] . . . . .	<sup>114</sup>	7
<sup>115</sup>	4.1	Distributions of $\cos\theta$ of $\Upsilon \rightarrow \mu\mu$ and $\gamma^* \rightarrow \mu\mu$ The orange distribution is the $Z \rightarrow \Upsilon(1S, 2S, 3S) + \gamma$ sample before reweighting (Unpolarized); the blue and gray distributions are $Z \rightarrow \Upsilon(1S, 2S, 3S)$ sample after reweighting, for the Transverse and Longitudinal Polarization. . . . .	<sup>116</sup>	16
<sup>117</sup>	4.2	Generator level distributions of main variables for $Z \rightarrow \Upsilon(1S, 2S, 3S) + \gamma$ : Transverse momenta of the leading/trailing $p_T$ muon and the photon, pseudorapidity ( $\eta$ ) and $\phi$ of the muons and the photon, distances $\Delta R$ between the two muons and between the muons and the photon. All the distributions shown in the figure are normalized to the unity of area. . . . .	<sup>118</sup>	18
<sup>119</sup>	4.3	Generator level distributions of main variables for $H \rightarrow \Upsilon(1S, 2S, 3S) + \gamma$ : Transverse momenta of the leading/trailing $p_T$ muon and the photon, pseudorapidity ( $\eta$ ) and $\phi$ of the muons and the photon, distances $\Delta R$ between the two muons and between the muons and the photon. All the distributions shown in the figure are normalized to the unity of area. . . . .	<sup>120</sup>	19
<sup>121</sup>	4.4	The $p_T$ muon distributions from data and signal events for Z decaying in $\Upsilon(1S, 2S, 3S) + \gamma$ after Group I of selection cuts, where on left are presenting the trailing muons and on right are the leading muons. The plots are normalized to the unit of area. . . . .	<sup>122</sup>	23
<sup>123</sup>	4.5	The $\eta$ muon distributions from data and signal events of Z decaying in $\Upsilon(1S, 2S, 3S) + \gamma$ after Group I of selection cuts, where on left are presenting the trailing muons and on right are the leading muons. The plots are normalized to the unit of area. . . . .	<sup>124</sup>	23
<sup>125</sup>	4.6	The $\phi$ muon distributions from data and signal events of Z decaying in $\Upsilon(1S, 2S, 3S) + \gamma$ after Group I of selection cuts, where on left are presenting the trailing muons and on right are the leading muons. The plots are normalized to the unit of area. . . . .	<sup>126</sup>	23
<sup>127</sup>	4.7	The $p_T$ photon distributions from data and signal events for Z decaying in $\Upsilon(1S, 2S, 3S) + \gamma$ Group I of selection cuts. The plots normalized to the unit of area. . . . .	<sup>128</sup>	24
<sup>129</sup>	4.8	The $\eta$ photon distributions from data and signal events of Z decaying in $\Upsilon(1S, 2S, 3S) + \gamma$ after Group I of selection cuts. The plot is normalized to the unit of area. . . . .	<sup>130</sup>	24
<sup>131</sup>	4.9	The $\phi$ photon distributions from data and signal events of Z decaying in $\Upsilon(1S, 2S, 3S) + \gamma$ after Group I of selection cuts. The plot is normalized to the unit of area. . . . .	<sup>132</sup>	24
<sup>133</sup>	4.10	The $p_T$ distributions for the reconstructed $\Upsilon(1S, 2S, 3S)$ in the left and for Z in the right from data and signal events for Z decaying in $\Upsilon(1S, 2S, 3S) + \gamma$ after Group I of selection cuts. The plots are normalized to the unit of area. . . . .	<sup>134</sup>	25

147	4.11 The $\eta$ distributions for $\Upsilon(1S, 2S, 3S)$ in the left and for Z in the right from data and signal events for Z decaying in $\Upsilon(1S, 2S, 3S) + \gamma$ after Group I of selection cuts. The plots are normalized to the unit of area. . . . .	25
148		
149		
150	4.12 The $\phi$ distributions for $\Upsilon(1S, 2S, 3S)$ in the left and for Z in the right from data and signal events for Z decaying in $\Upsilon(1S, 2S, 3S) + \gamma$ after Group I of selection cuts. The plots are normalized to the unit of area. . . . .	25
151		
152		
153	4.13 The $\Delta R$ distributions between the photon and the leading muon (left) and the trailing muon (right) for for Z decaying in $\Upsilon(1S, 2S, 3S) + \gamma$ from data and signal events after Group I of selection cuts. The plots are normalized to the unit of area. . . . .	26
154		
155		
156	4.14 Left: The $\Delta R$ distributions between reconstructed dimuon ( $\mu\mu$ ) system and the photon. Right: absolute value of the $\Delta\phi$ between the leading muon and the photon for for Z decaying in $\Upsilon(1S, 2S, 3S) + \gamma$ from data and signal events after Group I of selection cuts. The plots are normalized to the unit of area. . . . .	26
157		
158		
159		
160	4.15 The ratio for the transverse momentum of the reconstructed Upsilon and the reconstructed Z mass ( $p_T^{\mu\mu}/M_{\mu\mu\gamma}$ - left) and the ratio for the transverse energy of the reconstructed Photon and the reconstructed Z mass ( $E_T^{\mu\mu}/M_{\mu\mu\gamma}$ - right) distribution for Z decaying in $\Upsilon(1S, 2S, 3S) + \gamma$ from data and signal events after Group I of selection cuts. The plots are normalized to the unit of area. . . . .	26
161		
162		
163		
164		
165	4.16 The dimuon mass distribution of the reconstructed $\Upsilon(1S, 2S, 3S)$ from data and signal events for Z decaying after Group I of selection cuts. The plot is normalized to the number of events. "Signal" stands for the $Z \rightarrow \Upsilon(1S, 2S, 3S) + \gamma$ sample (scaled by a factor of $\times 100$ ) and "Background" corresponds to the peaking background ( $Z \rightarrow \mu\mu\gamma_{FSR}$ ) sample (scaled by a factor of x3). . . . .	27
166		
167		
168		
169		
170	4.17 The $p_T$ muon distributions from data and signal events for Higgs decaying in $\Upsilon(1S, 2S, 3S) + \gamma$ after Group I of selection cuts, where on left are presenting the trailing muons and on right are the leading muons. The plots are normalized to the unit of area. . . . .	27
171		
172		
173	4.18 The $\eta$ muon distributions from data and signal events of Higgs decaying in $\Upsilon(1S, 2S, 3S) + \gamma$ after Group I of selection cuts, where on left are presenting the trailing muons and on right are the leading muons. The plots are normalized to the unit of area. . . . .	27
174		
175		
176		
177	4.19 The $\phi$ muon distributions from data and signal events of Higgs decaying in $\Upsilon(1S, 2S, 3S) + \gamma$ after Group I of selection cuts, where on left are presenting the trailing muons and on right are the leading muons. The plots are normalized to the unit of area. . . . .	27
178		
179		
180	4.20 The $p_T$ photon distributions from data and signal events for Higgs decaying in $\Upsilon(1S, 2S, 3S) + \gamma$ Group I of selection cuts. The plot is normalized to the unit of area. . . . .	28
181		
182		
183	4.21 The $\eta$ photon distributions from data and signal events of Higgs decaying in $\Upsilon(1S, 2S, 3S) + \gamma$ after Group I of selection cuts. The plot is normalized to the unit of area. . . . .	28
184		
185	4.22 The $\phi$ photon distributions from data and signal events of Higgs decaying in $\Upsilon(1S, 2S, 3S) + \gamma$ after Group I of selection cuts. The plot is normalized to the unit of area. . . . .	29
186		
187	4.23 The $p_T$ distributions for $\Upsilon(1S, 2S, 3S)$ in the left and for Higgs in the right from data and signal events for Higgs decaying in $\Upsilon(1S, 2S, 3S) + \gamma$ after Group I of selection cuts. The plots are normalized to the unit of area. . . . .	29
188		
189	4.24 The $\eta$ distributions for $\Upsilon(1S, 2S, 3S)$ in the left and for Higgs in the right from data and signal events for Higgs decaying in $\Upsilon(1S, 2S, 3S) + \gamma$ after Group I of selection cuts. The plots are normalized to the unit of area. . . . .	29
190		
191		
192	4.25 The $\phi$ distributions for $\Upsilon(1S, 2S, 3S)$ in the left and for Higgs in the right from data and signal events for Higgs decaying in $\Upsilon(1S, 2S, 3S) + \gamma$ after Group I of selection cuts. The plots are normalized to the unit of area. . . . .	30
193		
194		
195	4.26 The $\Delta R$ distributions between the photon and the leading muon (left) and the trailing muon (right) for Higgs decaying in $\Upsilon(1S, 2S, 3S) + \gamma$ from data and signal events after Group I of selection cuts. The plots are normalized to the unit of area. . . . .	30
196		
197		

198	4.27 Left: The $\Delta R$ distributions between reconstructed dimuon ( $\mu\mu$ ) system and the photon. Right: absolute value of the $\Delta\phi$ between the leading muon and the photon for Higgs decaying in $\Upsilon(1S, 2S, 3S) + \gamma$ from data and signal events after Group I of selection cuts. The plots are normalized to the unit of area. . . . .	30
202	4.28 The ratio for the transverse momentum of the reconstructed Upsilon and the reconstructed Higgs mass ( $p_T^{\mu\mu}/M_{\mu\mu\gamma}$ - left) and the ratio for the transverse energy of the reconstructed Photon and the reconstructed Higgs mass ( $E_T^{\mu\mu}/M_{\mu\mu\gamma}$ - right) distribution for Higgs decaying in $\Upsilon(1S, 2S, 3S) + \gamma$ from data and signal events after Group I of selection cuts. The plots are normalized to the unit of area. . . . .	31
206	4.29 The dimuon mass distribution of the reconstructed $\Upsilon(1S, 2S, 3S)$ from data and signal events for Higgs decaying after Group I of selection cuts. This plot is normalized the expected number of events. The plot is normalized to the number of events. "Signal" stands for the $H \rightarrow \Upsilon(1S, 2S, 3S) + \gamma$ sample (scaled by a factor of $\times 60000$ ) and "Background" corresponds to the peaking background (Higgs Dalitz Decay) sample (scaled by a factor of $\times 400$ ). . . . .	31
210	4.30 The $p_T$ muon distributions from data and signal events for Z decaying in $\Upsilon(1S, 2S, 3S) + \gamma$ after Group I of selection cuts, where on left are presenting the trailing muons and on right are the leading muons. The plots are normalized to the number of events. Signal sample is scaled by a factor of $\times 100$ . . . . .	32
214	4.31 The $\eta$ muon distributions from data and signal events of Z decaying in $\Upsilon(1S, 2S, 3S) + \gamma$ after Group I of selection cuts, where on left are presenting the trailing muons and on right are the leading muons. The plots are normalized to the number of events. Signal sample is scaled by a factor of $\times 100$ . . . . .	33
218	4.32 The $\phi$ muon distributions from data and signal events of Z decaying in $\Upsilon(1S, 2S, 3S) + \gamma$ after Group I of selection cuts, where on left are presenting the trailing muons and on right are the leading muons. The plots are normalized to the number of events. Signal sample is scaled by a factor of $\times 100$ . . . . .	33
222	4.33 The $p_T$ photon distributions from data and signal events for Z decaying in $\Upsilon(1S, 2S, 3S) + \gamma$ all (Group I+II) selection cuts. The plot is normalized to the number of events. Signal sample is scaled by a factor of $\times 100$ . . . . .	33
226	4.34 The $\eta$ photon distributions from data and signal events of Z decaying in $\Upsilon(1S, 2S, 3S) + \gamma$ after all (Group I+II) selection cuts. The plot is normalized to the number of events. Signal sample is scaled by a factor of $\times 100$ . . . . .	34
230	4.35 The $\phi$ photon distributions from data and signal events of Z decaying in $\Upsilon(1S, 2S, 3S) + \gamma$ after all (Group I+II) selection cuts. The plot is normalized to the number of events. Signal sample is scaled by a factor of $\times 100$ . . . . .	34
234	4.36 The $p_T$ distributions for $\Upsilon(1S, 2S, 3S)$ in the left and for Z in the right from data and signal events for Z decaying in $\Upsilon(1S, 2S, 3S) + \gamma$ after all (Group I+II) selection cuts. The plots are normalized to the number of events. Signal sample is scaled by a factor of $\times 100$ . . . . .	34
238	4.37 The $\eta$ distributions for $\Upsilon(1S, 2S, 3S)$ in the left and for Z in the right from data and signal events for Z decaying in $\Upsilon(1S, 2S, 3S) + \gamma$ after all (Group I+II) selection cuts. The plots are normalized to the number of events. Signal sample is scaled by a factor of $\times 100$ . . . . .	35
242	4.38 The $\phi$ distributions for $\Upsilon(1S, 2S, 3S)$ in the left and for Z in the right from data and signal events for Z decaying in $\Upsilon(1S, 2S, 3S) + \gamma$ after all (Group I+II) selection cuts. The plots are normalized to the number of events. Signal sample is scaled by a factor of $\times 100$ . . . . .	35

246	4.39 The $\Delta R$ distributions between the photon and the leading muon (left) and the trailing 247 muon (right) for $\Upsilon(1S, 2S, 3S)$ from data and signal events for Z decaying after all 248 (Group I+II) selection cuts. The plots are normalized to the number of events. Signal 249 sample is scaled by a factor of $\times 100$ ) . . . . .	35
250	4.40 The ratio for the transverse momentum of the reconstructed Upsilon and the re- 251 constructed Z mass ( $p_T^{\mu\mu}/M_{\mu\mu\gamma}$ - left) and the ratio for the transverse energy of the 252 reconstructed Photon and the reconstructed Z mass ( $E_T^{\mu\mu}/M_{\mu\mu\gamma}$ - right) distribution 253 for $\Upsilon(1S, 2S, 3S)$ from data and signal events for Z decaying after all (Group I+II) 254 selection cuts. The plots are normalized to the number of events. Signal sample is 255 scaled by a factor of $\times 100$ ) . . . . .	36
256	4.41 The $p_T$ muon distributions from data and signal events for Higgs decaying in $\Upsilon(1S, 2S, 3S)$ 257 + $\gamma$ after Group I of selection cuts, where on left are presenting the trailing muons 258 and on right are the leading muons. The plots are normalized to the number of 259 events. Signal sample is scaled by a factor of $\times 600000$ ) . . . . .	36
260	4.42 The $\eta$ muon distributions from data and signal events of Higgs decaying in $\Upsilon(1S, 2S, 3S)$ 261 + $\gamma$ after Group I of selection cuts, where on left are presenting the trailing muons 262 and on right are the leading muons. The plots are normalized to the number of 263 events. Signal sample is scaled by a factor of $\times 600000$ ) . . . . .	36
264	4.43 The $\phi$ muon distributions from data and signal events of Higgs decaying in $\Upsilon(1S, 2S, 3S)$ 265 + $\gamma$ after Group I of selection cuts, where on left are presenting the trailing muons 266 and on right are the leading muons. The plots are normalized to the number of 267 events. Signal sample is scaled by a factor of $\times 600000$ ) . . . . .	37
268	4.44 The $p_T$ photon distributions from data and signal events for Higgs decaying in 269 $\Upsilon(1S, 2S, 3S) + \gamma$ all (Group I+II) selection cuts. The plot is normalized to the 270 number of events. Signal sample is scaled by a factor of $\times 600000$ ) . . . . .	37
271	4.45 The $\eta$ photon distributions from data and signal events of Higgs decaying in $\Upsilon(1S, 2S, 3S)$ 272 + $\gamma$ after all (Group I+II) selection cuts. The plot is normalized to the number of 273 events. Signal sample is scaled by a factor of $\times 600000$ ) . . . . .	37
274	4.46 The $\phi$ photon distributions from data and signal events of Higgs decaying in $\Upsilon(1S, 2S, 3S)$ 275 + $\gamma$ after all (Group I+II) selection cuts. The plot is normalized to the number of 276 events. Signal sample is scaled by a factor of c) . . . . .	38
277	4.47 The $p_T$ distributions for $\Upsilon(1S, 2S, 3S)$ in the left and for Higgs in the right from 278 data and signal events for Higgs decaying in $\Upsilon(1S, 2S, 3S) + \gamma$ after all (Group I+II) 279 selection cuts. The plots are normalized to the number of events. Signal sample is 280 scaled by a factor of $\times 600000$ ) . . . . .	38
281	4.48 The $\eta$ distributions for $\Upsilon(1S, 2S, 3S)$ in the left and for Higgs in the right from data 282 and signal events for Higgs decaying in $\Upsilon(1S, 2S, 3S) + \gamma$ after all (Group I+II) 283 selection cuts. The plots are normalized to the number of events. Signal sample is 284 scaled by a factor of $\times 600000$ ) . . . . .	38
285	4.49 The $\phi$ distributions for $\Upsilon(1S, 2S, 3S)$ in the left and for Higgs in the right from data 286 and signal events for Higgs decaying in $\Upsilon(1S, 2S, 3S) + \gamma$ after all (Group I+II) 287 selection cuts. The plots are normalized to the number of events. Signal sample is 288 scaled by a factor of $\times 600000$ ) . . . . .	39
289	4.50 The $\Delta R$ distributions between the photon and the leading muon (left) and the trailing 290 muon (right) for $\Upsilon(1S, 2S, 3S)$ from data and signal events for Higgs decaying after 291 all (Group I+II) selection cuts. The plots are normalized to the number of events. 292 Signal sample is scaled by a factor of $\times 600000$ ) . . . . .	39

293	4.51 The ratio for the transverse momentum of the reconstructed Upsilon and the re-	
294	constructed Higgs mass ( $p_T^{\mu\mu}/M_{\mu\mu\gamma}$ - left) and the ratio for the transverse energy	
295	of the reconstructed Photon and the reconstructed Higgs mass ( $E_T^{\mu\mu}/M_{\mu\mu\gamma}$ - right)	
296	distribution for $\Upsilon(1S, 2S, 3S)$ from data and signal events for Higgs decaying after	
297	all (Group I+II) selection cuts. The plots are normalized to the number of events.	
298	Signal sample is scaled by a factor of $\times 600000$ ). . . . .	39
299	4.52 Data and MC of the R9 variable, before and after the reweighting. Barrel (left) and	
300	Endcap (right). . . . .	40
301	4.53 Peaking background for the $Z \rightarrow \Upsilon(1S, 2S, 3S) + \gamma$ analysis. $\mu\mu$ mass distribution	
302	(left) and $\mu\mu\gamma$ invariant mass distribution (right). From top to bottom categories:	
303	Inclusive, EB High R9, EB Low R9, EE. . . . .	44
304	4.54 $\Upsilon$ control sample fit with Chebychev 1 <sup>st</sup> order for the background support and 3	
305	gaussian for the three $\Upsilon(1S, 2S, 3S)$ peaks. . . . .	45
306	4.55 $Z \rightarrow \Upsilon(1S, 2S, 3S) + \gamma$ Background Modeling: $\mu\mu$ distribution. Inclusive (top left);	
307	EB High R9 (top right), EB Low R9 (bottom left), EE (bottom right). The pdfs	
308	projections are plotted with respect to the overall best choice of the statistica test. .	47
309	4.56 $Z \rightarrow \Upsilon(1S, 2S, 3S) + \gamma$ Background Modeling: $\mu\mu\gamma$ distribution. Inclusive (top left);	
310	EB High R9 (top right), EB Low R9 (bottom left), EE (bottom right). The plotted	
311	<i>pdfs</i> corresponds to the best choice by the statistical test for each family. The signal	
312	region, from 80 GeV to 100 GeV was blinded. . . . .	47
313	4.57 Peaking Background for the $H \rightarrow \Upsilon(1S, 2S, 3S) + \gamma$ analysis. $m_{\mu\mu}$ invariant mass	
314	distribution (left) and $m_{\mu\mu\gamma}$ invariant mass distribution (right). . . . .	48
315	4.58 $H \rightarrow \Upsilon(1S, 2S, 3S) + \gamma$ Background Modeling: $m_{\mu\mu}$ distribution. The <i>pdfs</i> projections	
316	are plotted with respect to the overall best choice of the statistical test. . . . .	48
317	4.59 $H \rightarrow \Upsilon(1S, 2S, 3S) + \gamma$ Background Modeling: $\mu\mu\gamma$ distribution. The plotted <i>pdfs</i>	
318	corresponds to the best choice by the statistical test for each family. The signal	
319	region, from 115 GeV to 135 GeV was blinded. . . . .	48
320	4.60 Signal Modeling for the $Z \rightarrow \Upsilon(1S, 2S, 3S) + \gamma$ analysis for Inclusive category. $m_{\mu\mu}$	
321	mass distribution (left) and $m_{\mu\mu\gamma}$ mass distribution (right). From top to bottom:	
322	$\Upsilon(1S)$ , $\Upsilon(2S)$ , $\Upsilon(3S)$ . . . . .	50
323	4.61 Signal Modeling for the $Z \rightarrow \Upsilon(1S, 2S, 3S) + \gamma$ analysis for EB High R9 category.	
324	$m_{\mu\mu}$ mass distribution (left) and $m_{\mu\mu\gamma}$ mass distribution (right). From top to bottom:	
325	$\Upsilon(1S)$ , $\Upsilon(2S)$ , $\Upsilon(3S)$ . . . . .	51
326	4.62 Signal Modeling for the $Z \rightarrow \Upsilon(1S, 2S, 3S) + \gamma$ analysis for EB Low R9 category.	
327	$m_{\mu\mu}$ mass distribution (left) and $m_{\mu\mu\gamma}$ mass distribution (right). From top to bottom:	
328	$\Upsilon(1S)$ , $\Upsilon(2S)$ , $\Upsilon(3S)$ . . . . .	52
329	4.63 Signal Modeling for the $Z \rightarrow \Upsilon(1S, 2S, 3S) + \gamma$ analysis for EE category. $m_{\mu\mu}$ mass	
330	distribution (left) and $m_{\mu\mu\gamma}$ mass distribution (right). From top to bottom: $\Upsilon(1S)$ ,	
331	$\Upsilon(2S)$ , $\Upsilon(3S)$ . . . . .	53
332	4.64 Signal Modeling for the $H \rightarrow \Upsilon(1S, 2S, 3S) + \gamma$ . $m_{\mu\mu}$ mass distribution (left) and	
333	$m_{\mu\mu\gamma}$ mass distribution (right). From top to bottom: $\Upsilon(1S)$ , $\Upsilon(2S)$ , $\Upsilon(3S)$ . . . . .	54
334	4.65 Examples of the toy datasets fit ( $M_{\mu\mu}$ ), for the Z decay analysis, after the toy dataset	
335	refit, for 1S, 2S and 3S (left to right), with $\mu_{true}$ equals to 20, 50, 100, 1000 (top to	
336	bottom). The red lines corresponds to the background model (B), the green lines to	
337	signal model (S), the blue lines to the total (S+B) and the dots is the toy dataset. .	59
338	4.66 Examples of the toy datasets fit ( $M_{\mu\mu\gamma}$ ), for the Z decay analysis, after the toy dataset	
339	refit, for 1S, 2S and 3S (left to right), with $\mu_{true}$ equals to 20, 50, 100, 1000 (top to	
340	bottom). The red lines corresponds to the background model (B), the green lines to	
341	signal model (S), the blue lines to the total (S+B) and the dots is the toy dataset. .	60

342	4.67 Examples of the toy datasets fit ( $M_{\mu\mu}$ ), for the Higgs decay analysis, after the toy dataset refit, for 1S, 2S and 3S (left to right), with $\mu_{true}$ equals to 100000, 200000, 300000, 1000000 (top to bottom). The red lines corresponds to the background model (B), the green lines to signal model (S), the blue lines to the total (S+B) and the dots is the toy dataset. . . . .	61
347	4.68 Examples of the toy datasets fit ( $M_{\mu\mu\gamma}$ ), for the Higgs decay analysis, after the toy dataset refit, for 1S, 2S and 3S (left to right), with $\mu_{true}$ equals to 100000, 200000, 300000, 1000000 (top to bottom). The red lines corresponds to the background model (B), the green lines to signal model (S), the blue lines to the total (S+B) and the dots is the toy dataset. . . . .	62
352	4.69 Distribution of pulls ( $\frac{\mu_{fit} - \mu_{true}}{\sigma_{fit}}$ ), for the Z decay analysis, after the toy dataset refit, for 1S, 2S and 3S (left to right), with $\mu_{true}$ equals to 20, 50, 100, 1000 (top to bottom). . . . .	63
357	4.70 Distribution of pulls ( $\frac{\mu_{fit} - \mu_{true}}{\sigma_{fit}}$ ), for the Higgs decay analysis, after the toy dataset refit, for 1S, 2S and 3S (left to right), with $\mu_{true}$ equals to 100000, 200000, 300000, 1000000 (top to bottom). . . . .	64
358	5.1 Example of $f(\tilde{q}_\mu   \mu, \hat{\theta}_\mu^{\text{obs}})$ $f(\tilde{q}_\mu   \mu = 0, \hat{\theta}_{\mu=0}^{\text{obs}})$ distributions generated with toy MC. Source: [76]. . . . .	67
360	5.2 Example of $f(\tilde{q}_\mu   \mu, \hat{\theta}_\mu^{\text{obs}})$ $f(\tilde{q}_\mu   \mu = 0, \hat{\theta}_{\mu=0}^{\text{obs}})$ distributions generated with toy MC. In the figure, $q$ must be read as $\tilde{q}$ . The green area shows the $p_{s+b}$ defined in 5.7, while the yellow one shows $p_b$ defined in 5.8. Source: [73]. . . . .	68
362	6.1 The Avalanche production process inside a RPC gap. (Top) The initial process and the secondary electron/ion generation. (Bottom) The overall charge distribution of an Avalanche between the electrodes. Source: [80]. . . . .	72
364	6.2 Streamer formation process. The distorted electric field around the high positive charge concentration enhances the ionization process, initiating secondary avalanches. Source: [80]. . . . .	73
366	6.3 RPC chamber on installed on station RE+4 of CMS Endcap. Source: [83]. . . . .	74
368	6.4 R- $\phi$ (left) and R-Z (right) projections of the barrel Muon System. . . . .	75
370	6.5 R-Z projections of the endcap Muon System (positive Z side). This is the same configuration for the 36 $\phi$ sectors. . . . .	76
372	6.6 RPC efficiencies (per chamber) over Run2 Integrated Luminosity for Barrel (left) and Endcap (right). Red lines indicates technical stops (TS) while grey ones indicates Year-End-Technical stops (YETS). The drop in the efficiency around $110 \text{ pb}^{-1}$ is related to a known operation mistake. Source: [94]. . . . .	77
374	6.7 RPC cluster size (CLS - per chamber) over Run2 Integrated Luminosity for Barrel (left) and Endcap (right). Red lines indicates technical stops (TS) while grey ones indicates Year-End-Technical stops (YETS). The drop in the cluster size around $110 \text{ pb}^{-1}$ is related to a known operation mistake. Source: [94]. . . . .	77
376	6.8 Ohmic current history of W+0, RE+1, RE+4 and RE-4. The blank regions, from time to time, corresponds to technical stops (TS), when the detector is off. Source: [94]. . . . .	78
378	6.9 (a) Luminosity delivered by the LHC, recorded one by CMS and the certified (validated), from the 22nd of April, 2016 to the 27th of October, 2016. (b) Efficiency of the certification process for each subsystem, from the 22nd of April, 2016 to the 27th of October, 2016. Total CMS efficiency is above 90%. Source: [95]. . . . .	79
380	6.10 Upgrade of the RPC online software. . . . .	80
382	6.11 Example of the updated screens, using Trigger Supervisor 5. . . . .	80
384	6.12 $\eta$ projection of the Muon System subdetectors. In purple, is labeled the iRPCS to be installed during the CMS upgrade. . . . .	81

390	6.13 FEB configured 8 channels modes. Group should be understood as wire pad. Left:	82
391	Logical diagram for OR2. Right: Logical diagram for AND2. . . . .	
392	6.14 FEB configured 2 channels modes. Left: Logical diagram for OR8. Group should be	
393	understood as wire pad. Right: Logical diagram for OR4AND2. . . . .	83
394	6.15 Left: Setup mounted for commissioning. Two MWPC chamber on the top (chambers	
395	A and B) and two (chambers C and D) on the bottom with a RPC R&D in the	
396	middle. Right: Rack with all the services for the operation of these chambers. . . . .	84
397	6.16 Coincidence rate of two chambers with respect to an arbitrary distance between	
398	the two top planes. Measured in 10 minutes, for 2 logical combinations (OR8 and	
399	OR4AND2). Applied high voltage: 2.65 kV. Threshold: 7 pC. Active area: readout	
400	of 160 mm x 160 mm per chamber. . . . .	85
401	6.17 Individual rates (chambers A, B, C and D) and coincidence rates for two chambers	
402	(A AND B, C AND D), for without $\gamma$ source (blue), a shielded $\gamma$ source (orange) and	
403	an unshielded $\gamma$ source (green). Source sitting on top of chamber A. Applied high	
404	voltage: 2.65 kV. Threshold: 7 pC. Active area: readout of 160 mm x 320 mm per	
405	chamber. Logical combination: AND2 . . . . .	85
406	6.18 Left: Proposed adapter the chamber patch panel which make it possible to replace	
407	a tripolar by a jupiter HV connector. Right: Try out of the proposed HV connector	
408	replacement. . . . .	87
409	6.19 RPC Front-end board (FEB) used in the barrel chambers. . . . .	88
410	6.20 RPC FEB Commissioning Analyzer. . . . .	89

DRAFT

# List of Tables

412    2.1	Relative strength (with respect to the strong force) and effective range of action for the four fundamentals interactions. . . . .	3
413    2.2	Summary of cross section and branching ratio for $H/Z \rightarrow \Upsilon(1S, 2S, 3S) + \gamma \rightarrow \mu^+ \mu^- + \gamma$ analysis. The effective cross-section will be discussed in section 4.1.2. . . . .	5
414    2.3	Observed upper limits, by the ATLAS experiment, on the branching fractions for the Higgs and Z decays (last result). Detailed comparisons with the results obtained in this study will be presented in chapter 5. . . . .	7
415    2.4	Observed upper limits, by CMS, on the branching fractions for the Higgs and Z decays. The number are compatible with the ones obtained by ATLAS. The results presented for different polarization scenarios of the $J/\Psi$ . . . . .	8
422    4.1	Datasets simulated (MC) for 2016 conditions. Assuming that $\sigma(pp \rightarrow H)$ , taking into consideration all the simulated Higgs production modes, is 55.13 pb [44] and $\sigma(pp \rightarrow$ $Z \rightarrow \mu\mu)$ is 57094.5 pb, including the next-to-next-to-leading order (NNLO) QCD contributions, and the next-to-leading order (NLO) electroweak corrections from fewz 3.1 [45] calculated using the NLO PDF set NNPDF3.0, with the phase space selection in invariant mass of the dimuon system of $m_{\mu\mu} > 50$ GeV. For the Higgs Dalitz $\sigma$ , we consider only the gluon fusion contribution ( $\sigma_{ggF} = 48.6$ pb) [44]. The Higgs Dalitz Decay $BR_{SM}$ and the $Z \rightarrow \mu\mu\gamma_{FSR}$ were obtained with MCFM 6.6 [46] (as in the CMS search for Higgs Dalitz Decay in at $\sqrt{s} = 8$ TeV [47]) and with MADGRAPH 5 _MC@NLO, respectively. The $BR_{\Upsilon(1S, 2S, 3S) \rightarrow \mu\mu}^{PDG} = (2.48, 1.93, 2.18) \times 10^{-2}$ is quoted from Particle Data Group report (PDG) [2]. The "Effective $\sigma$ " for the signal samples is $\sigma(pp \rightarrow Z(H)) \times BR_{SM} \times BR_{\Upsilon(nS) \rightarrow \mu\mu}^{PDG}$ . . . . .	15
434    4.2	Summary of the impact of reweighted of polarization contribution using several sce- narios. . . . .	16
436    4.3	Conditions for a muon to pass the strict tracker requirements. . . . .	21
437    4.4	Number of events for the Z decay, before and after the full selection, per categorization scenarios. . . . .	41
439    4.5	Number of events for the H decay, before and after the full selection. . . . .	41
440    4.6	Modeling for each background source and mass component. . . . .	42
441    4.7	Modeling for each signal source and mass component. . . . .	49
443    4.8	A summary table of systematic uncertainties in the Z boson decaying in $\Upsilon(1S, 2S, 3S) +$ $\gamma$ , affecting the final yields of the MC samples. . . . .	57
444    4.9	A summary table of systematic uncertainties in the Higgs boson decaying in $\Upsilon(1S, 2S, 3S) +$ $\gamma$ , affecting the final yields of the MC samples. . . . .	58
446    4.10	A summary table of systematic uncertainties in the Z (H) decaying in $\Upsilon(1S, 2S, 3S) +$ $\gamma$ , affecting the signal fits. . . . .	58
448    5.1	Summary table for the limits on branching ratio of $Z \rightarrow \Upsilon(1S, 2S, 3S)\gamma$ and $H \rightarrow$ $\Upsilon(1S, 2S, 3S)\gamma$ decays. . . . .	69
450    5.2	Summary table for the limits on branching ratio of $Z \rightarrow \Upsilon(1S, 2S, 3S)\gamma$ , for the two possible categorization scenarios. . . . .	69

DRAFT

# 452 1 Introduction

- 453 INTRODUÇÃO
- 454 MOTIVAÇÃO PARA A ANÁLISE, RESUMO DO MÉTODO E RESULTADOS.
- 455 USAR UM PAPER DE CMS MUON PERFORMANCE PARA DIZER PORQUE
- 456 TRABALHAR COM DETECTORES DE MUONS

DRAFT

## 2 Rare Z and Higgs decays to quarkonia

### 2.1 Standard Model and Local Gauge Invariance

Physics understands the matter and how it interacts in terms of two components: four fundamental forces and elementary particles. From the weakest to the strongest, the fundamental forces are: gravitational, weak, electromagnetic and strong. All share common characteristics like, being mediated by particles <sup>1</sup>, being relevant within some effective range and have a associate a charge-like quantity (i.e. intrinsic characteristic of the object) that defines whether or not, particles might be subjected to a specific interaction.

Along with the fundamental interactions, the Standard Model (or simply *SM*) defines every existing matter in the Universe as a set of fundamental quantum objects, with properties that define their interaction. Those objects are said to be fundamental since, in the context of the SM, they are the smallest possible components of matter. We shall refer to them as fundamental particles. There four of those mediating particles (force carriers), gluon ( $g$  - for the strong interaction), photon ( $\gamma$  - for the electromagnetic interaction), Z and W (for weak interaction), all of them being vector bosons (spin 1). Besides the interaction mediators, described at Table 2.1, the fundamental particles are divided in two groups (*quarks* and *leptons*), with three generations, each. These are not force carriers, but elementary particles, endowed with charge-like characteristics that allow them to by exchange the vector bosons. Those are the building blocks of Matter in our Universe.

Figure 2.1 summarizes their properties. Table 2.1 presents the relative strength and effective range, for each one of the four fundamental interactions. The gravitational force is not study subject of the Standard Model.

Table 2.1: Relative strength (with respect to the strong force) and effective range of action for the four fundamentals interactions.

	Mediator	Relative Strength	Effective Range
Gravitational	Graviton	$10^{-41}$	$\infty$
Weak	W and Z bosons	$10^{-16}$	$10^{-18}$ m
Electromagnetic	Photon	$10^{-3}$	$\infty$
Strong	gluons	1	$10^{-15}$ m

There are six quark, up and down ( $u$  and  $d$  - first generation), charm and strange ( $c$  and  $s$  - second generation), top and bottom ( $t$  and  $b$  - first generation), in increasing invariant mass order of the generations. Since they interact thought all the three fundamental forces of the SM, they are said to possess electrical charge, flavour and color. Their generational counterparts, the leptons, don't interact via strong interaction, that is why they are said to have only flavours and electric charge. The leptons are electron and electron neutrino ( $e$  and  $\nu_e$  - first generation), muon and muon neutrino ( $\mu$  and  $\nu_\mu$  - second generation) and tau and tau neutrino ( $\tau$  and  $\nu_\tau$  - third generation). The neutrinos, within the SM, are massless, even though, experimental measurements have shown

<sup>1</sup>There is no evidence of the existence of the Graviton (force carrier associated to the gravitational force), even though, it is theorized by models that wish to comprehend gravity in a quantum perspective.

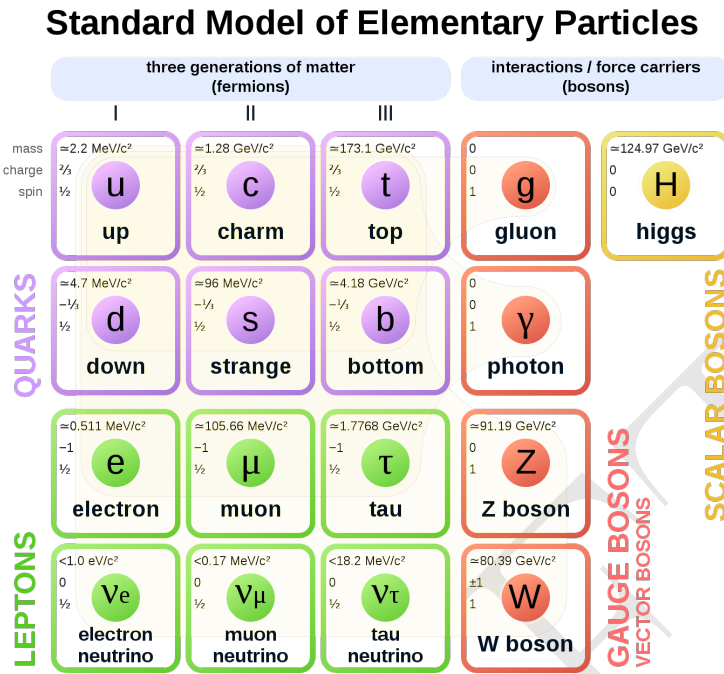


Figure 2.1: Elementary particles of the Standard Model, with their masses charges and spin. Those particles can be divided in two classes: boson (the interaction/force carriers) and the fermions, which are divided in three generations. Source: [1].

486 that they actually have mass [2]. Neutrinos are also electrically neutral, meaning that they only  
 487 interact through weak interactions.

488 Figure 2.1 also presents the Higgs Boson ( $H$ ) which is part of the SM and shall be discussed later.

489 Within the Standard Model, the theoretical basis that describe the fundamental interactions are  
 490 derived from a common principle: the local gauge invariance. According to Salam and Ward [3]:

491 "Our basic postulate is that it should be possible to generate strong, weak and electro-  
 492 magnetic interaction terms [...], by making local gauge transformations on the kinetic-  
 493 energy terms in the free Lagrangian for all particles."

494 Taking the Quantum Electrodynamics (QED) as an example: the quantum field theory that de-  
 495 scribes the x

496 The fundamental theories that compose the Standard Model are all derived from a fundamental  
 497 principle call

498 The electromagnetic force, in the context of fundamental interactions, is described by a gauge theory  
 499 called quantum electrodynamics.

## 500 Electroweak

501 Higgs discovery Production modes Decay modes

502 Yukawa coupling

503 Higgs results at CMS

504 The rare decays of the Higgs boson [4, 5] to a quarkonium state and a photon provide a unique  
 505 sensitivity to the magnitude of the Yukawa couplings of the Higgs boson to quarks [6–8]. These

506 couplings are difficult to access on hadronic collisions through direct decay of Higgs in quark-  
 507 antiquark, due to the immense background from QCD [9].

508 Among the channels available to explore Yukawa's couplings of light quarks [7, 8] are those with  
 509 heavy-quarkonia. The rare modes of decay of the Z boson have attracted attention focused on  
 510 establishing its sensitivity to New Physics [10], being configured as an alternative environment to  
 511 investigate the Yukawa couplings of the Higgs boson.

512 Also, the exclusive rare decays of vector bosons (Z, W) provide a favorable environment for testing  
 513 the factorization of QCD, thus allowing an approach in a context where the power of corrections  
 514 are definitely under control. The main focus of this kind of analysis are the hadronic radioactive  
 515 decays,  $Z \rightarrow M\gamma$ , where M can be a pseudoscalar or a vector meson ( $J/\psi, \phi, \Upsilon_n$ ).

516 They offer the perfect way to explore some of the leading order properties of the light-cone distri-  
 517 bution amplitudes (LCDAs) [11] of several mesons, but they present a difficulty, considering that  
 518 in the LHC energy scale the branching ratio of these processes is very small. There are theoretical  
 519 predictions [12, 13] that point out a branching ratio for several decay channels in the Standard  
 520 Model, as shown in the Table 2.2.

Physics Processes	Branching Ratio ( $\text{BR}_{SM}$ ):
$H \rightarrow \Upsilon(1S) + \gamma$	$5.22 \times 10^{-9}$
$H \rightarrow \Upsilon(2S) + \gamma$	$1.42 \times 10^{-9}$
$H \rightarrow \Upsilon(3S) + \gamma$	$9.10 \times 10^{-10}$
$Z \rightarrow \Upsilon(1S) + \gamma$	$4.88 \times 10^{-8}$
$Z \rightarrow \Upsilon(2S) + \gamma$	$2.44 \times 10^{-8}$
$Z \rightarrow \Upsilon(3S) + \gamma$	$1.88 \times 10^{-8}$

Table 2.2: Summary of cross section and branching ratio for  $H/Z \rightarrow \Upsilon(1S, 2S, 3S) + \gamma \rightarrow \mu^+ \mu^- + \gamma$  analysis. The effective cross-section will be discussed in section 4.1.2.

521 Recent studies on exclusive Higgs boson decays [14–16] in final states containing a simple vector  
 522 meson and a photon have caused interest in these physics topics. It was proposed to use these decays  
 523 as a possible way to explore non-standard Yukawa couplings of the Higgs boson. Such measures are  
 524 quite challenging in the LHC environment. The observation of hadronic decays of vector bosons  
 525 provides could provide a new frontier for the nature of heavy quarkonia production in hadronic  
 526 collisions.

527 Along the same lines, the simple exploration of rare SM decays, even in scenarios where anomalous  
 528 couplings are, in principle, ruled out by direct measurements [17], as in the case of this analysis  
 529 ( $H \rightarrow \Upsilon(nS) + \gamma$ ), are still important as a stress test of the SM and as reference for future  
 530 measurements. Specially the later one, when you consider that the small predicted cross sections  
 531 from Table 2.2, most probably, would imply that an observation of this decay would be unlikely  
 532 even in the HL-LHC [18].

533 This measurement is sensitive to the direct and indirect production (Figure 2.2). The *direct* process  
 534 consists in the decay of boson (Higgs or Z) to a quark anti-quark pair, in which, one of the quarks  
 535 radiates a photon and the pair hadronizes to a meson (a  $\Upsilon(nS)$ , for this study), while in *indirect*  
 536 process, the decay happens to a  $\gamma\gamma^*(Z)$ , with the subsequent decay of the  $\gamma^*(Z)$  to a quark anti-  
 537 quark that hadronizes.

538 Clearly, only the direct process is sensible to the Yukawa coupling of the boson with the quarks,  
 539 but, since both processes are indistinguishable in their final state, the in direct process needs to be  
 540 taken into account. In this study, a dimuon final state is used to tag the  $\Upsilon(nS)$ .

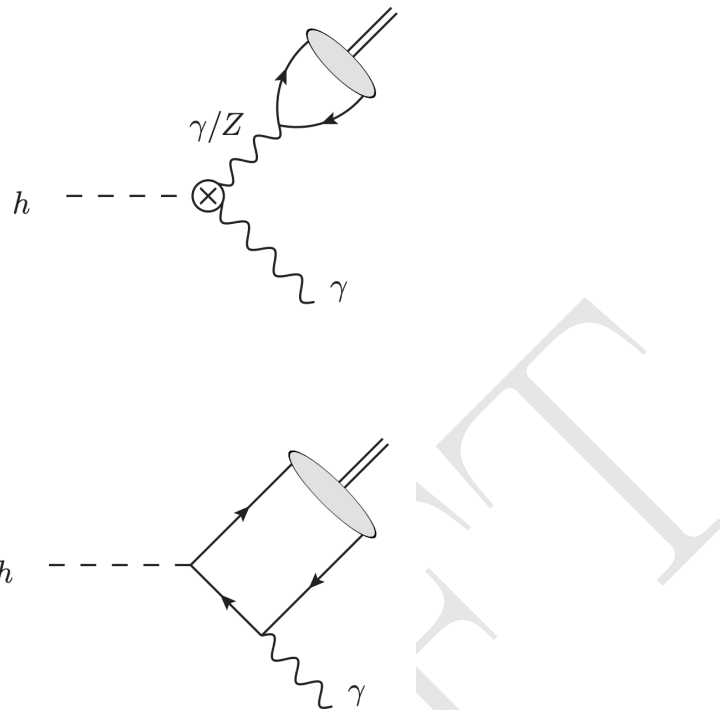


Figure 2.2: Example of leading order diagrams for the indirect (top) and direct (bottom) production mechanisms. In the diagrams, the  $h$  can also be understood as a  $Z$  boson.

Even though there is different theoretical predictions for the cross section of this process and its twin brother ( $H \rightarrow J/\Psi + \gamma$ ), each one taking into account different levels of complexity, the 2013 paper [6], from G. Bodwin, F. Petriello, S. Stoynev and M. Velasco, summarizes very well and in a simpler manner, the most relevant phenomenological results on these decays. For the decay to  $J/\Psi + \gamma$ , the quantum interference with the indirect amplitude, enhances the directed production, leading to a larger, and potentially observable, cross section. This is not true for the  $\Upsilon(nS) + \gamma$  decay, since the interference is destructive, diminishing the cross sections.

Another interesting aspect of this study is that, for both  $Hc\bar{c}$  and  $Hb\bar{b}$  direct coupling measurements are not sensible to the sign of the Yukawa coupling, while the presence of the indirect process in the  $H \rightarrow M + \gamma$  ( $M$  standing for  $J/\Psi$  or  $\Upsilon(nS)$ ) decays resolve this ambiguity.

Finally, since the  $\Upsilon(nS) + \gamma$  decay has a much smaller cross section, because of the destructive quantum interference between direct and indirect production mechanisms, a small deviation in the  $Hb\bar{b}$  Yukawa coupling, can lead a large increase in the expected branching ratio, making this channel sensible any non-Standard Model process that might interfere in this final state. This becomes clear when we look to Figure 2.3.

## 2.2 Recent results

The ATLAS experiment [19] already have two results on this decays [20, 21]. The first one corresponds to data taken from 2015, while the former one, corresponds to data from 2016 (the same data taking period to which this study refers).

What concerns the most updated result, the study corresponded to  $36.1 \text{ fb}^{-1}$  at  $\sqrt{s} = 13 \text{ TeV}$  and no significant excess was found by the experiment. Upper limits for the were obtained,

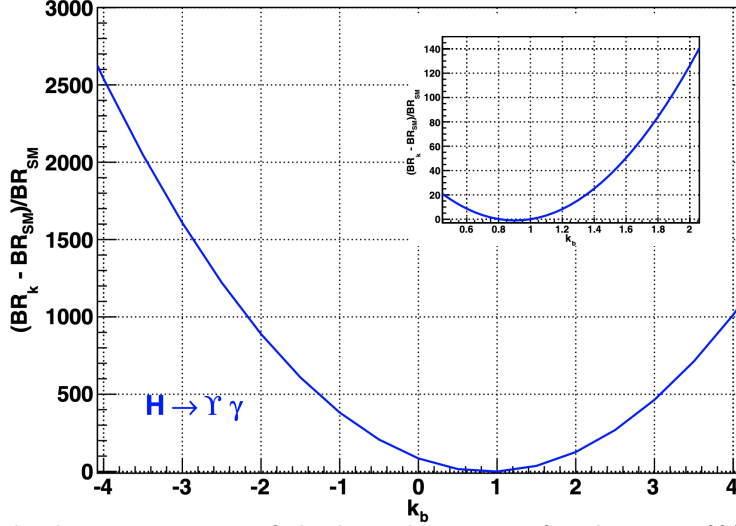


Figure 2.3: Expected relative variation of the branching ratio for the  $H \rightarrow \Upsilon(nS) + \gamma$  to  $k_b$ , where  $k_b = g(Hb\bar{b})/g(Hb\bar{b})_{SM}$  is the ratio for the observed and expected Yukawa coupling oh  $Hbb$ . [6]

562 assuming the Standard Model branching fractions predictions, at 95% confidence level, according  
563 to table 2.3.

Decay	$\mathcal{B}F$ at 95% CL
$H \rightarrow J/\Psi + \gamma$	$< 4.5 \times 10^{-4}$
$H \rightarrow \Psi(2S) + \gamma$	$< 2.0 \times 10^{-3}$
$H \rightarrow \Upsilon(1S) + \gamma$	$< 4.9 \times 10^{-4}$
$H \rightarrow \Upsilon(2S) + \gamma$	$< 5.9 \times 10^{-4}$
$H \rightarrow \Upsilon(3S) + \gamma$	$< 5.7 \times 10^{-4}$
<hr/>	
$Z \rightarrow J/\Psi + \gamma$	$< 2.3 \times 10^{-6}$
$Z \rightarrow \Psi(2S) + \gamma$	$< 4.5 \times 10^{-6}$
$Z \rightarrow \Upsilon(1S) + \gamma$	$< 2.8 \times 10^{-6}$
$Z \rightarrow \Upsilon(2S) + \gamma$	$< 1.7 \times 10^{-6}$
$Z \rightarrow \Upsilon(3S) + \gamma$	$< 4.8 \times 10^{-6}$

Table 2.3: Observed upper limits, by the ATLAS experiment, on the branching fractions for the Higgs and Z decays (last result). Detailed comparisons with the results obtained in this study will be presented in chapter 5.

564 It is worth it to mention that the ATLAS papers present a broader analysis, including the decays  
565 to  $J/\Psi + \gamma$  and  $\Psi(2S) + \gamma$ .

566 CMS [22] also have a result on  $J/\Psi + \gamma$  and  $\Psi(2S) + \gamma$  decay channel, of the Higgs and Z boson [23].  
567 The observed upper limit on the branching fraction for these decays are presented in table 2.4.

568 No result on the Z and Higgs decays to  $\Upsilon(nS) + \gamma$  have been published by CMS, yet.

569 The results presented here, are a subset of a broader topic related to the rare decays of Standard  
570 Model (SM) boson, involving quarkonia. Sticking only to CMS results, we can cite:

- 571 • Search for Higgs and Z boson decays to  $J/\psi$  or  $\Upsilon$  pairs in proton-proton collisions at  $\sqrt{s} =$   
572 13 TeV [24].
- 573 • Observation of the  $Z \rightarrow \psi\ell^+\ell^-$  decay in pp collisions at  $\sqrt{s} = 13$  TeV [25]. This one specifically,  
574 is the first observation a such decay, involving a Z boson.

Channel	Polarization	$\mathcal{B}F$ at 95% CL
$Z \rightarrow J/\Psi + \gamma$	Unpolarized	$< 1.4 \times 10^{-6}$
	Transverse	$< 1.5 \times 10^{-6}$
	Longitudinal	$< 1.2 \times 10^{-6}$
$H \rightarrow J/\Psi + \gamma$	Transverse	$< 7.6 \times 10^{-4}$

Table 2.4: Observed upper limits, by CMS, on the branching fractions for the Higgs and Z decays. The numbers are compatible with the ones obtained by ATLAS. The results presented for different polarization scenarios of the  $J/\Psi$ .

575 **verificar resultados se outros foram publicados.**

## <sup>576</sup> 3 Experimental Setup

<sup>577</sup> The central feature of the CMS apparatus is a superconducting solenoid of 6 m internal diameter,  
<sup>578</sup> providing a magnetic field of 3.8 T. Within the solenoid volume are a silicon pixel and strip tracker,  
<sup>579</sup> a lead tungstate crystal electromagnetic calorimeter (ECAL), and a brass and scintillator hadron  
<sup>580</sup> calorimeter (HCAL), each composed of a barrel and two endcap sections. Forward calorimeters ex-  
<sup>581</sup> tend the pseudorapidity coverage provided by the barrel and endcap detectors. Muons are detected  
<sup>582</sup> in gas-ionization chambers embedded in the steel flux-return yoke outside the solenoid.

<sup>583</sup> A detailed description of the CMS detector, together with a definition of the coordinate system  
<sup>584</sup> used and the relevant kinematic variables, can be found in [26].

<sup>585</sup> **falar do sistema de coordenadas e definir  $\eta$**

### <sup>586</sup> 3.1 Tracker

<sup>587</sup> **FAZER!**

<sup>588</sup> The silicon tracker measures charged particles within the pseudorapidity range  $|\eta| < 2.5$ . It consists  
<sup>589</sup> of 1440 silicon pixel and 15 148 silicon strip detector modules. For non-isolated particles of  $1 <$   
<sup>590</sup>  $p_T < 10 \text{ GeV}$  and  $|\eta| < 1.4$ , the track resolutions are typically 1.5% in  $p_T$  and 25–90 (45–150)  $\mu\text{m}$   
<sup>591</sup> in the transverse (longitudinal) impact parameter [27]

### <sup>592</sup> 3.2 Electromagnetic Calorimeter

<sup>593</sup> **FAZER!**

<sup>594</sup> The ECAL consists of 75 848 lead tungstate crystals, which provide coverage in pseudorapidity  
<sup>595</sup>  $|\eta| < 1.48$  in a barrel region (EB) and  $1.48 < |\eta| < 3.0$  in two endcap regions (EE). Preshower  
<sup>596</sup> detectors consisting of two planes of silicon sensors interleaved with a total of  $3X_0$  of lead are  
<sup>597</sup> located in front of each EE detector [28]. In the barrel section of the ECAL, an energy resolution of  
<sup>598</sup> about 1% is achieved for unconverted or late-converting photons that have energies in the range of  
<sup>599</sup> tens of GeV. The remaining barrel photons have a resolution of about 1.3% up to a pseudorapidity  
<sup>600</sup> of  $|\eta| = 1$ , rising to about 2.5% at  $|\eta| = 1.4$ . In the endcaps, the resolution of unconverted or late-  
<sup>601</sup> converting photons is about 2.5%, while the remaining endcap photons have a resolution between  
<sup>602</sup> 3 and 4% [29]. When combining information from the entire detector, the jet energy resolution  
<sup>603</sup> amounts typically to 15% at 10 GeV, 8% at 100 GeV, and 4% at 1 TeV, to be compared to about  
<sup>604</sup> 40%, 12%, and 5% obtained when the ECAL and HCAL calorimeters alone are used.

### <sup>605</sup> 3.3 Hadronic Calorimeter

<sup>606</sup> **FAZER!**

## 607 3.4 Muon System

608 FAZER!

609 Muons are measured in the pseudorapidity range  $|\eta| < 2.4$ , with detection planes made using three  
610 technologies: drift tubes, cathode strip chambers, and resistive plate chambers. The single muon  
611 trigger efficiency exceeds 90% over the full  $\eta$  range, and the efficiency to reconstruct and identify  
612 muons is greater than 96%. Matching muons to tracks measured in the silicon tracker results in  
613 a relative transverse momentum resolution, for muons with  $p_T$  up to 100 GeV, of 1% in the barrel  
614 and 3% in the endcaps. The  $p_T$  resolution in the barrel is better than 7% for muons with  $p_T$  up to  
615 1 TeV [30].

### 616 3.4.1 DT

617 FAZER!

### 618 3.4.2 CSC

619 FAZER!

### 620 3.4.3 RPC

621 Due to the particularities of the study, especially the contributions given to the RPC project of  
622 CMS, chapter 6 is devoted exclusively to this sub-detector.

### 623 3.4.4 GEN

624 FAZER!

## 625 3.5 Trigger and Data Acquisition

626 FAZER!

627 A two-tiered trigger system [31]. The first level (L1), composed of custom hardware processors, uses  
628 information from the calorimeters and muon detectors to select events at a rate of around 100 kHz  
629 within a time interval of less than  $4\ \mu\text{s}$ . The second level, known as the high-level trigger (HLT),  
630 consists of a farm of processors running a version of the full event reconstruction software optimized  
631 for fast processing, and reduces the event rate to around 1 kHz before data storage.

## 632 3.6 Simulation, reconstruction and computing

633 FAZER!

634 **3.7 Particle Flow Algorithm**

635 **FAZER!**

DRAFT

DRAFT

# <sup>636</sup> 4 Physics Analysis

<sup>637</sup> **DEFINIR A ANALISE**

<sup>638</sup> **EXPLICAR O PROCESSO E EXEMPLOS DE GRAFICO**

<sup>639</sup> **EXPLICAR A ESTRATEGIA**

## <sup>640</sup> 4.1 Datasets and simulated events

### <sup>641</sup> 4.1.1 Data samples

<sup>642</sup> The data sample used in this analysis consists of the 2016 13 TeV run with 25 ns bunch separation  
<sup>643</sup> recorded by CMS. This data sample is composed only by events that were certified from all CMS  
<sup>644</sup> subsystems and reconstruction specialist as good for physics analysis.

<sup>645</sup> This data sample corresponds to  $35.86 \text{ fb}^{-1}$  of integrated luminosity [32].

### <sup>646</sup> 4.1.2 Simulated datasets

<sup>647</sup> Data simulation at CMS is done by the use of Monte Carlo (from here on, simply called MC)  
<sup>648</sup> simulations generates pseudo-random events, constrained by the physics of the related process to  
<sup>649</sup> which we are interested, including the effect of the produced particles interacting with the detector.  
<sup>650</sup> The simulation starts with the **hard-scattering** process, at parton (constituents of the proton)  
<sup>651</sup> level, done usually, by matrix element generators, which impose to the incoming and outgoing  
<sup>652</sup> partons, the dynamics of the simulated process, according to some pre-defined theoretical model.  
<sup>653</sup> Along the hard interaction simulation, the **fragmentation** process takes place. Since the matrix  
<sup>654</sup> element generator provide information on the parton level, it is necessary to extract the momentum  
<sup>655</sup> distribution of the parton as a function of the  $Q^2$  (transferred momentum) of the process. To do  
<sup>656</sup> so, MC generators use the PDFs (parton distribution functions) to sample those values, accordingly.  
<sup>657</sup> The matrix element formalism also allows the simulation of the process, taking into account, different  
<sup>658</sup> orders of perturbations, like NLO (next-to-leading-order), NNLO (next-to-next-to-leading-order),  
<sup>659</sup> and so on.

<sup>660</sup> After the hard-scattering, the **showering** process simulates the radiation emission by gluons and  
<sup>661</sup> quarks in the initial and final states. Along the hard interaction, the other proton constituents  
<sup>662</sup> may also interact through soft interaction. This part of the simulation is called **multiple parton**  
<sup>663</sup> **interaction** (MPI). The last components of the simulation is the **hadronization** and the **decay**  
<sup>664</sup> **of heavy hadrons and leptons**. The former one, imposes the QCD confinement to low energy  
<sup>665</sup> quarks and gluons <sup>1</sup>, while the latter one, implements specific models to decays heavy hadrons and  
<sup>666</sup> leptons, like  $B$  hadrons and taus.

---

<sup>1</sup>QCD forbids coloured objects to exist in non-asymptotic states. They must decay to more complex systems, until they form stable colorless states.

667 Usually, different generators are used to simulate a process. Each specialized in one or more steps.

668 A summary of the signal and background MC samples used is presented in Table 4.1. These  
 669 simulated data are comparable with the proton-proton collision using 2016 data conditions and the  
 670 **pileup**<sup>2</sup> events are added to the simulated event in this step. The pileup events distribution used is  
 671 modeled as a Poisson pdf (probability distribution function) with mean of 23 events, as recommended  
 672 by CMS. Detector response in the MC samples is simulated using a detailed description of the CMS  
 673 detector, based on GEANT4 [33].

674 The signal MC samples are simulated for the Higgs bosons decaying to  $\Upsilon(nS)(\rightarrow \mu\mu) + \gamma$  channels  
 675 with POWHEG v2.0 [34–36], at next-to-leading order (NLO) of Feynman graphs computation, for  
 676 the following production modes: gluon-gluon fusion (ggF), vector boson fusion (VBF), associated  
 677 production (VH) and associated top production (ttH), with cross-section summarized at table 4.1.  
 678 A extensive review of these production modes can be found at [37]. The PYTHIA 8 generator [38,  
 679 39] is used for hadronization and fragmentation with underlying event tune CUETP8M1 [40]. The  
 680 parton distribution functions (pdf) NNPDF3.0 [41] are used.

681 For Z decaying to  $\Upsilon(nS)(\rightarrow \mu\mu) + \gamma$  channels, the signal samples are simulated with MADGRAPH 5  
 682 \_MC@NLO 2.6.0 matrix element generator [42] at next leading order and the PYTHIA 8 generator [38,  
 683 39] for hadronization and fragmentation with underlying event tune CUETP8M1 [40].

684 The Drell-Yan process,  $pp \rightarrow Z \rightarrow \mu\mu\gamma_{FSR}$ , results in the same final state as the signal. This  
 685 process exhibits a peak in the three-body invariant mass,  $m_{\mu\mu\gamma}$ , at the Z boson mass,  $m_Z$ , and it is  
 686 a resonant background for this channel, therefore referred to as a Peaking Background.

687 It is taken into account when deriving the upper limit on the branching fraction for  $Z \rightarrow \Upsilon(nS) +$   
 688  $\gamma \rightarrow \mu\mu + \gamma$ . The MADGRAPH 5 \_MC@NLO 2.6.0 matrix element generator [42] at leading order,  
 689 interfaced with PYTHIA 8.226 for parton showering and hadronization with tune CUETP8M1 [40],  
 690 is used to generate a sample of these resonant background events. The photons in these events are  
 691 all produced as final-state radiation from the  $Z \rightarrow \mu\mu$  decay and therefore the  $m_{\mu\mu\gamma}$  distribution  
 692 peaks at the Z boson mass and there is no continuum contribution.

693 Similarly, the Higgs boson Dalitz decay [43],  $H \rightarrow \gamma^*\gamma \rightarrow \mu\mu + \gamma$ , is a Peaking Background  
 694 (resonant) to  $H \rightarrow \Upsilon(nS) \rightarrow \mu\mu + \gamma$ . It is simulated at NLO with MADGRAPH 5 \_MC@NLO  
 695 2.6.0 matrix element generator [42] at next-to-leading order and the PYTHIA 8 generator [38, 39] for  
 696 hadronization and fragmentation with underlying event tune CUETP8M1 [40]. This Higgs Dalitz  
 697 Decay sample, was generated only for the ggF production mode, but its cross-section was rescaled  
 698 to the full Higgs cross-section. This process will present a small contribuition of selected events, so  
 699 this approximation should be sufficient for the Higgs Peaking Background modeling.

700 There are also background processes that do not give resonance peaks in the three-body invariant  
 701 mass spectrum. They are modeled from data, as it will be explained latter in more details.

702 The number of simulated events is is rescaled by the Effective  $\sigma$ , from table 4.1, in order to match  
 703  $35.86 fb^{-1}$  of integrated luminosity, from the recorded data. Being  $N = \sigma\mathcal{L}$ ,  $N$  in the number of

---

<sup>2</sup>Each LHC collision recorded by CMS, is composed not by a single  $pp$  interaction, but by a bunch of protons crossing. In this case, a hard interaction is actually surrounded by many soft interaction between adjacent protons. The extra activity produced in these interactions, and caught by the detector, is called **pileup** and has its signal mixed with the hard one. Since, during the data taking, the number of pileup interactions varies according to the instantaneous luminosity, the MC are mixed some soft interaction only sample, called Minimum Bias. The number of mixed soft interaction (pileup events) is governed by a Poisson distribution with a pre-defined mean. The MC samples are then reweighted to match the same distribution of primary vertexes for the corresponding Data. Systematics related to this procedure will be discussed later.

Physics Processes	Branching Ratio ( $BR_{SM}$ )	Effective $\sigma$ (in pb)	Generator	Sample Type
$H \rightarrow \Upsilon(1S) + \gamma$	$5.22 \times 10^{-9}$	$7.14 \times 10^{-9}$	POWHEG 2.0	Signal
$H \rightarrow \Upsilon(2S) + \gamma$	$1.42 \times 10^{-9}$	$1.51 \times 10^{-9}$	POWHEG 2.0	Signal
$H \rightarrow \Upsilon(3S) + \gamma$	$9.10 \times 10^{-10}$	$1.10 \times 10^{-9}$	POWHEG 2.0	Signal
$Z \rightarrow \Upsilon(1S) + \gamma$	$4.88 \times 10^{-8}$	$6.80 \times 10^{-5}$	MADGRAPH 5	Signal
$Z \rightarrow \Upsilon(2S) + \gamma$	$2.44 \times 10^{-8}$	$2.69 \times 10^{-5}$	MADGRAPH 5	Signal
$Z \rightarrow \Upsilon(3S) + \gamma$	$1.88 \times 10^{-8}$	$2.34 \times 10^{-5}$	MADGRAPH 5	Signal
H Dalitz Decay	$3.83 \times 10^{-5}$	$2.13 \times 10^{-3}$	MADGRAPH 5	Peaking Background
$Z \rightarrow \mu\mu\gamma_{FSR}$	—	$7.93 \times 10^{-2}$	MADGRAPH 5	Peaking Background

Table 4.1: Datasets simulated (MC) for 2016 conditions. Assuming that  $\sigma(pp \rightarrow H)$ , taking into consideration all the simulated Higgs production modes, is  $55.13 \text{ pb}$  [44] and  $\sigma(pp \rightarrow Z \rightarrow \mu\mu)$  is  $57094.5 \text{ pb}$ , including the next-to-next-to-leading order (NNLO) QCD contributions, and the next-to-leading order (NLO) electroweak corrections from fewz 3.1 [45] calculated using the NLO PDF set NNPDF3.0, with the phase space selection in invariant mass of the dimuon system of  $m_{\mu\mu} > 50 \text{ GeV}$ . For the Higgs Dalitz  $\sigma$ , we consider only the gluon fusion contribution ( $\sigma_{ggF} = 48.6 \text{ pb}$ ) [44]. The Higgs Dalitz Decay  $BR_{SM}$  and the  $Z \rightarrow \mu\mu\gamma_{FSR}$  were obtained with MCFM 6.6 [46] (as in the CMS search for Higgs Dalitz Decay in at  $\sqrt{s} = 8 \text{ TeV}$  [47]) and with MADGRAPH 5 \_MC@NLO, respectively. The  $BR_{\Upsilon(1S,2S,3S) \rightarrow \mu\mu}^{PDG} = (2.48, 1.93, 2.18) \times 10^{-2}$  is quoted from Particle Data Group report (PDG) [2]. The "Effective  $\sigma$ " for the signal samples is  $\sigma(pp \rightarrow Z(H)) \times BR_{SM} \times BR_{\Upsilon(nS) \rightarrow \mu\mu}^{PDG}$ .

704 events for a process,  $\sigma$  is the cross-section and  $\mathcal{L}$  is the integrated luminosity, the reweighting factor,  
 705 for a simulated sample is:

$$w_{MC} = \frac{\sigma \mathcal{L}}{N_{sim}}, \quad (4.1)$$

706 where  $N_{sim}$  is the number of simulated events for a specific process.

707 The simulated sample are also corrected by the data pile-up distribution, since the pileup distribu-  
 708 tion of MC is different from the pileup distribution of data. The way to correct the MC is to assign  
 709 a weight to each bin of the MC pileup distribution, with respect to the data. The rescaling is defined  
 710 as the ratio between normalized Pile-up (PU) distribution for Data and MC.

$$w_{PU}(n) = \frac{P_{PU}^{Data}(n)}{P_{PU}^{Sim}(n)}, \quad (4.2)$$

711 where  $n$  is the number of interaction per bunch crossing (pile-up).

## 712 4.2 Contribution of the $\Upsilon(nS)$ polarisation

713 Measurements of quarkonium polarization observables may yield information about quarkonium  
 714 production mechanisms that are not available from the study of unpolarized cross sections alone.  
 715 The three polarization states of a  $J = 1$  quarkonium can be specified in terms of a particular  
 716 coordinate system in the rest frame of the quarkonium. This coordinate system is often called the  
 717 "spin-quantization frame".

718 In a hadron collider,  $\Upsilon(1S, 2S, 3S)$  are reconstructed through their electromagnetic decays into a  
 719 lepton pair. The information about the polarization of the quarkonium state is encoded in the

angular distribution of the leptons. This angular distribution is usually described in the quarkonium rest frame with respect to a particular spin-quantization frame [48]. The polarization of the  $\Upsilon(1S, 2S, 3S)$  is not simulated for signal MC sample and we only apply a reweighting scale factor to each event and so we can emulate the polarization effects [49]. Figure 4.1 present the distributions of  $\cos \Theta$  of  $\Upsilon \rightarrow \mu\mu$ , where  $\Theta$  is the angle between the positive muon and the  $\Upsilon$  in the Z (Higgs) rest-frame. At Table 4.2 we show the the analytical functions used to describe the extremes scenarios (Unpolarized, Transverse Polarization and Longitudinal Polarization) reweighting, presented in this analysis.

It is worth stating that, for the Higgs decay, on the Transverse Polarization is considered. For the Z decay, because of its spin nature, the Unpolarized scenario is used as the nominal one, and the effects of the two other extremes (Transverse Polarization and Longitudinal Polarization) are quoted as systematics.

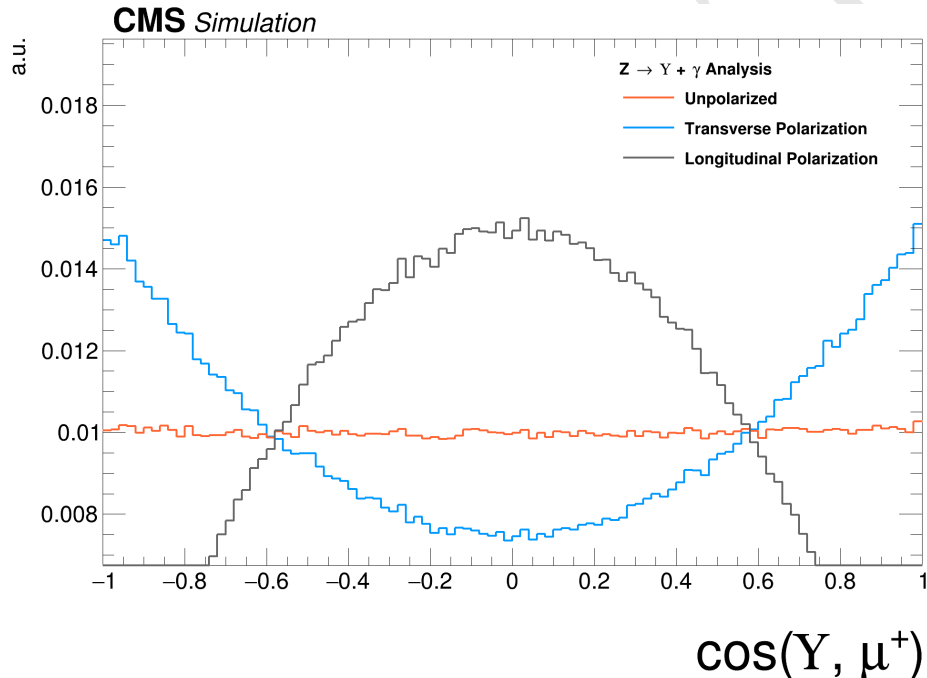


Figure 4.1: Distributions of  $\cos \theta$  of  $\Upsilon \rightarrow \mu\mu$  and  $\gamma^* \rightarrow \mu\mu$ . The orange distribution is the  $Z \rightarrow \Upsilon(1S, 2S, 3S) + \gamma$  sample before reweighting (Unpolarized); the blue and gray distributions are  $Z \rightarrow \Upsilon(1S, 2S, 3S)$  sample after reweighting, for the Transverse and Longitudinal Polarization.

$J_Z$	Polarisation Scenario	Analytic Description
$\pm 1$	Transverse	$3/4 \times (1 + (\cos \Theta)^2)$
0	Longitudinal	$3/2 \times (1 - (\cos \Theta)^2)$

Table 4.2: Summary of the impact of reweighted of polarization contribution using several scenarios.

### 4.3 Kinematical studies using MC generator

Using the PYTHIA 8.226 generator, the Monte Carlo signals are produced for Higgs (Z) boson events decaying in ( $\Upsilon(1S, 2S, 3S)$ ) +  $\gamma$ , which are highly boosted. Observing the kinematic generator level distributions in Figure 4.2 for Z boson and Figure 4.3 for Higgs boson, we could conclude that the high- $E_T$  (transverse energy, with respect to the beam line) photon will be back-to-back to the  $\Upsilon$  particles being possible to apply an isolation selection to identify a photon in this kinematic topology.

738 Also, we can observe those transverse momenta of the leading/trailing  $p_T$  (transverse momemtum,  
739 with respect to the beam line) muon<sup>3</sup> and the photon and distances  $\Delta R = \sqrt{\Delta\eta^2 + \Delta\phi^2}$  between  
740 the two muons and between the muons and the photon are a good variable that can be used to  
741 discriminate the contribution between signal and background events. The leading muon transverse  
742 momentum can be greater than 45(30) GeV and trailing muon is greater than 10(20) GeV in Higgs(Z)  
743 decay.  $\Delta R$  distributions of the two muons and between the muons and the photon in the both cases  
744 show that the two muons are very close and the photon is back-to-back in relation of dimuon system.  
745 Another feature of this kinematic topology is that the production vertex between muons produced  
746 in  $\Upsilon$  decaying events and the high- $E_T$  photon is very well defined.

---

<sup>3</sup>In this study we define leading muon and the muon, decaying from the  $\Upsilon$ , with highest  $p_T$ . Trailing muon is the one with the second hight  $p_T$ .

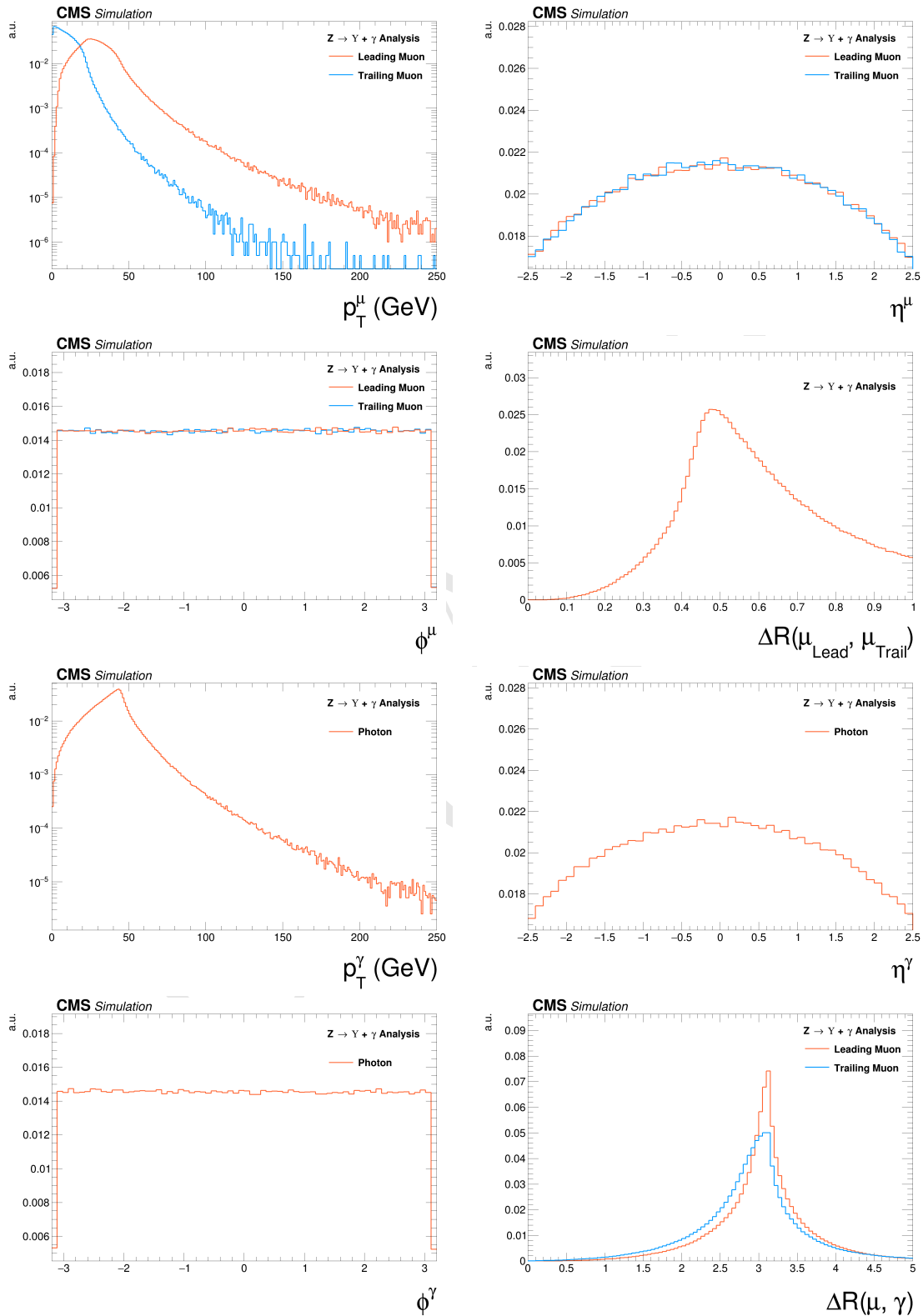


Figure 4.2: Generator level distributions of main variables for  $Z \rightarrow \Upsilon(1S, 2S, 3S) + \gamma$ : Transverse momenta of the leading/trailing  $p_T$  muon and the photon, pseudorapidity ( $\eta$ ) and  $\phi$  of the muons and the photon, distances  $\Delta R$  between the two muons and between the muons and the photon. All the distributions shown in the figure are normalized to the unity of area.

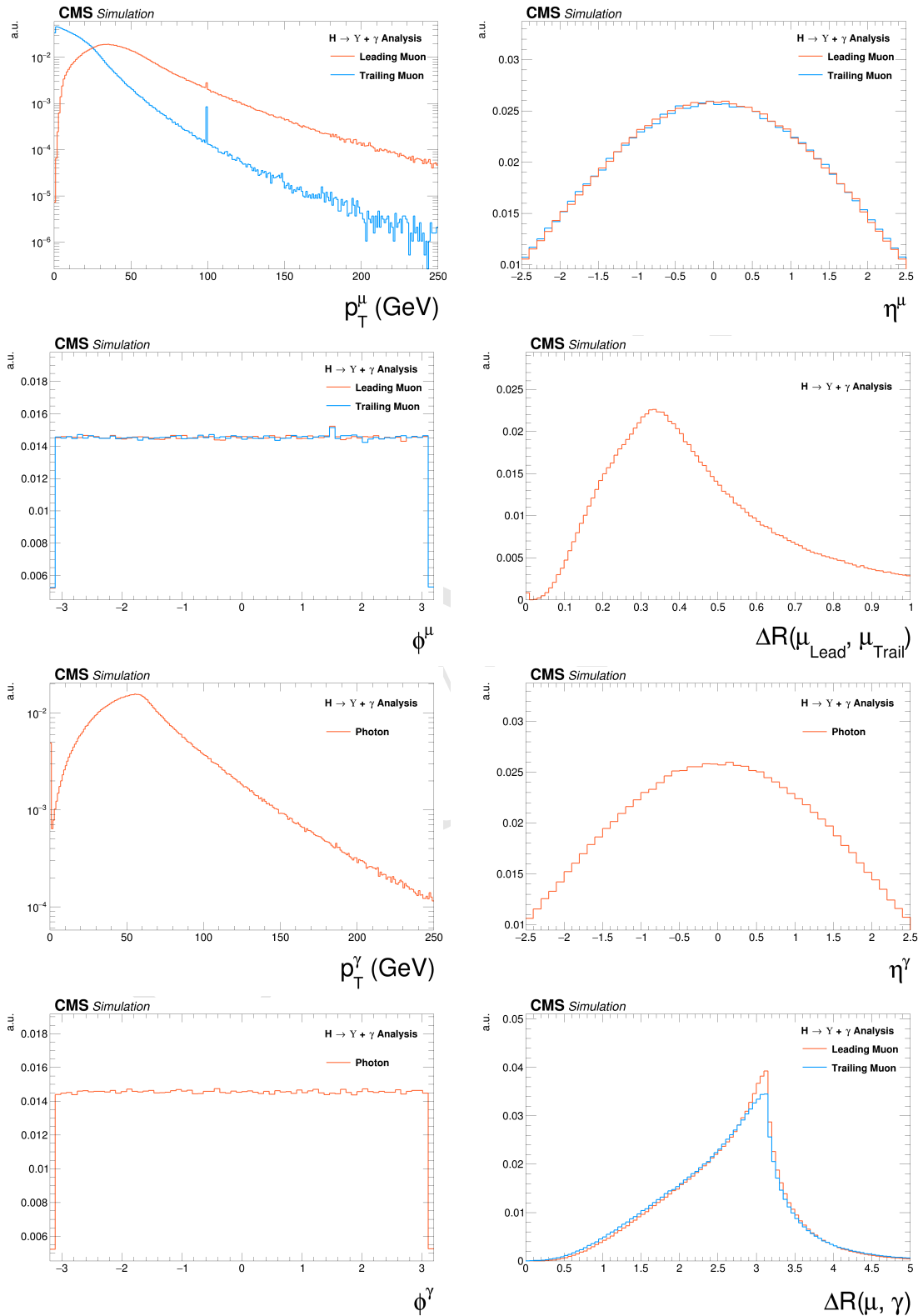


Figure 4.3: Generator level distributions of main variables for  $H \rightarrow \Upsilon(1S, 2S, 3S) + \gamma$ : Transverse momenta of the leading/trailing  $p_T$  muon and the photon, pseudorapidity ( $\eta$ ) and  $\phi$  of the muons and the photon, distances  $\Delta R$  between the two muons and between the muons and the photon. All the distributions shown in the figure are normalized to the unity of area.

## 747 4.4 Event selection

748 The event selection is divided in two steps. At first, a set of cuts related to trigger and physics object  
 749 (muons and photons) selection is applied. High level physics objects at CMS are reconstructed based  
 750 of the Particle Flow (PF) algorithm [50]. This selection is called, within this analysis, Group I.

751 For the events that pass the Group I selection, another set of cuts is applied, this time focusing on  
 752 kinematical (phase space) event selection, in order to enhance the signal to background ratio. This  
 753 later set is called, within this analysis, Group II. After full selection, three exclusive categories are  
 754 defined, based on the photon's  $\eta$  region and its energy spread shape within the ECAL cells (R9).

755 After the full selection, a background and signal modeling process is applied, based on the invariant  
 756 mass distributions, which will be explained in the next section.

## 757 4.5 Trigger and physics object selection (Group I)

### 758 4.5.1 Trigger

759 In this study, the same trigger requirements are applied to both data and simulated samples. For  
 760 the first trigger level (L1), events are selected if they present at least one muon with transverse  
 761 momentum greater than 5 GeV and an isolated <sup>4</sup> photon or electron with transverse momentum  
 762 greater than 18 GeV (at L1, there is no differentiation between photons and electrons). At the  
 763 software level of the trigger system (HLT), the events are required to have at least one muon with  
 764 transverse momentum greater than 17 GeV and a photon with transverse momentum greater than  
 765 30 GeV.

766 In order to compensate any difference in the trigger performance between simulated and data sam-  
 767 ples, for every selected MC a proper scale factor is applied, based on the the  $p_T$  of the reconstructed  
 768 muon and photon. These scale factor computed by the ratio between efficiency of the trigger for  
 769 the Data sample over the efficiency for a MC sample. These efficiencies are calculated with the  
 770 tag-and-probe method, exploring the the resonance of a final state composted by two muon and  
 771 one photon in the vicinity of the  $Z$  boson invariant mass. To this final state, a selections was  
 772 applied to ensure that the photon comes from a Final State Radiation process, allowing us to use  
 773 the tag-and-probe method.

774 Considering the similarity of this analysis with the  $H/Z \rightarrow J/\psi + \gamma$  analysis [23], not only in therm  
 775 of data samples, but also for triggering and physics object selection, the same scale factors were  
 776 applied. More details are given in the same paper.

### 777 4.5.2 Muon Identification

778 Ahead of any selection, a standard CMS "Ghost Cleaning" procedure is applied to all reconstructed  
 779 muons in order to avoid that a single physical muon is reconstructed as two or more. For this  
 780 procedure, reconstructed muons sharing 50% or more segments in the system are arbitrated.

781 After the cleaning, a muon is chosen when it passes a a two step identification: the **Loose ID** and  
 782 the **Tight ID**. Below the muon identification procedure is summarized .

---

<sup>4</sup>The concept of isolation will be detailed later, but in summary, it means a object which has very small activity (above a certain threshold of energy/momentum) around it. In hadron-hadron collider, isolation is a characteristics of hard interactions.

783 For the Loose ID, each muon is required to:

- 784 • have transverse momentum greater than 5 GeV, in order to cope with Particle Flow require-  
785     ments;
- 786 • be within the muon system acceptance:  $|\eta| < 2.4$ ;
- 787 • to have a three dimensional impact parameter uncertainty smaller than 4;
- 788 • to have transverse distance smaller than 0.5 cm ( $d_{xy} < 0.5$ ), with respect to the primary  
789     vertex (PV);
- 790 • to have longitudinal distance greater than 1.0 cm ( $d_z < 1$ ), with respect to the primary vertex  
791     (PV).

792 Muons reconstructed only in the muon system, without a correspondence with the tracker, are  
793 rejected. The last three requirements of the Loose ID are imposed in order to suppress muons from  
794 in-flight decays.

795 The primary vertex itself, is determined as the reconstructed vertex with the biggest sum of  $p_T^2$  in  
796 the event. This sum is performed, considering all the charged PF candidates clustered by the jet  
797 finding algorithms [51, 52] and the MET, which is defined as the  $p_T$  vector sum of all the charged  
798 and neutral PF candidates associated to that vertex.

799 For the Tight ID, muons with transverse momentum  $p_T < 200$  GeV, are required to have been  
800 reconstructed with the Particle Flow (PF) algorithm. If they have  $p_T > 200$  GeV, they should re-  
801 constructed with the Particle Flow (PF) algorithm or satisfy the strict tracker requirements (defined  
802 in table 4.3).

Requirement	Technical definition
Muon station matching	Muon is matched to segments in at least two stations in the muon system
Good $p_T$ measurement	$\frac{p_T}{\sigma_{p_T}} < 0.3$
Vertex compatibility ( $x - y$ )	$d_{xy} < 2$ mm
Vertex compatibility ( $z$ )	$d_z < 5$ mm
Pixel hits	At least one pixel hit
Tracker hits	Hits in at least six tracker layers

Table 4.3: Conditions for a muon to pass the strict tracker requirements.

803 To mitigate spurious signal in the detector that would mimic a muon, the leading muon (the one  
804 with highest  $p_T$ ) is required to be isolated within a cone of radius  $\Delta R = \sqrt{\Delta\eta^2 + \Delta\phi^2} < 0.3$  in  
805 the  $\eta - \phi$  plane. The isolation is evaluated in terms of  $\mathcal{I}^\mu < 0.35$ , defined as:

$$\mathcal{I}^\mu \equiv \left( \sum p_T^{\text{charged}} + \max \left[ 0, \sum p_T^{\text{neutral}} + \sum p_T^\gamma - p_T^{\text{PU}}(\mu) \right] \right) / p_T^\mu. \quad (4.3)$$

806 The  $\sum p_T^{\text{charged}}$  is the scalar sum of the transverse momenta of charged hadrons originating from the  
807 chosen primary vertex of the event. The  $\sum p_T^{\text{neutral}}$  and  $\sum p_T^\gamma$  are the scalar sums of the transverse  
808 momenta for neutral hadrons and photons, respectively. Since the isolation variable is particularly  
809 sensitive to energy deposits from pileup interactions, a  $p_T^{\text{PU}}(\mu)$  contribution is subtracted, where  
810  $p_T^{\text{PU}}(\mu) \equiv 0.5 \times \sum_i p_T^{\text{PU},i}$ , where  $i$  runs over the momenta of the charged hadron PF candidates  
811 not originating from the primary vertex, and the factor of 0.5 corrects for the different fraction of  
812 charged and neutral particles in the cone.

813 One should keep in mind that this muon identification is the same as the one used by the  $H \rightarrow$   
 814  $ZZ^* \rightarrow 4l$  [53]. This was done in order to keep in phase with other Higgs analysis inside the  
 815 collaboration. After the muon identification, an appropriate scale factor is applied to the MC  
 816 events based on the leading muon  $p_T$  and  $\eta$ , in order to correct any possible discrepancy between  
 817 data and simulated samples. The scale factors were taken from the  $H \rightarrow ZZ^* \rightarrow 4l$  analysis.

818 In order to cope with trigger requirements, the leading muon should have  $p_T > 20$  GeV and the  
 819 trailing muon  $p_T > 4$  GeV.

### 820 4.5.3 Photon Identification

821 For the photon identification and selection, standard CMS . The Multivariate (MVA) Photon iden-  
 822 tification is used with a working point of 90%, together with a electron veto procedure, to avoid  
 823 misidentification of electrons as photons. Kinematically, the photons are requested to have trans-  
 824 verse energy, with respect to the beam line,  $E_T > 33$  GeV and reconstructed within the CMS  
 825 acceptance for photons  $|\eta_{SC}| < 2.5^5$ , excluding the Electromagnetic Calorimeter (ECAL) Barrel-  
 826 Endcap intersections.

827 The threshold of 33 GeV for the photon transverse energy is driven by the trigger requirements.  
 828 The selecte photon, per event, is the one with highest  $E_T$ .

### 829 4.5.4 Kinematical distributions

830 The selection described so far, is called Group I. The plots shown below are related to selected  
 831 events after this set.

832 Figures 4.4 to 4.9 presents the  $p_T$ ,  $\eta$  and  $\phi$  distributions for the leading muon, trailing muon and  
 833 the photon, for the Z decaying in  $\Upsilon(1S, 2S, 3S) + \gamma$ .

834 Figures 4.10 to 4.12 presents the  $p_T$ ,  $\eta$  and  $\phi$  distributions for reconstructed  $\Upsilon(nS)$  ( $\mu\mu$  system)  
 835 and the reconstructed boson ( $\mu\mu\gamma$  system).

836 Figures 4.13 to 4.16 presents the  $\Delta R = \sqrt{\Delta\eta^2 + \Delta\phi^2}$  between the photon and the muons, the  
 837  $\Delta R$  distributions between reconstructed dimuon ( $\mu\mu$ ) system and the photon, the absolute value  
 838 of the  $\Delta\phi$  between the leading muon and the photon, the ratio for the transverse momentum of  
 839 the reconstructed Upsilon and the reconstructed Z mass ( $p_T^{\mu\mu}/M_{\mu\mu\gamma}$ ), the ratio for the transverse  
 840 energy of the reconstructed Photon and the reconstructed Z mass ( $E_T^{\mu\mu}/M_{\mu\mu\gamma}$ ) and dimuon mass  
 841 distribution of the reconstructed  $\Upsilon(nS)$ .

842 Figures 4.17 to 4.29 present the same variables, but for the Higgs decaying in  $\Upsilon(1S, 2S, 3S) + \gamma$   
 843 channel.

---

<sup>5</sup>SC stands for Super Cluster of the reconstructed photon. It is the set of cell in the Electromagnetic Calorimeter used for the photon observation.

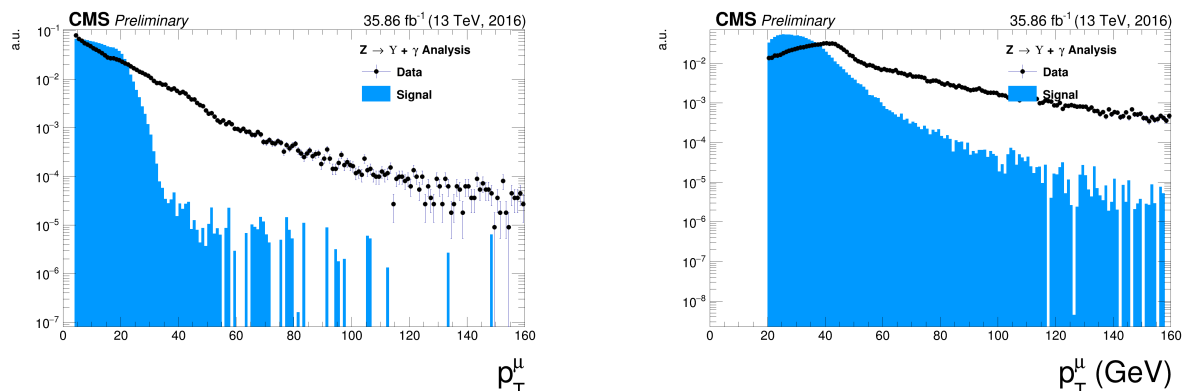


Figure 4.4: The  $p_T$  muon distributions from data and signal events for  $Z$  decaying in  $\Upsilon(1S, 2S, 3S) + \gamma$  after Group I of selection cuts, where on left are presenting the trailing muons and on right are the leading muons. The plots are normalized to the unit of area.

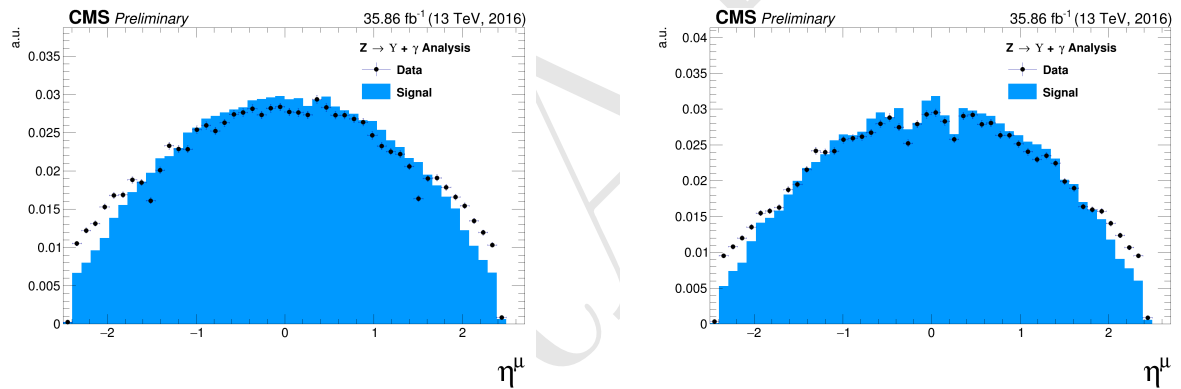


Figure 4.5: The  $\eta$  muon distributions from data and signal events of  $Z$  decaying in  $\Upsilon(1S, 2S, 3S) + \gamma$  after Group I of selection cuts, where on left are presenting the trailing muons and on right are the leading muons. The plots are normalized to the unit of area.

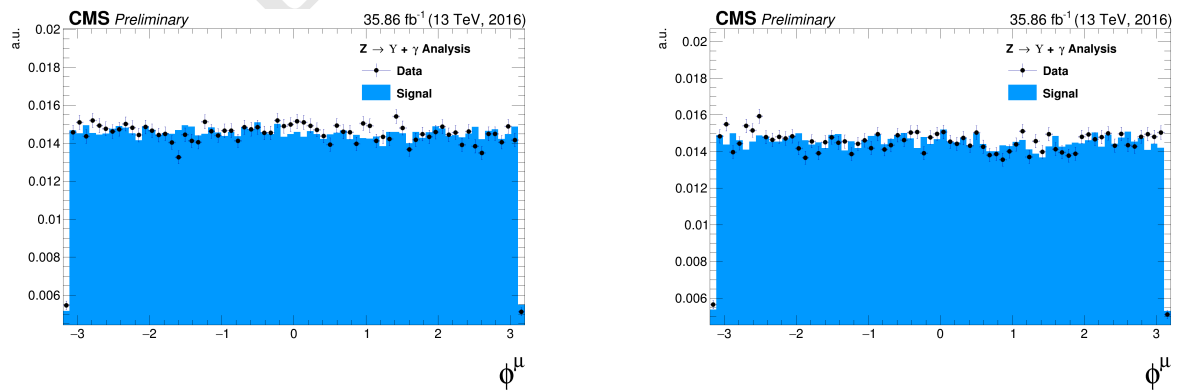


Figure 4.6: The  $\phi$  muon distributions from data and signal events of  $Z$  decaying in  $\Upsilon(1S, 2S, 3S) + \gamma$  after Group I of selection cuts, where on left are presenting the trailing muons and on right are the leading muons. The plots are normalized to the unit of area.

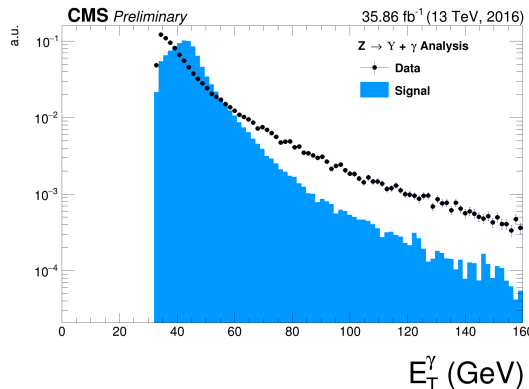


Figure 4.7: The  $p_T$  photon distributions from data and signal events for Z decaying in  $\Upsilon(1S, 2S, 3S) + \gamma$  Group I of selection cuts. The plots normalized to the unit of area.

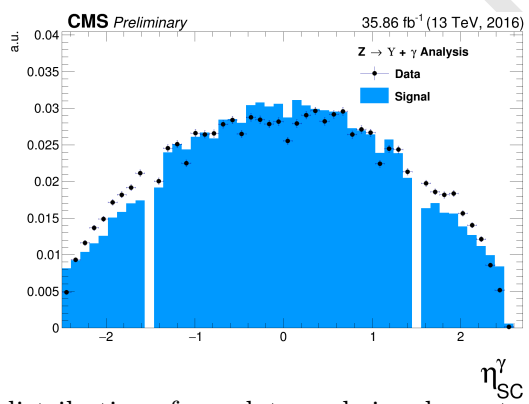


Figure 4.8: The  $\eta$  photon distributions from data and signal events of Z decaying in  $\Upsilon(1S, 2S, 3S) + \gamma$  after Group I of selection cuts. The plot is normalized to the unit of area.

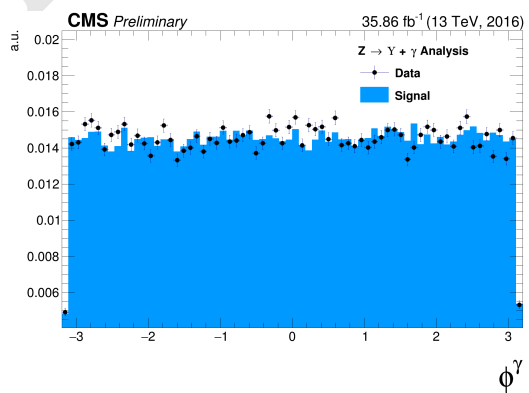


Figure 4.9: The  $\phi$  photon distributions from data and signal events of Z decaying in  $\Upsilon(1S, 2S, 3S) + \gamma$  after Group I of selection cuts. The plot is normalized to the unit of area.

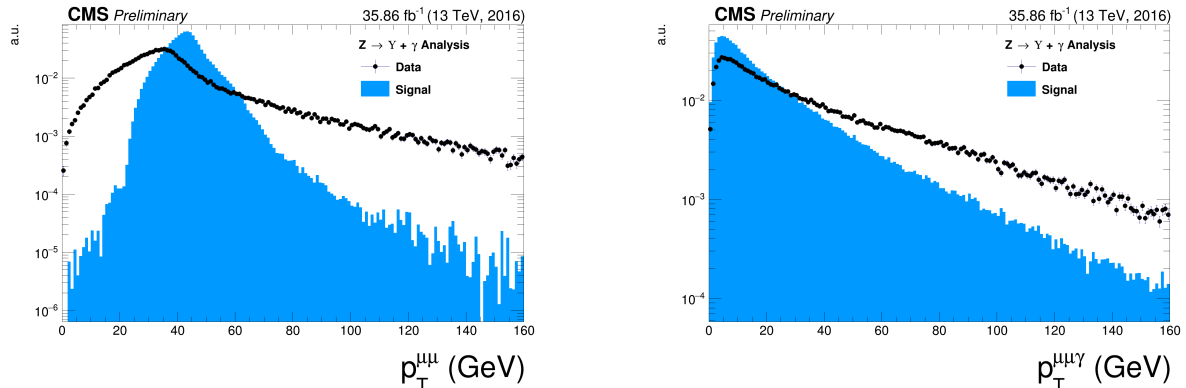


Figure 4.10: The  $p_T$  distributions for the reconstructed  $\Upsilon(1S, 2S, 3S)$  in the left and for  $Z$  in the right from data and signal events for  $Z$  decaying in  $\Upsilon(1S, 2S, 3S) + \gamma$  after Group I of selection cuts. The plots are normalized to the unit of area.

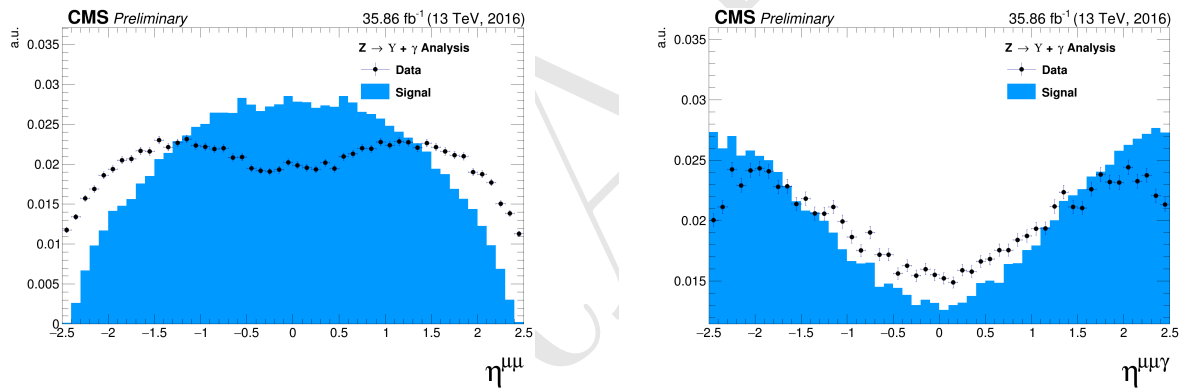


Figure 4.11: The  $\eta$  distributions for  $\Upsilon(1S, 2S, 3S)$  in the left and for  $Z$  in the right from data and signal events for  $Z$  decaying in  $\Upsilon(1S, 2S, 3S) + \gamma$  after Group I of selection cuts. The plots are normalized to the unit of area.

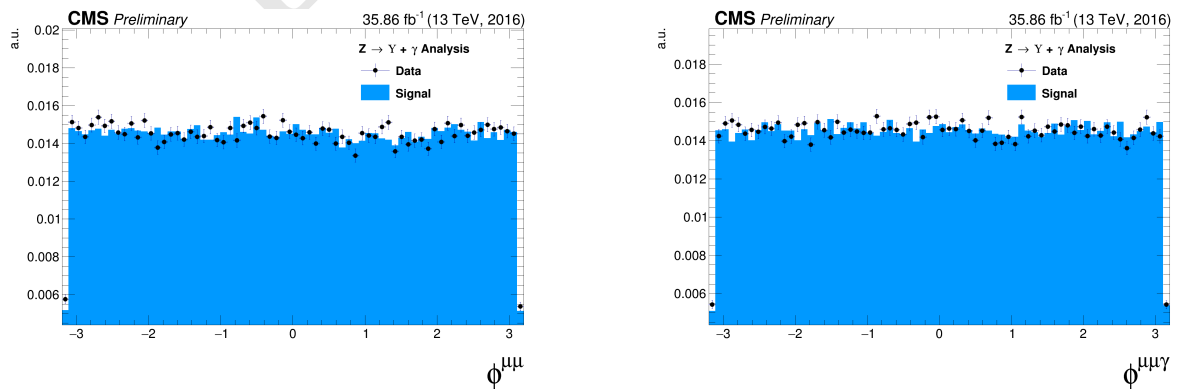


Figure 4.12: The  $\phi$  distributions for  $\Upsilon(1S, 2S, 3S)$  in the left and for  $Z$  in the right from data and signal events for  $Z$  decaying in  $\Upsilon(1S, 2S, 3S) + \gamma$  after Group I of selection cuts. The plots are normalized to the unit of area.

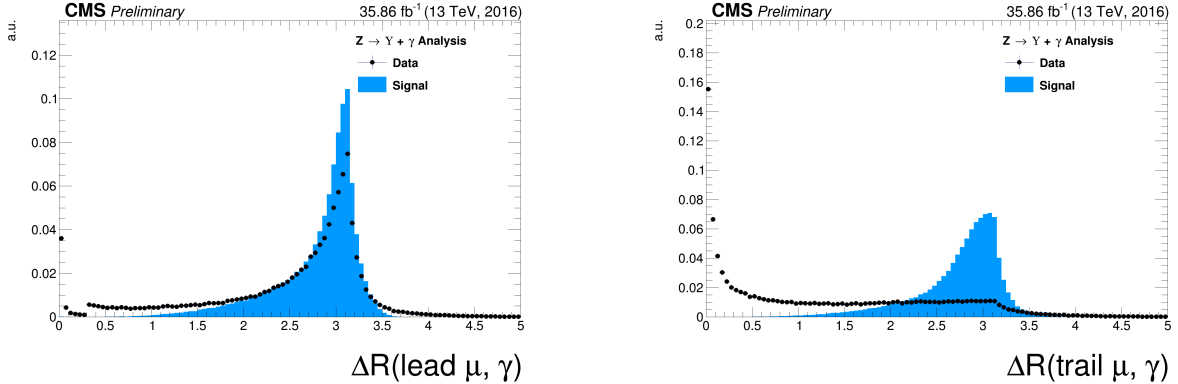


Figure 4.13: The  $\Delta R$  distributions between the photon and the leading muon (left) and the trailing muon (right) for for Z decaying in  $\Upsilon(1S, 2S, 3S) + \gamma$  from data and signal events after Group I of selection cuts. The plots are normalized to the unit of area.

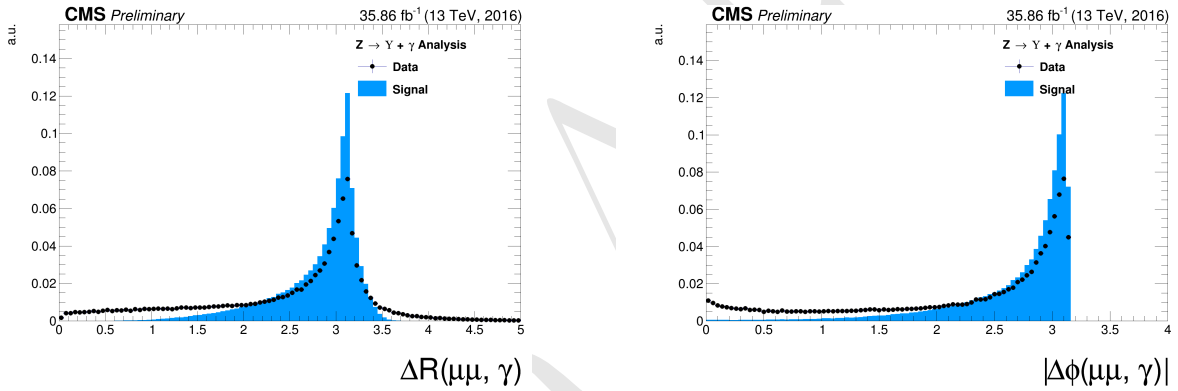


Figure 4.14: Left: The  $\Delta R$  distributions between reconstructed dimuon ( $\mu\mu$ ) system and the photon. Right: absolute value of the  $\Delta\phi$  between the leading muon and the photon for for Z decaying in  $\Upsilon(1S, 2S, 3S) + \gamma$  from data and signal events after Group I of selection cuts. The plots are normalized to the unit of area.

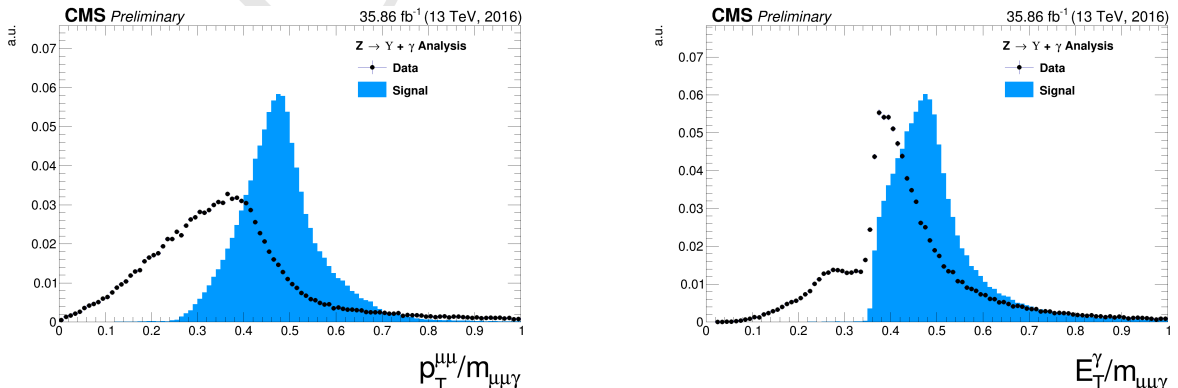


Figure 4.15: The ratio for the transverse momentum of the reconstructed Upsilon and the reconstructed Z mass ( $p_T^{\mu\mu}/M_{\mu\mu\gamma}$  - left) and the ratio for the transverse energy of the reconstructed Photon and the reconstructed Z mass ( $E_T^\gamma/M_{\mu\mu\gamma}$  - right) distribution for Z decaying in  $\Upsilon(1S, 2S, 3S) + \gamma$  from data and signal events after Group I of selection cuts. The plots are normalized to the unit of area.

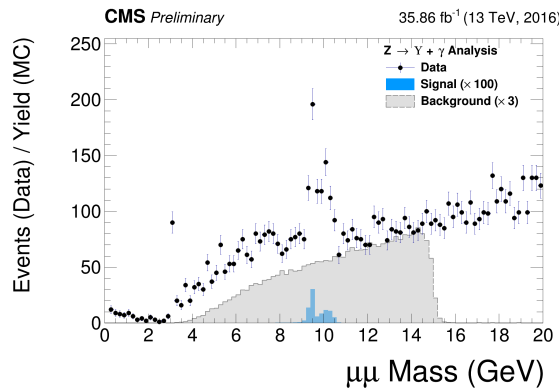


Figure 4.16: The dimuon mass distribution of the reconstructed  $\Upsilon(1S, 2S, 3S)$  from data and signal events for  $Z$  decaying after Group I of selection cuts. The plot is normalized to the number of events. "Signal" stands for the  $Z \rightarrow \Upsilon(1S, 2S, 3S) + \gamma$  sample (scaled by a factor of  $\times 100$ ) and "Background" corresponds to the peaking background ( $Z \rightarrow \mu\mu\gamma_{FSR}$ ) sample (scaled by a factor of  $\times 3$ ).

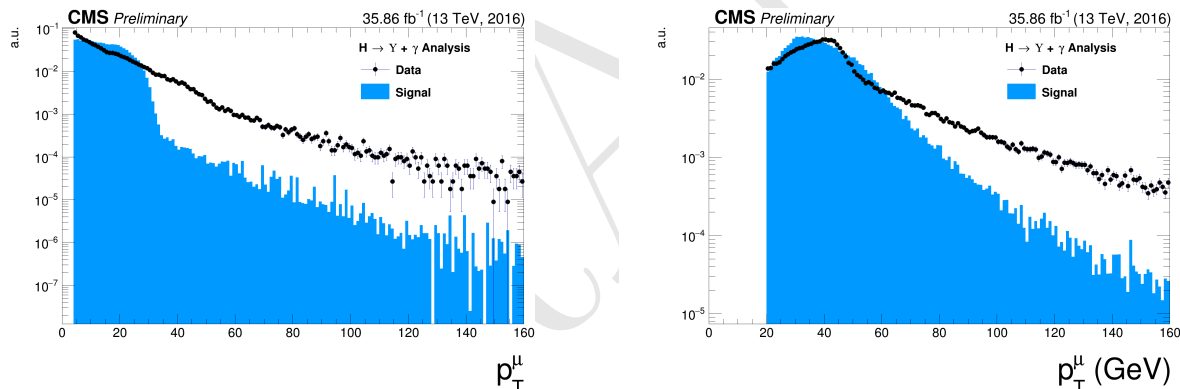


Figure 4.17: The  $p_T$  muon distributions from data and signal events for Higgs decaying in  $\Upsilon(1S, 2S, 3S) + \gamma$  after Group I of selection cuts, where on left are presenting the trailing muons and on right are the leading muons. The plots are normalized to the unit of area.

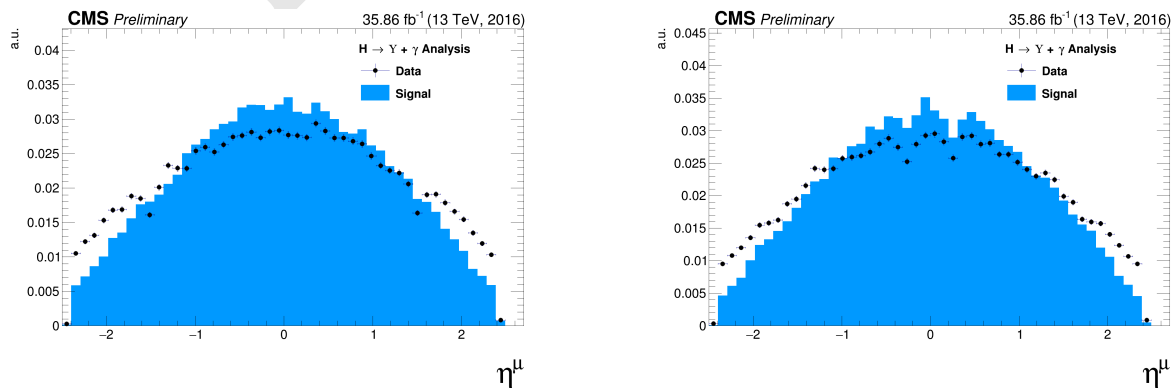


Figure 4.18: The  $\eta$  muon distributions from data and signal events of Higgs decaying in  $\Upsilon(1S, 2S, 3S) + \gamma$  after Group I of selection cuts, where on left are presenting the trailing muons and on right are the leading muons. The plots are normalized to the unit of area.

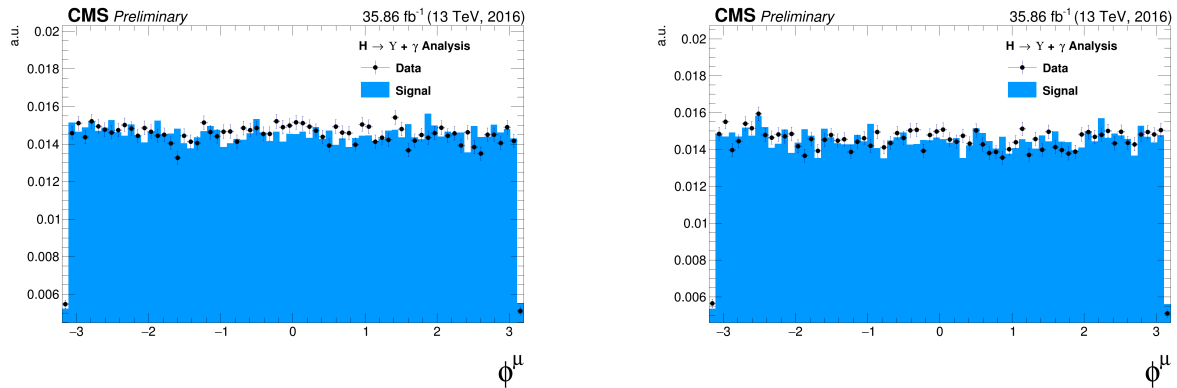


Figure 4.19: The  $\phi$  muon distributions from data and signal events of Higgs decaying in  $\Upsilon(1S, 2S, 3S) + \gamma$  after Group I of selection cuts, where on left are presenting the trailing muons and on right are the leading muons. The plots are normalized to the unit of area.

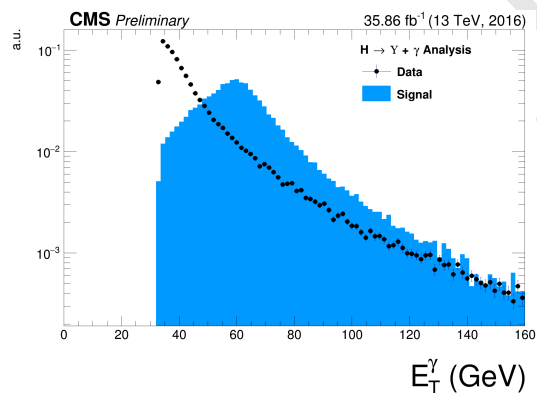


Figure 4.20: The  $p_T$  photon distributions from data and signal events for Higgs decaying in  $\Upsilon(1S, 2S, 3S) + \gamma$  Group I of selection cuts. The plot is normalized to the unit of area.

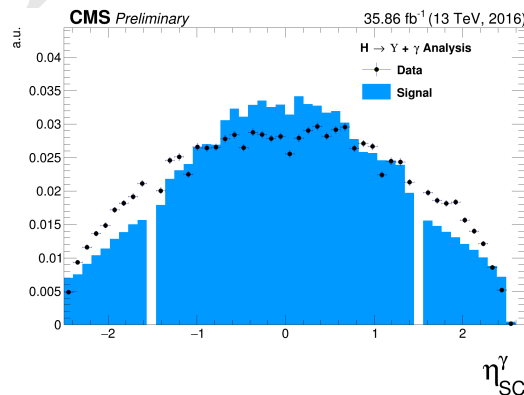


Figure 4.21: The  $\eta$  photon distributions from data and signal events of Higgs decaying in  $\Upsilon(1S, 2S, 3S) + \gamma$  after Group I of selection cuts. The plot is normalized to the unit of area.

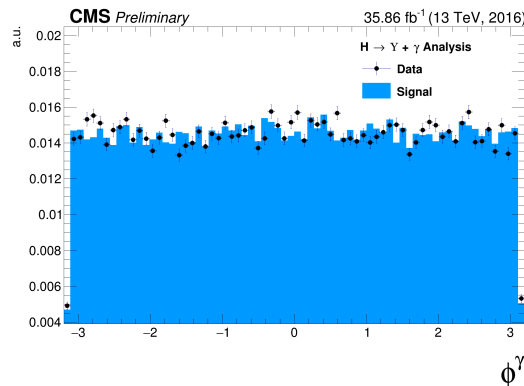


Figure 4.22: The  $\phi$  photon distributions from data and signal events of Higgs decaying in  $\Upsilon(1S, 2S, 3S) + \gamma$  after Group I of selection cuts. The plot is normalized to the unit of area.

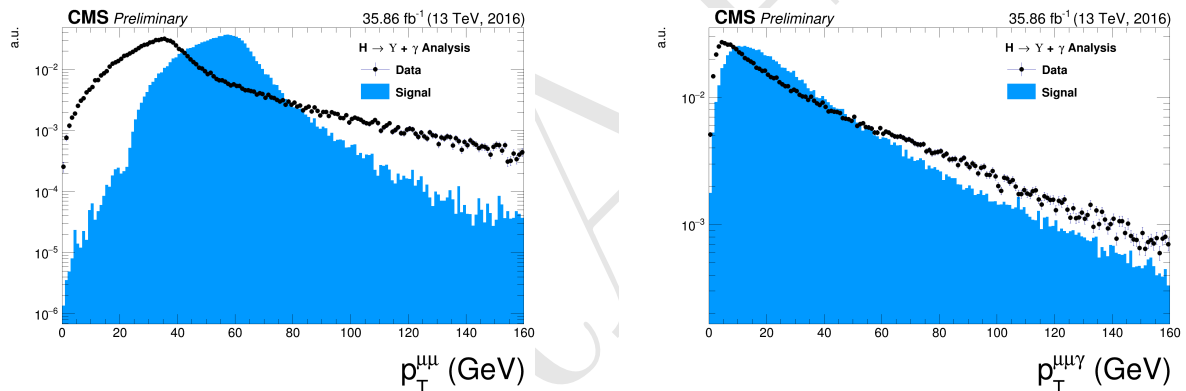


Figure 4.23: The  $p_T$  distributions for  $\Upsilon(1S, 2S, 3S)$  in the left and for Higgs in the right from data and signal events for Higgs decaying in  $\Upsilon(1S, 2S, 3S) + \gamma$  after Group I of selection cuts. The plots are normalized to the unit of area.

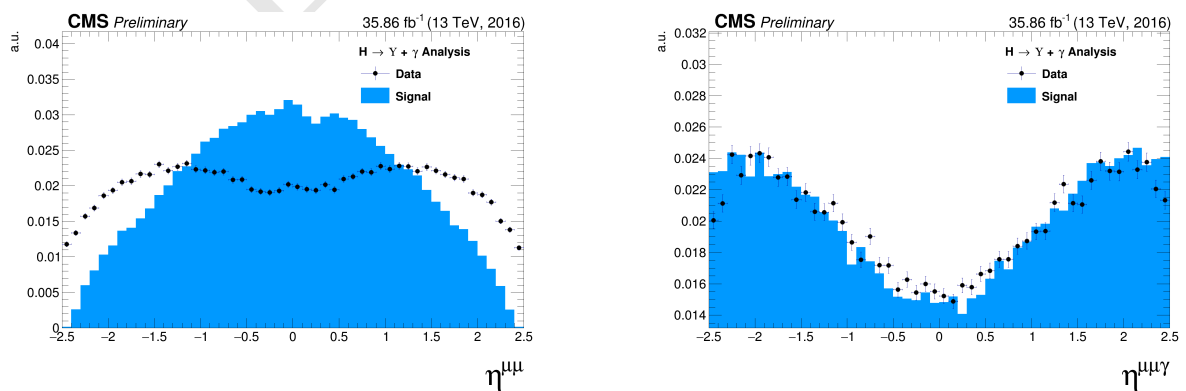


Figure 4.24: The  $\eta$  distributions for  $\Upsilon(1S, 2S, 3S)$  in the left and for Higgs in the right from data and signal events for Higgs decaying in  $\Upsilon(1S, 2S, 3S) + \gamma$  after Group I of selection cuts. The plots are normalized to the unit of area.

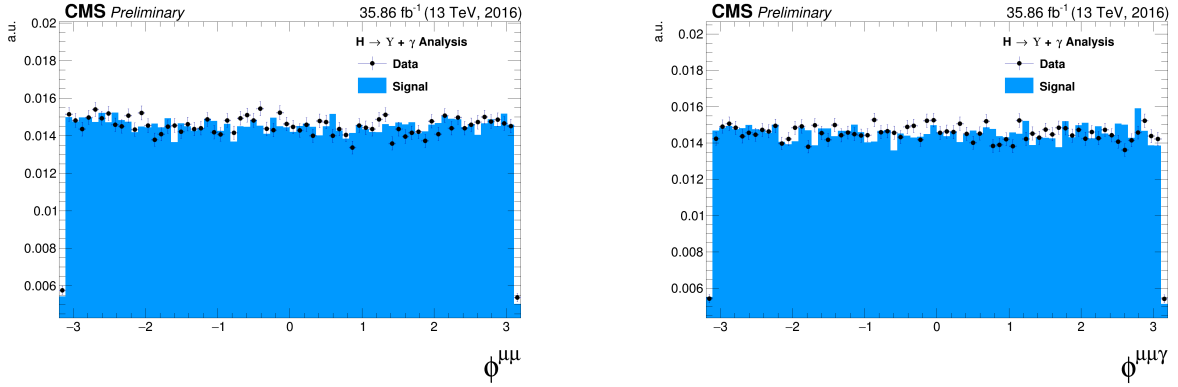


Figure 4.25: The  $\phi$  distributions for  $\Upsilon(1S, 2S, 3S)$  in the left and for Higgs in the right from data and signal events for Higgs decaying in  $\Upsilon(1S, 2S, 3S) + \gamma$  after Group I of selection cuts. The plots are normalized to the unit of area.

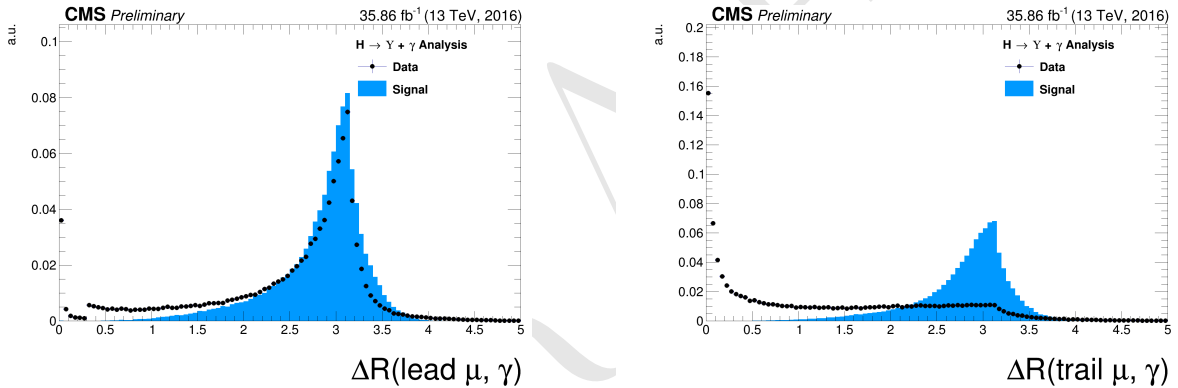


Figure 4.26: The  $\Delta R$  distributions between the photon and the leading muon (left) and the trailing muon (right) for Higgs decaying in  $\Upsilon(1S, 2S, 3S) + \gamma$  from data and signal events after Group I of selection cuts. The plots are normalized to the unit of area.

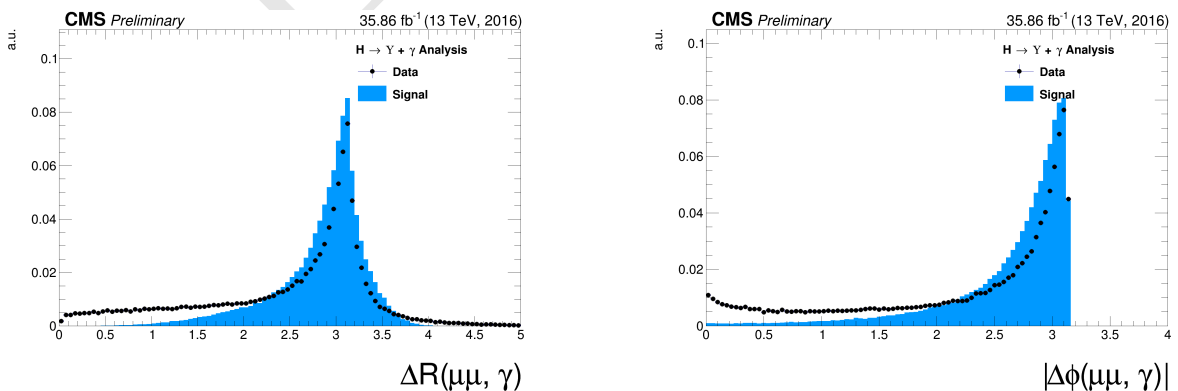


Figure 4.27: Left: The  $\Delta R$  distributions between reconstructed dimuon ( $\mu\mu$ ) system and the photon. Right: absolute value of the  $\Delta\phi$  between the leading muon and the photon for Higgs decaying in  $\Upsilon(1S, 2S, 3S) + \gamma$  from data and signal events after Group I of selection cuts. The plots are normalized to the unit of area.

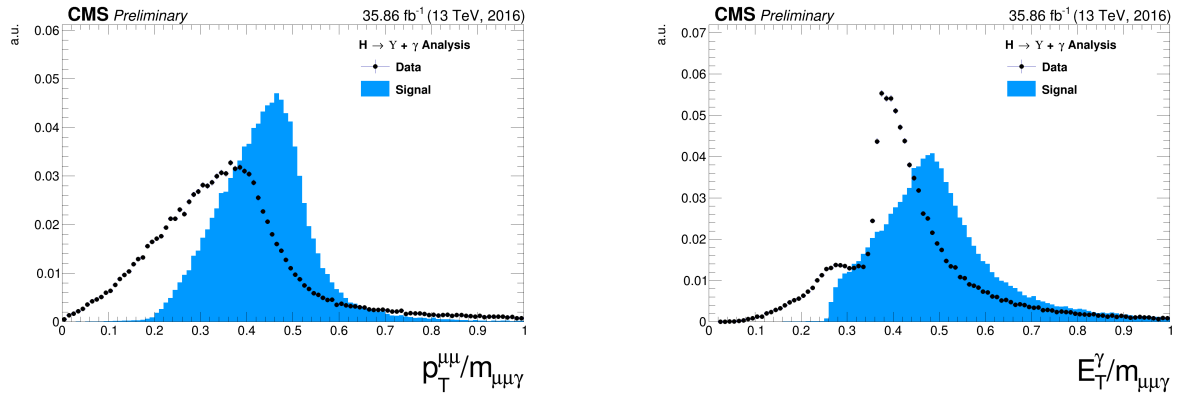


Figure 4.28: The ratio for the transverse momentum of the reconstructed Upsilon and the reconstructed Higgs mass ( $p_T^{\mu\mu}/M_{\mu\mu\gamma}$  - left) and the ratio for the transverse energy of the reconstructed Photon and the reconstructed Higgs mass ( $E_T^\gamma/M_{\mu\mu\gamma}$  - right) distribution for Higgs decaying in  $\Upsilon(1S, 2S, 3S) + \gamma$  from data and signal events after Group I of selection cuts. The plots are normalized to the unit of area.

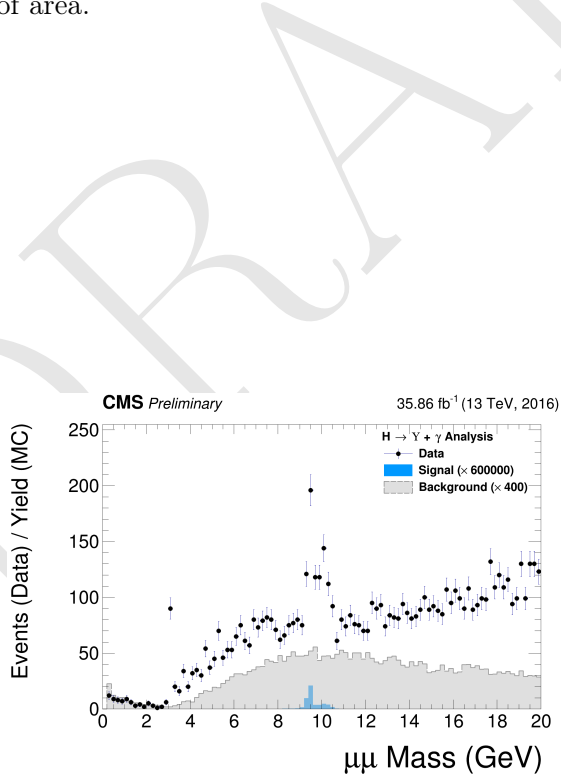


Figure 4.29: The dimuon mass distribution of the reconstructed  $\Upsilon(1S, 2S, 3S)$  from data and signal events for Higgs decaying after Group I of selection cuts. This plot is normalized the expected number of events. The plot is normalized to the number of events. "Signal" stands for the  $H \rightarrow \Upsilon(1S, 2S, 3S) + \gamma$  sample (scaled by a factor of  $\times 60000$ ) and "Background" corresponds to the peaking background (Higgs Dalitz Decay) sample (scaled by a factor of  $\times 400$ ).

## 4.6 Kinematical selection (Group II)

After all Trigger and Object Identification cuts, described in before (**Group I**), a set of kinematical cuts are applied in order to improve the signal to background relation. They are

- $\Delta R(\text{leading } \mu, \gamma) > 1$ ;
- $\Delta R(\text{trailing } \mu, \gamma) > 1$ ;
- $\Delta R(\mu\mu, \gamma) > 2$ ;
- $|\Delta\phi(\text{leading } \mu, \gamma)| > 1.5$ ;
- $8.4 \text{ GeV} < M_{\mu\mu} < 11.1 \text{ GeV}$ ;
- $E_T^\gamma/M_{\mu\mu\gamma} > 35/91.2$  for the Z decay or  $35/125$  for the Higgs decay;
- $p_T^{\mu\mu}/M_{\mu\mu\gamma} > 35/91.2$  for the Z decay or  $35/125$  for the Higgs decay.

The choice of these thresholds were based on the visual inspection of the distributions (besides the invariant mass distribution of the dimuon system  $M_{\mu\mu}$ , which needs to be defined around the  $\nu(1S, 2S, 3S)$  mass) and to keep this analysis in phase with other similar analysis within CMS.

Below it is shown the same set of plot shown before, but this time, taking into account the full selection (**Group I+II**).

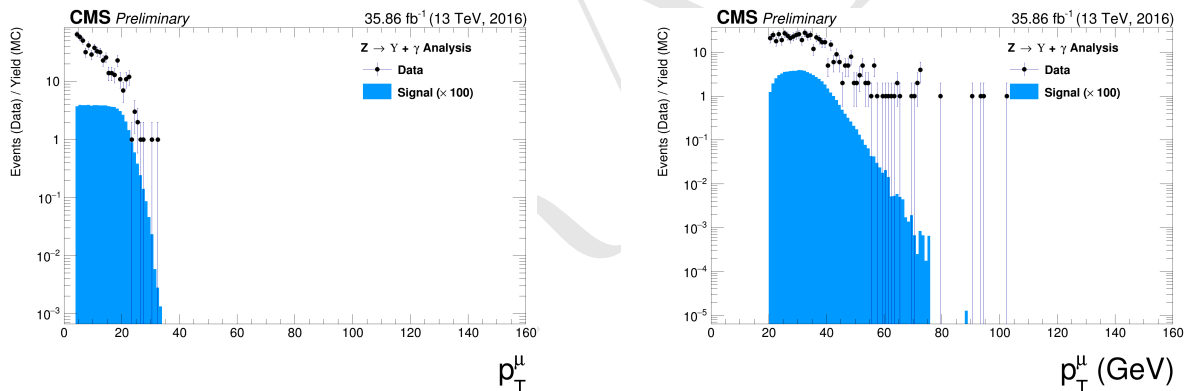


Figure 4.30: The  $p_T$  muon distributions from data and signal events for Z decaying in  $\Upsilon(1S, 2S, 3S) + \gamma$  after Group I of selection cuts, where on left are presenting the trailing muons and on right are the leading muons. The plots are normalized to the number of events. Signal sample is scaled by a factor of  $\times 100$ .

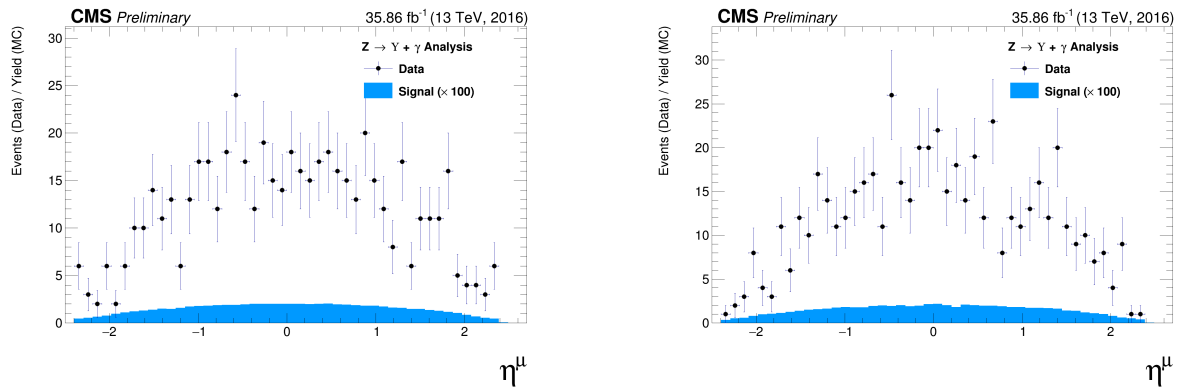


Figure 4.31: The  $\eta$  muon distributions from data and signal events of Z decaying in  $\Upsilon(1S, 2S, 3S) + \gamma$  after Group I of selection cuts, where on left are presenting the trailing muons and on right are the leading muons. The plots are normalized to the number of events. Signal sample is scaled by a factor of  $\times 100$ .

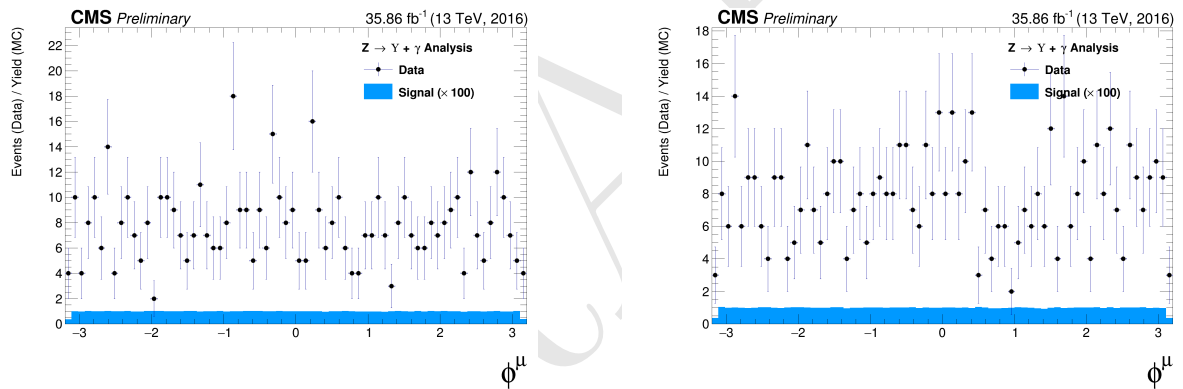


Figure 4.32: The  $\phi$  muon distributions from data and signal events of Z decaying in  $\Upsilon(1S, 2S, 3S) + \gamma$  after Group I of selection cuts, where on left are presenting the trailing muons and on right are the leading muons. The plots are normalized to the number of events. Signal sample is scaled by a factor of  $\times 100$ .

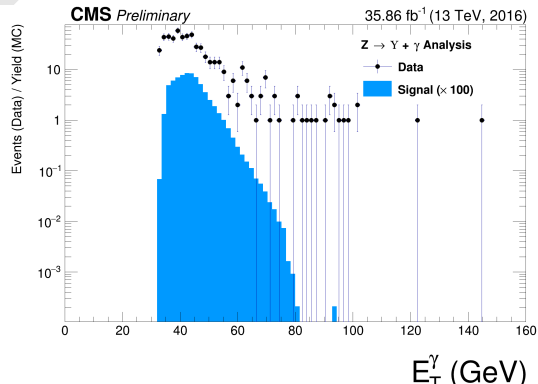


Figure 4.33: The  $p_T$  photon distributions from data and signal events for Z decaying in  $\Upsilon(1S, 2S, 3S) + \gamma$  all (Group I+II) selection cuts. The plot is normalized to the number of events. Signal sample is scaled by a factor of  $\times 100$ .

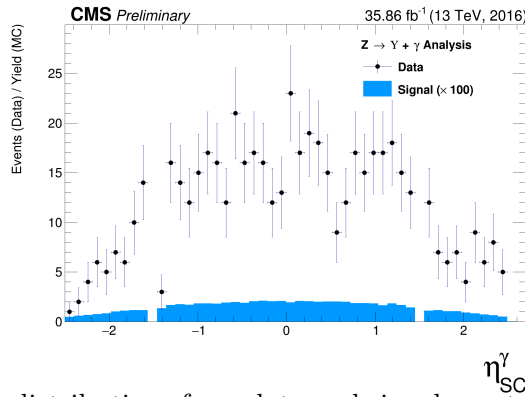


Figure 4.34: The  $\eta$  photon distributions from data and signal events of Z decaying in  $\Upsilon(1S, 2S, 3S) + \gamma$  after all (Group I+II) selection cuts. The plot is normalized to the number of events. Signal sample is scaled by a factor of  $\times 100$ .

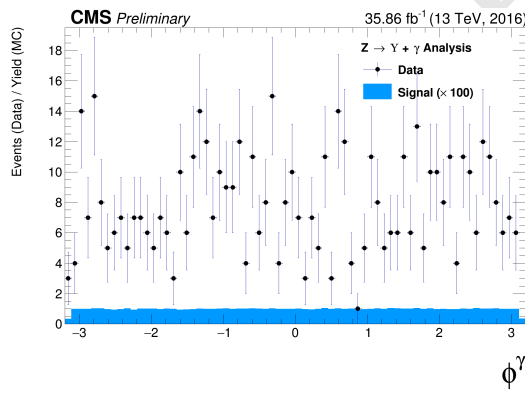


Figure 4.35: The  $\phi$  photon distributions from data and signal events of Z decaying in  $\Upsilon(1S, 2S, 3S) + \gamma$  after all (Group I+II) selection cuts. The plot is normalized to the number of events. Signal sample is scaled by a factor of  $\times 100$ .

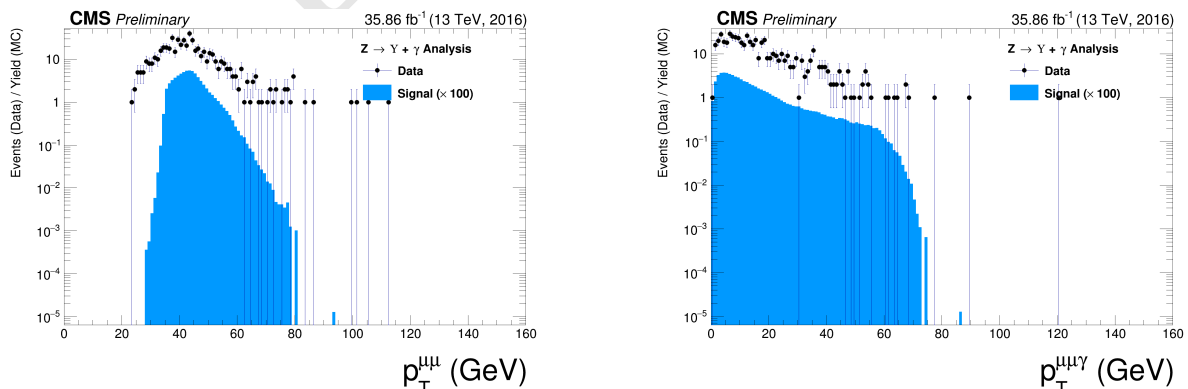


Figure 4.36: The  $p_T$  distributions for  $\Upsilon(1S, 2S, 3S)$  in the left and for Z in the right from data and signal events for Z decaying in  $\Upsilon(1S, 2S, 3S) + \gamma$  after all (Group I+II) selection cuts. The plots are normalized to the number of events. Signal sample is scaled by a factor of  $\times 100$ .

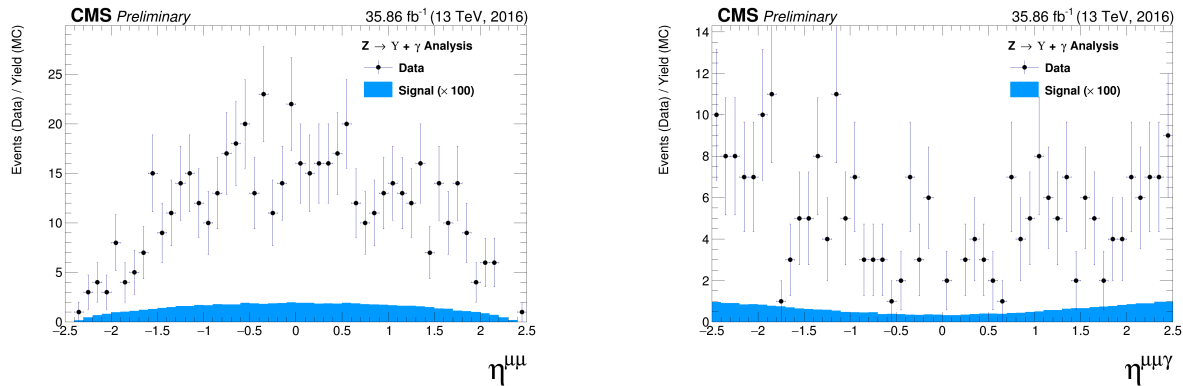


Figure 4.37: The  $\eta$  distributions for  $\Upsilon(1S, 2S, 3S)$  in the left and for  $Z$  in the right from data and signal events for  $Z$  decaying in  $\Upsilon(1S, 2S, 3S) + \gamma$  after all (Group I+II) selection cuts. The plots are normalized to the number of events. Signal sample is scaled by a factor of  $\times 100$ .

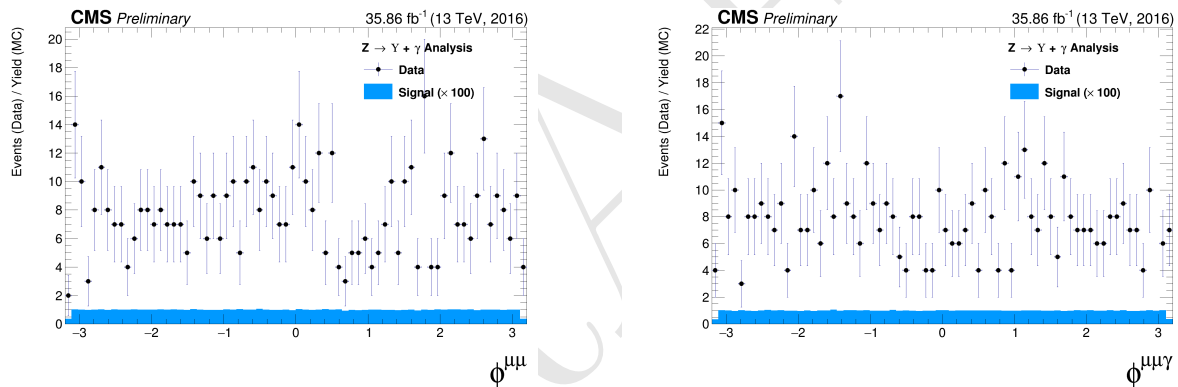


Figure 4.38: The  $\phi$  distributions for  $\Upsilon(1S, 2S, 3S)$  in the left and for  $Z$  in the right from data and signal events for  $Z$  decaying in  $\Upsilon(1S, 2S, 3S) + \gamma$  after all (Group I+II) selection cuts. The plots are normalized to the number of events. Signal sample is scaled by a factor of  $\times 100$ .

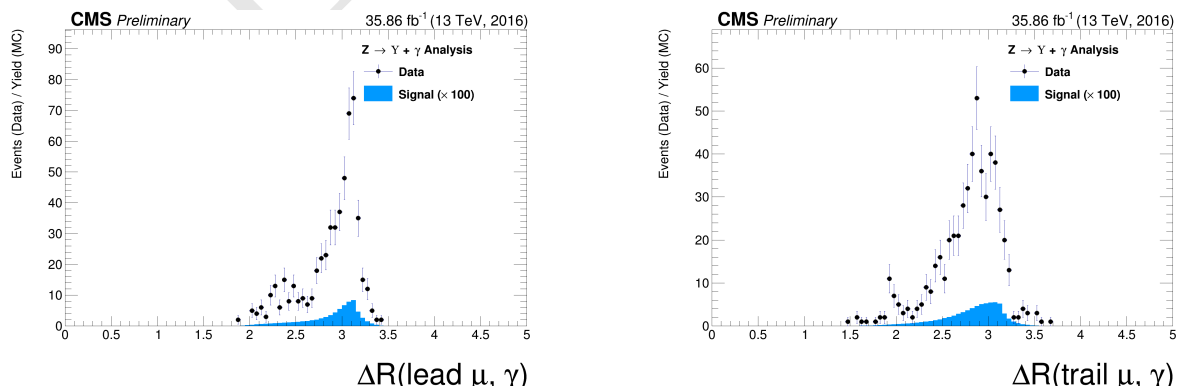


Figure 4.39: The  $\Delta R$  distributions between the photon and the leading muon (left) and the trailing muon (right) for  $\Upsilon(1S, 2S, 3S)$  from data and signal events for  $Z$  decaying after all (Group I+II) selection cuts. The plots are normalized to the number of events. Signal sample is scaled by a factor of  $\times 100$ .

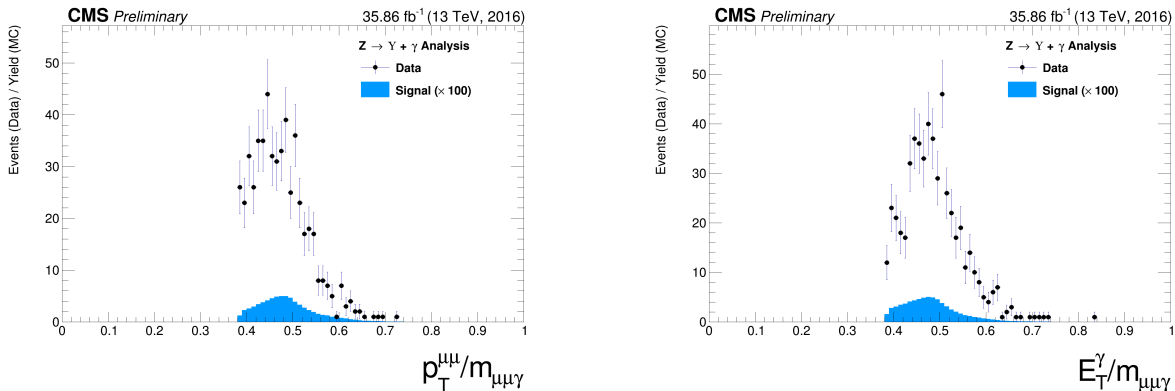


Figure 4.40: The ratio for the transverse momentum of the reconstructed Upsilon and the reconstructed Z mass ( $p_T^{\mu\mu}/M_{\mu\mu\gamma}$  - left) and the ratio for the transverse energy of the reconstructed Photon and the reconstructed Z mass ( $E_T^\gamma/M_{\mu\mu\gamma}$  - right) distribution for  $\Upsilon(1S, 2S, 3S)$  from data and signal events for Z decaying after all (Group I+II) selection cuts. The plots are normalized to the number of events. Signal sample is scaled by a factor of  $\times 100$ .

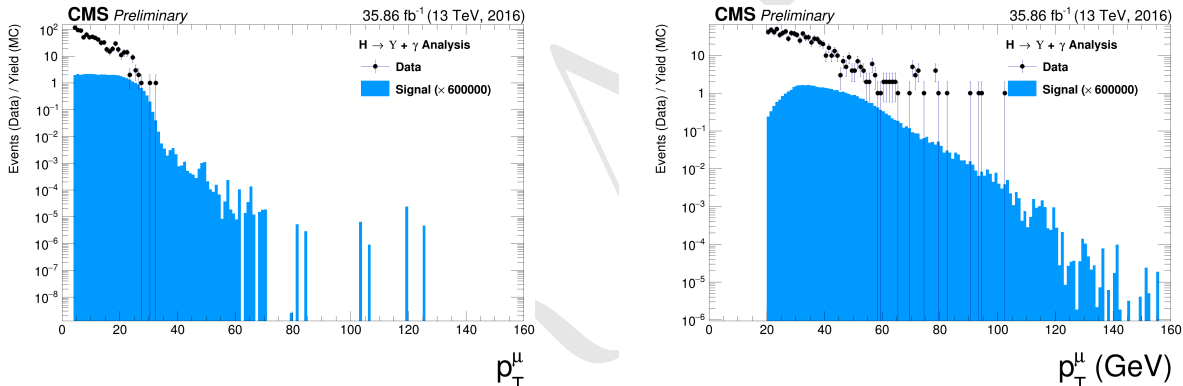


Figure 4.41: The  $p_T$  muon distributions from data and signal events for Higgs decaying in  $\Upsilon(1S, 2S, 3S) + \gamma$  after Group I of selection cuts, where on left are presenting the trailing muons and on right are the leading muons. The plots are normalized to the number of events. Signal sample is scaled by a factor of  $\times 600000$ .

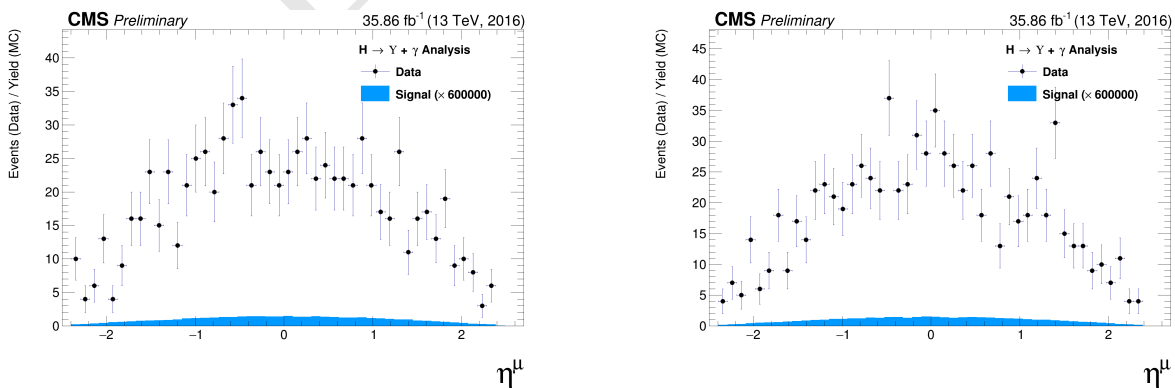


Figure 4.42: The  $\eta$  muon distributions from data and signal events of Higgs decaying in  $\Upsilon(1S, 2S, 3S) + \gamma$  after Group I of selection cuts, where on left are presenting the trailing muons and on right are the leading muons. The plots are normalized to the number of events. Signal sample is scaled by a factor of  $\times 600000$ .

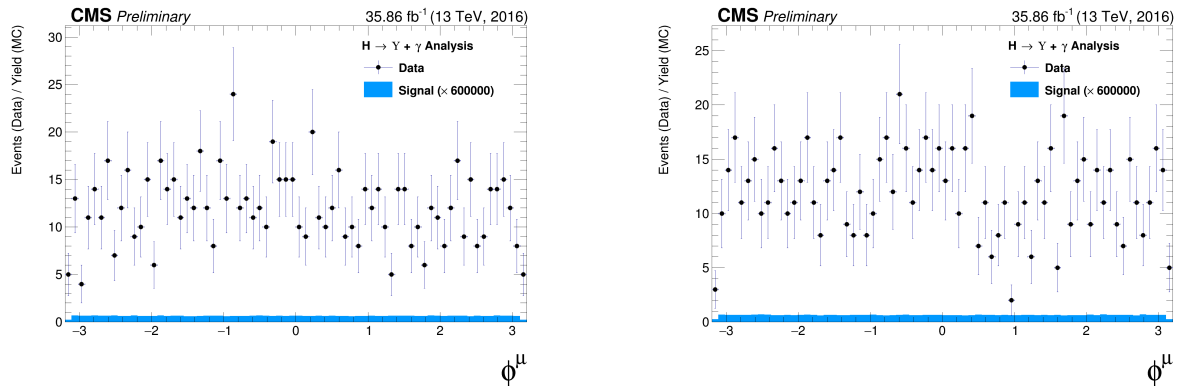


Figure 4.43: The  $\phi$  muon distributions from data and signal events of Higgs decaying in  $\Upsilon(1S, 2S, 3S) + \gamma$  after Group I of selection cuts, where on left are presenting the trailing muons and on right are the leading muons. The plots are normalized to the number of events. Signal sample is scaled by a factor of  $\times 600000$ .

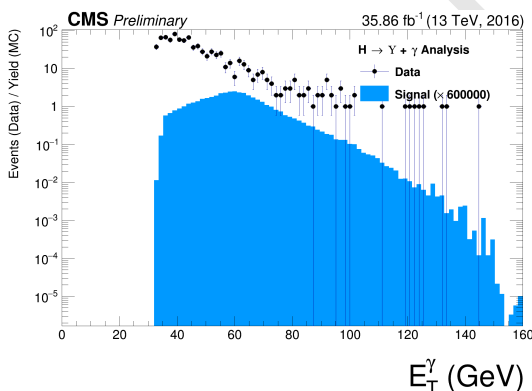


Figure 4.44: The  $p_T$  photon distributions from data and signal events for Higgs decaying in  $\Upsilon(1S, 2S, 3S) + \gamma$  all (Group I+II) selection cuts. The plot is normalized to the number of events. Signal sample is scaled by a factor of  $\times 600000$ .

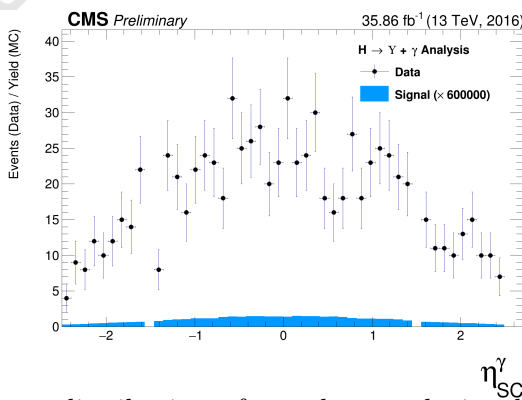


Figure 4.45: The  $\eta$  photon distributions from data and signal events of Higgs decaying in  $\Upsilon(1S, 2S, 3S) + \gamma$  after all (Group I+II) selection cuts. The plot is normalized to the number of events. Signal sample is scaled by a factor of  $\times 600000$ .

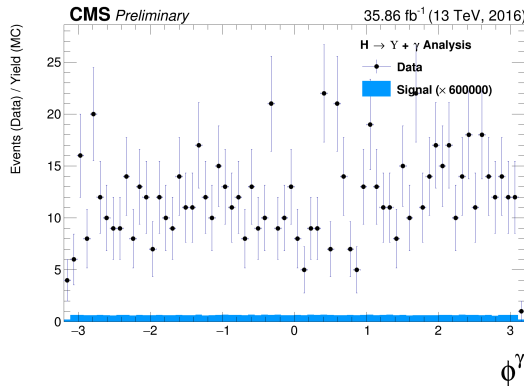


Figure 4.46: The  $\phi$  photon distributions from data and signal events of Higgs decaying in  $\Upsilon(1S, 2S, 3S) + \gamma$  after all (Group I+II) selection cuts. The plot is normalized to the number of events. Signal sample is scaled by a factor of c).

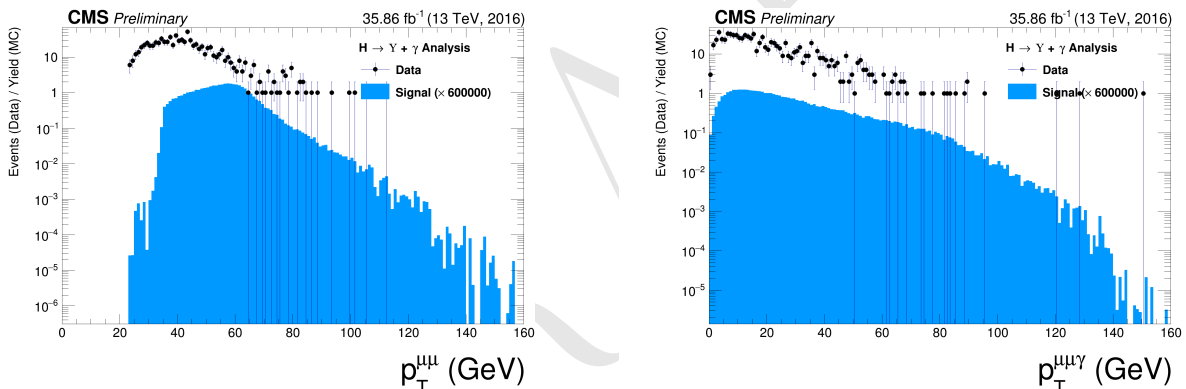


Figure 4.47: The  $p_T$  distributions for  $\Upsilon(1S, 2S, 3S)$  in the left and for Higgs in the right from data and signal events for Higgs decaying in  $\Upsilon(1S, 2S, 3S) + \gamma$  after all (Group I+II) selection cuts. The plots are normalized to the number of events. Signal sample is scaled by a factor of  $\times 600000$ .

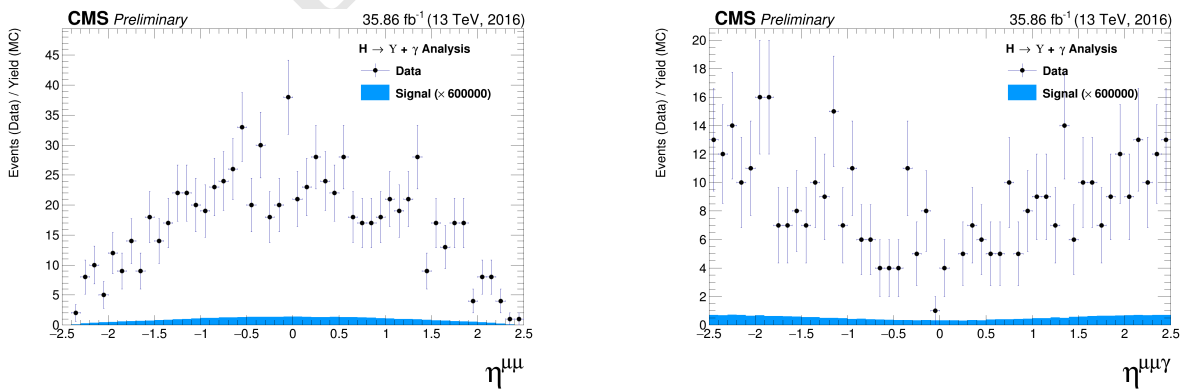


Figure 4.48: The  $\eta$  distributions for  $\Upsilon(1S, 2S, 3S)$  in the left and for Higgs in the right from data and signal events for Higgs decaying in  $\Upsilon(1S, 2S, 3S) + \gamma$  after all (Group I+II) selection cuts. The plots are normalized to the number of events. Signal sample is scaled by a factor of  $\times 600000$ .

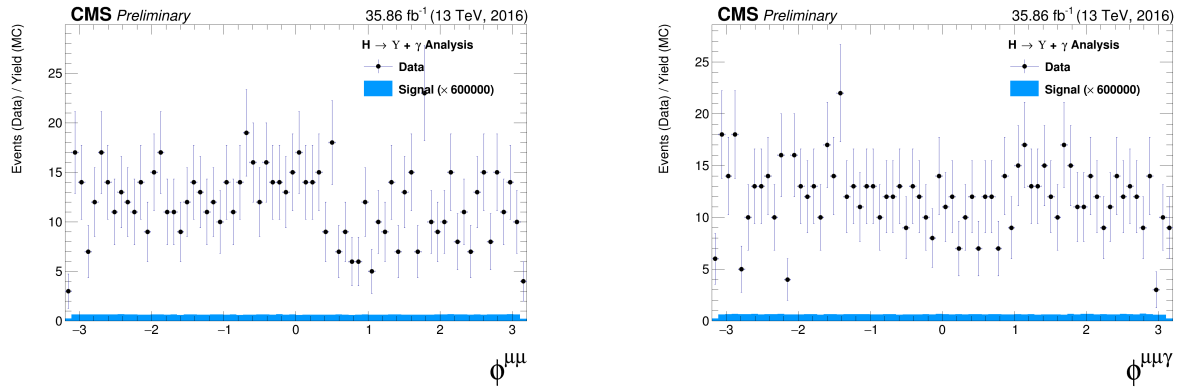


Figure 4.49: The  $\phi$  distributions for  $\Upsilon(1S, 2S, 3S)$  in the left and for Higgs in the right from data and signal events for Higgs decaying in  $\Upsilon(1S, 2S, 3S) + \gamma$  after all (Group I+II) selection cuts. The plots are normalized to the number of events. Signal sample is scaled by a factor of  $\times 600000$ .

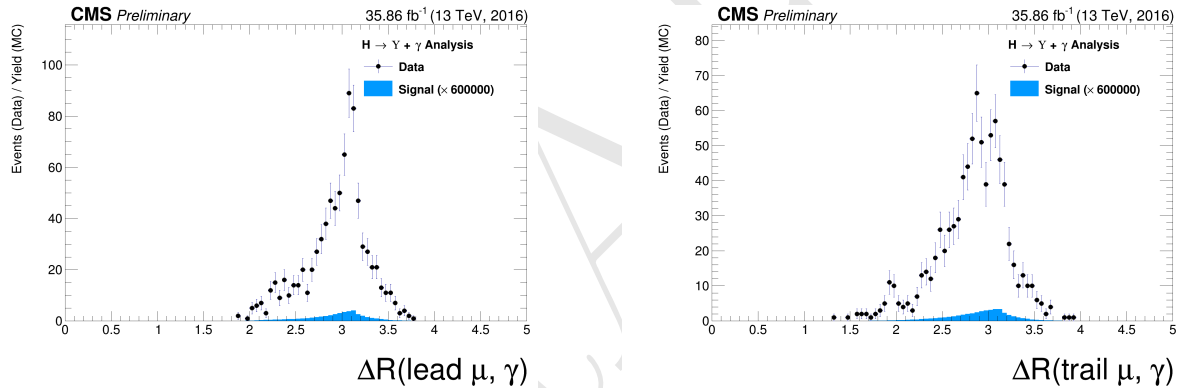


Figure 4.50: The  $\Delta R$  distributions between the photon and the leading muon (left) and the trailing muon (right) for  $\Upsilon(1S, 2S, 3S)$  from data and signal events for Higgs decaying after all (Group I+II) selection cuts. The plots are normalized to the number of events. Signal sample is scaled by a factor of  $\times 600000$ .

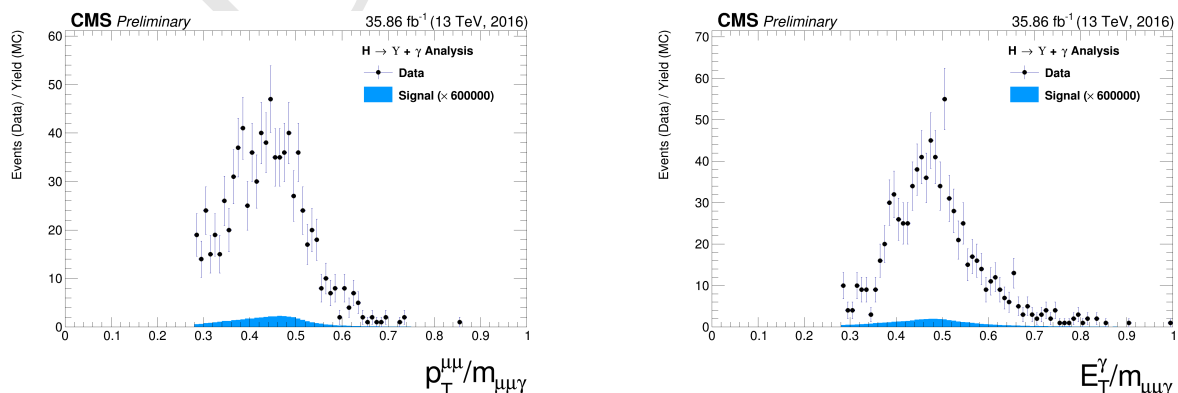


Figure 4.51: The ratio for the transverse momentum of the reconstructed Upsilon and the reconstructed Higgs mass ( $p_T^{\mu\mu}/M_{\mu\mu\gamma}$  - left) and the ratio for the transverse energy of the reconstructed Photon and the reconstructed Higgs mass ( $E_T^\gamma/M_{\mu\mu\gamma}$  - right) distribution for  $\Upsilon(1S, 2S, 3S)$  from data and signal events for Higgs decaying after all (Group I+II) selection cuts. The plots are normalized to the number of events. Signal sample is scaled by a factor of  $\times 600000$ .

## 4.7 Event categorization and yields

In order to increase the sensibility of the analysis, a categorization procedure was applied. They are based on the  $\eta$  and R9 distribution of the reconstructed photon.

The photon R9 is a shower shape variable defined as the fraction of energy deposited in the 5x5 square surrounding the Super Cluster seed of the reconstructed photon. A photon that convert before reaching the ECAL tend to have lower values of R9, in comparison with unconverted photons. Converted photons have wider energy resolution and are more likely to be misidentified.

Selected events with the photon reconstructed inside the barrel and with  $R9 > 0.94$  are categorized as "EB High R9"<sup>6</sup>, selected events with the photon reconstructed inside the barrel and with  $R9 < 0.94$  are categorized as "EB Low R9" and selected events with the photon reconstructed inside the endcap, regardless of its R9 value, categorized as "EE". This categorization is done in view of increase the analysis sensitivity.

This categorization is implemented only for the Z decay. The Higgs does not present enough statistics to make it profitable, so only the inclusive one is used.

### 4.7.1 R9 reweighting

As spotted by the  $H \rightarrow \gamma\gamma$  at  $\sqrt{13}$  TeV analysis [54], there is a disagreement in the R9 distribution of photons in Data and MC. In order to mitigate this difference, a transformation factor is extracted and applied to the reconstructed photons before the categorization.

The same approach of the  $H \rightarrow \gamma\gamma$  analysis is applied, in which the nominal photon selection of this analysis (see section 4.5.3) is used to select photons on Data and MC. Then the two distributions are remapped and the transformation factors are extracted.

Figure 4.52 show the R9 distribution before and after the reweighting, for the Barrel and the Endcap.

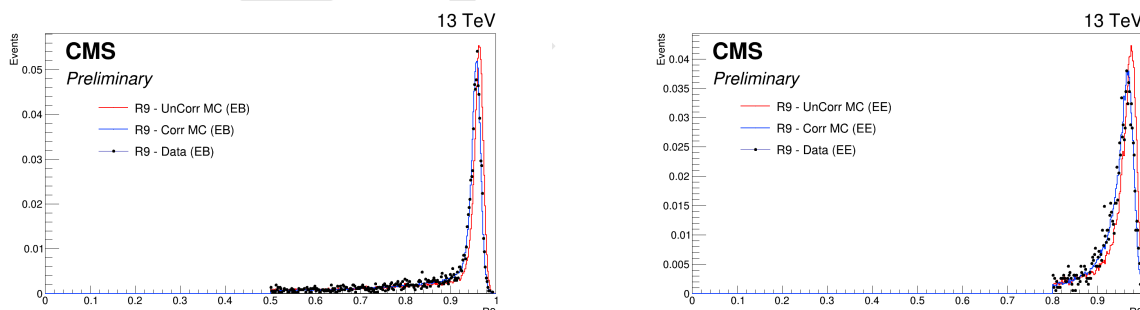


Figure 4.52: Data and MC of the R9 variable, before and after the reweighting. Barrel (left) and Endcap (right).

### 4.7.2 Event counting and yields

Tables 4.4 and 4.5 show the total number of events before and after the full selection. Two things are important to notice.

The signal selection efficiency is between 20% and 21% for all  $\Upsilon$  states and categories.

<sup>6</sup>EB stands for Electromagnetic Barrel

	Data	Signal			$Z \rightarrow \mu\mu\gamma_{FSR}$
		$Z \rightarrow \Upsilon(1S) + \gamma$	$Z \rightarrow \Upsilon(2S) + \gamma$	$Z \rightarrow \Upsilon(3S) + \gamma$	
Total (before selection)	169.84 M	3.54	1.4	1.22	$3.33 \times 10^3$
Inclusive	447	0.393	0.157	0.136	176
EB High R9	197	0.172	0.0682	0.0597	78
EB Low R9	146	0.129	0.0519	0.0448	58.5
EE	104	0.0916	0.0365	0.032	39.8

Table 4.4: Number of events for the Z decay, before and after the full selection, per categorization scenarios.

	Data	Signal			$H \rightarrow \gamma\gamma^*$
		$H \rightarrow \Upsilon(1S) + \gamma$	$H \rightarrow \Upsilon(2S) + \gamma$	$H \rightarrow \Upsilon(3S) + \gamma$	
Total (before selection)	169.84 M	0.000257	$5.43 \times 10^{-5}$	$3.93 \times 10^{-5}$	136
Inclusive	231	$5.23 \times 10^{-5}$	$1.2 \times 10^{-5}$	$8.96 \times 10^{-6}$	1.22

Table 4.5: Number of events for the H decay, before and after the full selection.

When one compares the fraction of selected peaking background, with respect to the selected data events for the Higgs decay ( $1.22/231$ ), the fraction obtained ( $\sim 0.3\%$ ) is irrelevant. On the other hand, the same fraction for the Z decay ( $176/447$ ) is far from irrelevant ( $\sim 39\%$ )<sup>7</sup>. The same relation is not found in the  $H/Z \rightarrow J/\psi + \gamma$  analysis [23], where both decays (Higgs and Z) show neglectable estimations of peaking background contribution to data. The very same behavior was found by ATLAS [20]. It can be explained by the relatively larger cross-section of the Z peaking background ( $Z \rightarrow \mu\mu\gamma_{FSR}$ ), with respect to the Higgs peaking background (Higgs Dalitz Decay). For the  $J/\psi$  channel, it is not an issue since its cross-section is way larger than the peaking background. The figures 4.16 and 4.29 help to clarify these affirmations, for the Z and Higgs decay, respectively. One can easily see how clear the  $J/\psi$  peak is in both decays and how minor the Higgs Dalitz Decay contributions is to the  $\Upsilon$  peak, with respect to the  $Z \rightarrow \mu\mu\gamma_{FSR}$  contribution. It is important to keep in mind the different scaling of the peaking background distributions,  $\times 3$  for the Z and  $\times 100$  for the Higgs. The peaking background to the data due to  $Z \rightarrow \Upsilon(1S, 2S, 3S) + \gamma$  channel is the main motivation to use a 2-dimensional modeling fitting of the signal and background events, in order to add one more layer of differentiation between many backgrounds contributions which will be detailed in the next section.

<sup>7</sup>It is worth to keep in mind that this is a estimation based on MC

## 4.8 Background modeling

The background modeling proposed for this analysis is a two dimensional unbinned maximum likelihood fit on the  $\mu\mu$  and the  $\mu\mu\gamma$  invariant mass distributions. It is considered and modeled, as briefly discussed in 4.1.2, three kinds of backgrounds:

- **Full Combinatorial:** any combination of two muon and one photon that pass all the object reconstruction and event selection criteria.
- **$\Upsilon$  Combinatorial:** a  $\Upsilon(1S, 2S, 3S)$ , that decays to a dimuon system, combined with a misidentified photon (misreconstructed, Pile-up photon, etc.), that pass all the object reconstruction, identification and event selection criteria.
- **Peaking background:** a Z (or Higgs) that decays straight to a  $\mu\mu\gamma$ , that pass all the object reconstruction and event selection criteria, without passing through any intermediate state. The main contributions considered for this background are  $Z \rightarrow \mu\mu\gamma_{FSR}$  (a Z decaying to a dimuon system with one of the muons irradiating a photon) or a Higgs Dalitz Decay.

All of them will be modeled from data, with some inputs from the MC (simulated) samples, as explained below. For both invariant mass spectra ( $\mu\mu$  and  $\mu\mu\gamma$ ) the full combinatorial background is expected to behave like a non-peaking distribution. The same behavior is expected for the  $\mu\mu\gamma$  mass distribution of the  $\Upsilon$  Combinatorial background and for the  $\mu\mu$  mass distribution of the peaking background.

On the other hand, the  $\mu\mu$  distribution of the  $\Upsilon$  Combinatorial background and the  $\mu\mu\gamma$  mass distribution for the peaking background are expected to behave like a peaking distribution, centered around the  $\Upsilon(1S, 2S, 3S)$  invariant mass (9.46 GeV, 10.02 GeV and 10.35 GeV) [2] and the Z boson invariant mass (91.2 GeV) [2], respectively . Table 4.6 summarizes the background modeling proposed for this analysis.

	$m_{\mu\mu}$	$m_{\mu\mu\gamma}$
<b>Peaking background</b>	Bernstein 1 <sup>st</sup> order	Crystal Ball (Higgs decay) Double Crystal Ball (Z decay)
<b><math>\Upsilon</math> Combinatorial</b>	3 Gaussians (one for each $\Upsilon$ state)	
<b>Full Combinatorial</b>	Chebychev 1 <sup>st</sup> order	Polynomial

Table 4.6: Modeling for each background source and mass component.

For the  $Z \rightarrow \Upsilon(1S, 2S, 3S) + \gamma$  analysis, the peaking background model parameters are extracted by performing a simultaneous 2-dimensional fit over the invariant masses,  $m_{\mu\mu}$  and  $m_{\mu\mu\gamma}$ , of the simulated  $Z \rightarrow \mu\mu\gamma_{FSR}$  MC sample of events that passes the selection described in Section 4.4, as in figure 4.53. Once the parameters are extracted, they are fixed and the *pdf* (Probability Distributions Function) of the 2-Dimensional modeling is stored, leaving only the normalization of the *pdf* as a parameter free to float (this will be determined from data).

In order to describe the 2-dimensional invariant mass distribution of the Peaking Background, as stated in Table 4.6, the  $m_{\mu\mu}$  component is described by a Bernstein polynomial of 1<sup>st</sup> order [55], which is used here just a representation of a linear function. The  $m_{\mu\mu\gamma}$  component is described by Double Crystal Ball function [56]. A Crystal Ball function is a *pdf* composed by a gaussian distribution and a power-law tail to the left, before certain threshold. The Crystal Ball function was named after the Crystal Ball Collaboration (first to use this *pdf*) and it is widely used in high-energy physics to describe mass distributions that incorporate FSR (final state radiation) effects, via the power-law tail. A Double Crystal Ball is a Crystal Ball function with the power-law tail on both sides.

939 A Crystal Ball function is define as:

$$CB(x; \alpha, n, \bar{x}, \sigma) = N \cdot \begin{cases} \exp\left(-\frac{(x-\bar{x})^2}{2\sigma^2}\right), & \text{for } \frac{x-\bar{x}}{\sigma} > -\alpha \\ A \cdot (B - \frac{x-\bar{x}}{\sigma})^{-n}, & \text{for } \frac{x-\bar{x}}{\sigma} \leq -\alpha \end{cases}, \quad (4.4)$$

940 where,

$$941 A = \left(\frac{n}{|\alpha|}\right)^n \cdot \exp\left(-\frac{|\alpha|^2}{2}\right),$$

$$942 B = \frac{n}{|\alpha|} - |\alpha|,$$

$$943 N = \frac{1}{\sigma(C+D)},$$

$$944 C = \frac{n}{|\alpha|} \cdot \frac{1}{n-1} \cdot \exp\left(-\frac{|\alpha|^2}{2}\right),$$

$$945 D = \sqrt{\frac{\pi}{2}} \left(1 + \operatorname{erf}\left(\frac{|\alpha|}{\sqrt{2}}\right)\right),$$

946 and  $\operatorname{erf}$  is the error function.

947 For the three gaussian functions fits, which represent the three  $\Upsilon$  states (1S, 2S and 3S) from the  $\Upsilon$   
 948 Combinatorial background in the  $m_{\mu\mu}$  component, we use a  $\Upsilon$  control sample in order to extract the  
 949 fit parameters, including the relative normalization between each  $\Upsilon$  state. This sample is composed  
 950 by dimuon candidates obtained from data, by selecting the events that passes the same trigger and  
 951 dimuon selection of the nominal selection and with  $p_T^{\mu\mu} > 35$  GeV (this cut is done in order to  
 952 keep this selected dimuon candidates compatibles with the  $p_T^{\mu\mu}/M_{\mu\mu\gamma}$  cut applied in the nominal  
 953 selection). No selection or cuts in the photon are required.

954 This control sample is fitted with a Chebychev 1<sup>st</sup> order (linear polynomial) for the background  
 955 support and 3 gaussian with the following constraints:

- 956 • the mean of each state should be the ones in the PDG [2], but allowed to shift by a float and  
 957 common (the same for all states) value.
- 958 • the sigma should be based on the 1S fit of the MC. All other sigma should be the result of  
 959 the 1S sigma times the state mass over the 1S mass ( $\sigma_{2S,3S} = \frac{m_{2S,3S}}{m_{1S}} \sigma_{1S}$ ).

960 The idea behind this fit is that scale and resolution (mean and sigma, respectively, of the gaussians)  
 961 over a sample without a photon selection should be the same as over a sample with photon selection,  
 962 since these are detector only dependent effects. The fact that we exclude the photon from this control  
 963 sample, improves the statistics and gives a better measurement of these variables.

964 The fit of the  $\Upsilon$  control sample if shown in figure 4.54.

965 Once determined, the fit parameters are fixed, they are used to compose the 2-Dimensional *pdf*. The  
 966  $m_{\mu\mu}$  component of the full combinatorial background is derived fully from the data fit (described  
 967 below). In the same sense, the  $m_{\mu\mu\gamma}$  component of the full combinatorial and the  $\Upsilon(nS)$  Combi-  
 968 torial backgrounds are also fully derived from the data, but following a more complex procedure:  
 969 a composition with the *pdf* components described above, plus a statistical test, to avoid overfit-  
 970 ting within a Discrete Profiling (or "Envelope Method"), as described in [57] and also implemented  
 971 in [54].

972 The statistical test consists of, for each category, different orders of a set of polynomial *pdfs* families  
 973 are tested: a sums of exponentials, sum of polynomials (in the Bernstein basis), a Laurent series  
 974 and a sums of power-law functions.

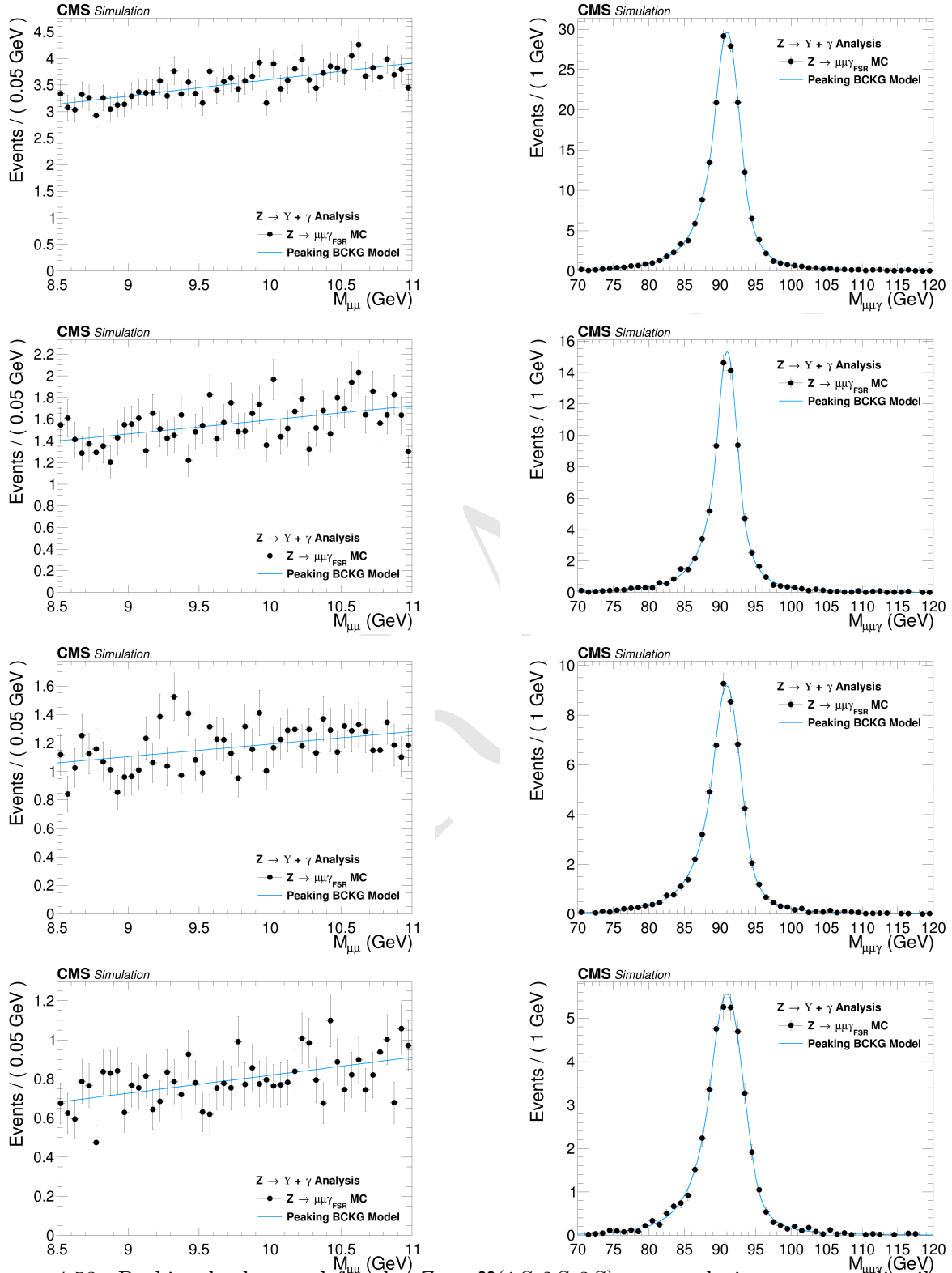


Figure 4.53: Peaking background for the  $Z \rightarrow Y(1S, 2S, 3S) + \gamma$  analysis.  $\mu\mu$  mass distribution (left) and  $\mu\mu\gamma$  invariant mass distribution (right). From top to bottom categories: Inclusive, EB High R9, EB Low R9, EE.

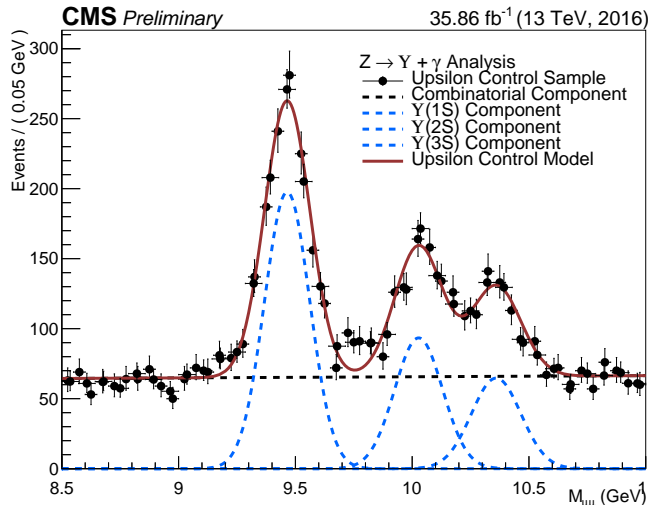


Figure 4.54:  $\Upsilon$  control sample fit with Chebychev 1<sup>st</sup> order for the background support and 3 gaussian for the three  $\Upsilon(1S, 2S, 3S)$  peaks.

- Sums of exponentials:

$$f_N(x) = \sum_{i=1}^N p_{2i} e^{p_{2i+1}x},$$

- Sums of polynomials (in the Bernstein basis):

$$f_N(x) = \sum_{i=0}^N p_i b_{(i,N)}, \text{ where } b_{(i,N)} := \binom{N}{i} x^i (1-x)^{N-i},$$

- Laurent series:

$$f_N(x) = \sum_{i=1}^N p_i x^{-4+\sum_{j=1}^i (-1)^j(j-1)},$$

- Sums of power-law functions:

$$f_N(x) = \sum_{i=1}^N p_{2i} x^{-p_{2i+1}},$$

where for all  $k$ , the  $p_k$  are a set of floating parameters in the fit.

Twice difference in the negative log-likelihood ( $NLL$ ) between the  $N^{th}$  and the  $(N+1)^{th}$  order of the same polynomial ( $\Delta NLL = 2 \times (NLL_N - NLL_{N+1})$ ) is expected to follow a  $\chi^2$  distribution with  $M$  degrees of freedom, where  $M$  is the increase in degrees of freedom when going from  $N^{th}$  to  $(N+1)^{th}$ . This can be shown with the help of the Wilks' theorem [58].

Starting from the lowest order possible, the best choice of order, for each family, is determined when a increase in the order of the polynomial, does not brings a significant improvement in the quality of the fit. Since a model with more fit parameters (higher order polynomials) will always perform, if not the same, better than a simpler one, an optimal choice of the polynomial order, will be the one right before the model becomes too flexible for the data.

985 Consider a  $p$ -value defined as:

$$\begin{aligned} p\text{-value} &= \int_{\Delta NLL}^{\infty} \chi_M^2(\Delta) d\Delta \\ &= P(\chi_M^2 > \Delta NLL), \end{aligned} \quad (4.5)$$

986 In the same spirit as the Wilks' theorem, this is the  $p$ -value for a likelihood ratio test between a  
 987 null hypotheses and an alternative model, where the null hypotheses is the  $N^{th}$  order and  $(N+1)^{th}$   
 988 order is the alternative one.

$$\begin{aligned} \Delta NLL &= 2 \times (NLL_N - NLL_{N+1}) \\ &= -2 \times \log\left(\frac{\mathcal{L}_N}{\mathcal{L}_{N+1}}\right), \end{aligned} \quad (4.6)$$

989 where  $\mathcal{L}_N$  is the likelihood for the  $N^{th}$  polynomial order.

990 The alternative will present a statistically significant improvement, with respect to the null hypothe-  
 991 seses, if the  $p$ -value is smaller than 0.05, since the probability of obtaining, by chance, considering  
 992 the null hypotheses is true, a even higher  $\Delta NLL$  is less than 5%. This will give support to chose  
 993  $(N+1)^{th}$  over  $N^{th}$ .

994 If the  $p$ -value is greater than 0.05 a higher order is not supported, since the probability of obtaining  
 995 a  $\Delta NLL$  greater than the one observed is statistically significant (more than 5%). A higher  $\Delta NLL$   
 996 means that another data sample, collected and analyzed with strictly the same conditions, would  
 997 have a probability of more than 5% of giving a better fit improvement than the one observed,  
 998 again assuming that the null hypotheses is true. This is an indication of overfitting, since the  
 999 improvements are likely to come from just statistical fluctuations. When testing the  $(N+1)^{th}$  order  
 1000 and this condition is reached, the optimal order should be the  $N^{th}$ .

1001 At first, before any fit to data, the 2-Dimensional model is composed by the five components, as  
 1002 described in Table 4.6 (in which the  $m_{\mu\mu\gamma}$  modeling for the Full Combinatorial Background and the  
 1003  $\Upsilon$  combinatorial are shared), then, the statistical test described before is ran for each family. It is  
 1004 important to stress that before the statistical test all the other fitting parameters have been fixed.  
 1005 This leaves only the normalizations of the model components and the polynomial coefficients free  
 1006 to float.

1007 Once the optimal order for each  $pdf$  family is obtained, the composed  $pdf$  with each choice from  
 1008 statistical test is saved in the same model, providing a discrete variable that indexes the different  
 1009 polynomial  $pdf$  families. This method is called Discrete Profiling (or "*Envelope Method*") and it  
 1010 allows the analysis algorithm to treat the choice of the  $pdf$  as a systematics and incorporate its  
 1011 effect in the extracted upper limits. This model, with different choices of polynomial families is  
 1012 called envelope.

1013 The implementation, used in the analysis, of the statistical test and the Discrete Profiling is based  
 1014 on the same algorithm used by the  $H \rightarrow \gamma\gamma$  Run II analysis. An extensive documentation on these  
 1015 methods can be found in  $H \rightarrow \gamma\gamma$  analysis note and physics analysis summary [59, 60] and in the  
 1016 specific reference of the Discrete Profiling [57]. The figures 4.55 and 4.56 show the projection for  
 1017 the  $\mu\mu$  and  $\mu\mu\gamma$  distribution after the statistical test.

1018 For the  $H \rightarrow \Upsilon(1S, 2S, 3S) + \gamma$  analysis, the same procedure is implemented, except for the peaking  
 1019 background modeling. Since the MC prediction for the contribution of the background is too small,

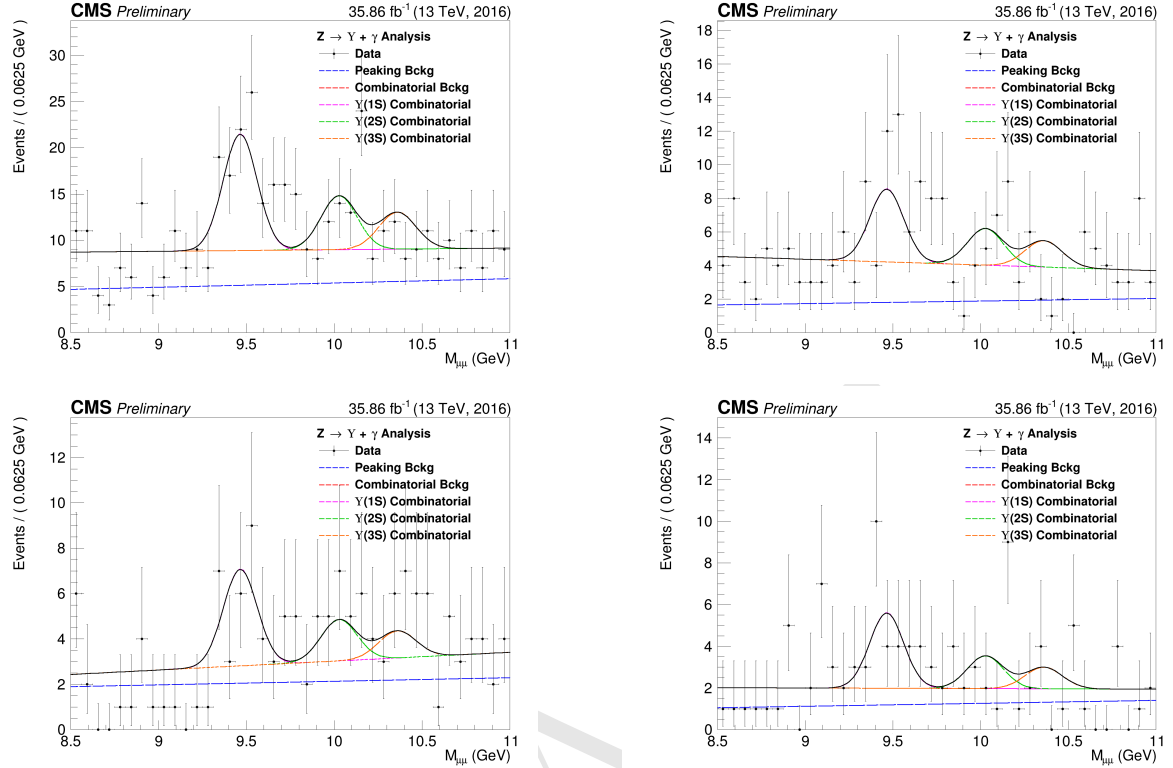


Figure 4.55:  $Z \rightarrow \Upsilon(1S, 2S, 3S) + \gamma$  Background Modeling:  $\mu\mu$  distribution. Inclusive (top left); EB High R9 (top right), EB Low R9 (bottom left), EE (bottom right). The pdfs projections are plotted with respect to the overall best choice of the statistica test.

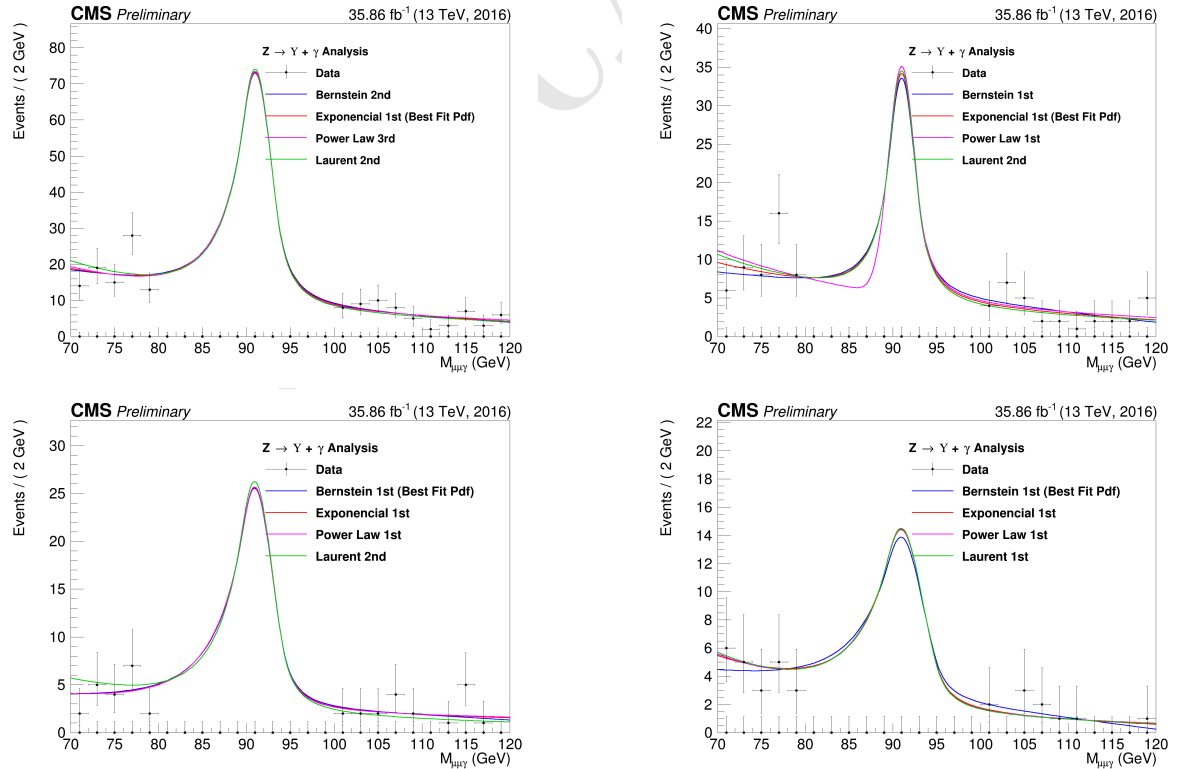


Figure 4.56:  $Z \rightarrow \Upsilon(1S, 2S, 3S) + \gamma$  Background Modeling:  $\mu\mu\gamma$  distribution. Inclusive (top left); EB High R9 (top right), EB Low R9 (bottom left), EE (bottom right). The plotted pdfs corresponds to the best choice by the statistical test for each family. The signal region, from 80 GeV to 100 GeV was blinded.

according to the comparison between the final selected events for data and the Higgs Dalitz Decay sample, in order to avoid fitting over statistical fluctuations of the data sample, the Peaking Background, for the Higgs channel, is fully modeled from the MC sample, including its normalization, as shown in figure 4.57, hence it is not included the the statistical test, neither in the final background modeling envelope.

The results of the background modeling for the Full Combinatorial and  $\Upsilon$  Combinatorial, can be found at Figures 4.58 and 4.59, for the  $\mu\mu$  and  $\mu\mu\gamma$  distribution, respectively. It is worth to remember that, for the Higgs channel, we are not implementing any categorization.

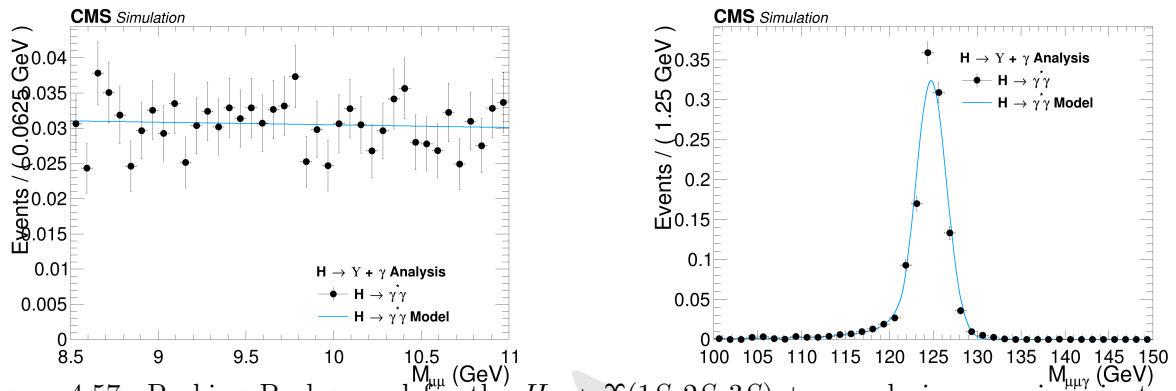


Figure 4.57: Peaking Background for the  $H \rightarrow \Upsilon(1S, 2S, 3S) + \gamma$  analysis.  $m_{\mu\mu}$  invariant mass distribution (left) and  $m_{\mu\mu\gamma}$  invariant mass distribution (right).

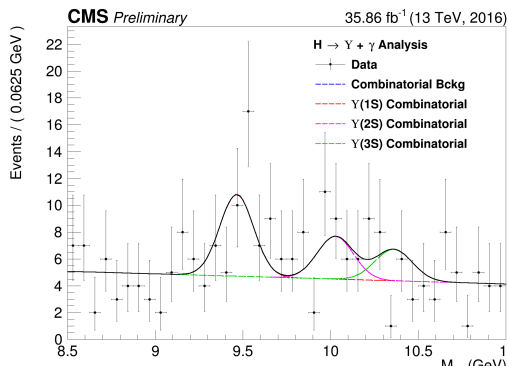


Figure 4.58:  $H \rightarrow \Upsilon(1S, 2S, 3S) + \gamma$  Background Modeling:  $m_{\mu\mu}$  distribution. The  $pdfs$  projections are plotted with respect to the overall best choice of the statistical test.

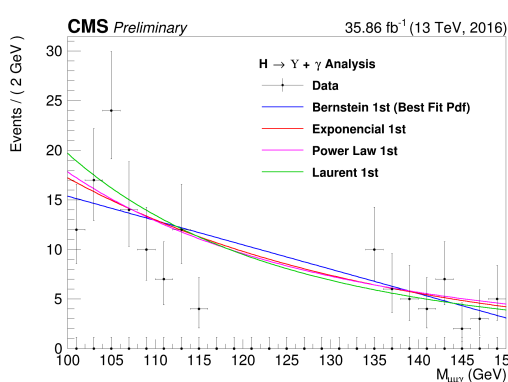


Figure 4.59:  $H \rightarrow \Upsilon(1S, 2S, 3S) + \gamma$  Background Modeling:  $\mu\mu\gamma$  distribution. The plotted  $pdfs$  corresponds to the best choice by the statistical test for each family. The signal region, from 115 GeV to 135 GeV was blinded.

<sub>1028</sub> **4.9 Signal modeling**

<sub>1029</sub> Along the same lines as the background modeling (Section 4.8), the signal modeling is implemented  
<sub>1030</sub> as a two dimensional unbinned maximum likelihood fit on the  $m_{\mu\mu}$  and the  $m_{\mu\mu\gamma}$  invariant masses  
<sub>1031</sub> distributions, but this time, only using the signal simulated MC samples 4.1.2. Since, for the two  
<sub>1032</sub> spectra, it is expected a peak-like distribution, one centered in the Z (or Higgs) boson mass and the  
<sub>1033</sub> other centered in the  $\Upsilon$  mass, two also peak-like analytics *pdfs* were chosen to compose the signal  
<sub>1034</sub> model. The modeling is summarized in table 4.7.

	$m_{\mu\mu}$	$m_{\mu\mu\gamma}$
$Z \rightarrow \Upsilon(1S, 2S, 3S) + \gamma$	Double Crystal Ball	Double Crystal Ball
$H \rightarrow \Upsilon(1S, 2S, 3S) + \gamma$	Double Crystal Ball	Crystal Ball + Gaussian with the same mean

Table 4.7: Modeling for each signal source and mass component.

<sub>1035</sub> The projections of the modeling for the Z boson decay channel analysis can be found at figures 4.60,  
<sub>1036</sub> 4.61, 4.62 and 4.63, for Inclusive, EB High R9, EB Low R9 and EE, respectively. The projection  
<sub>1037</sub> on the modeling for the Higgs boson signal can be found at Figure 4.64. A deeper discussion on the  
<sub>1038</sub> systematics uncertainties associated to them, will be presented in the next section.

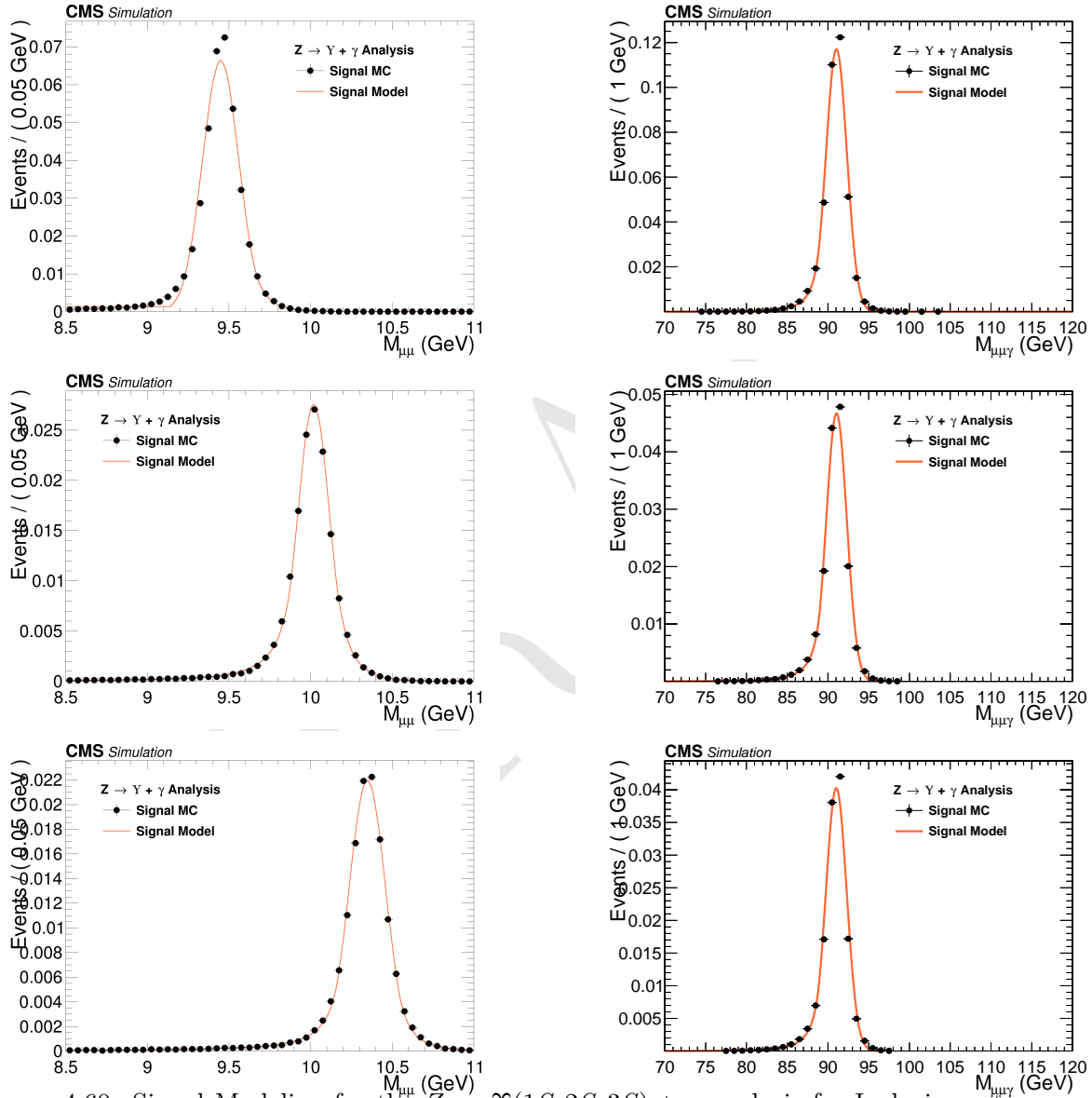


Figure 4.60: Signal Modeling for the  $Z \rightarrow \Upsilon(1S, 2S, 3S) + \gamma$  analysis for Inclusive category.  $m_{\mu\mu}$  mass distribution (left) and  $m_{\mu\mu\gamma}$  mass distribution (right). From top to bottom:  $\Upsilon(1S)$ ,  $\Upsilon(2S)$ ,  $\Upsilon(3S)$ .

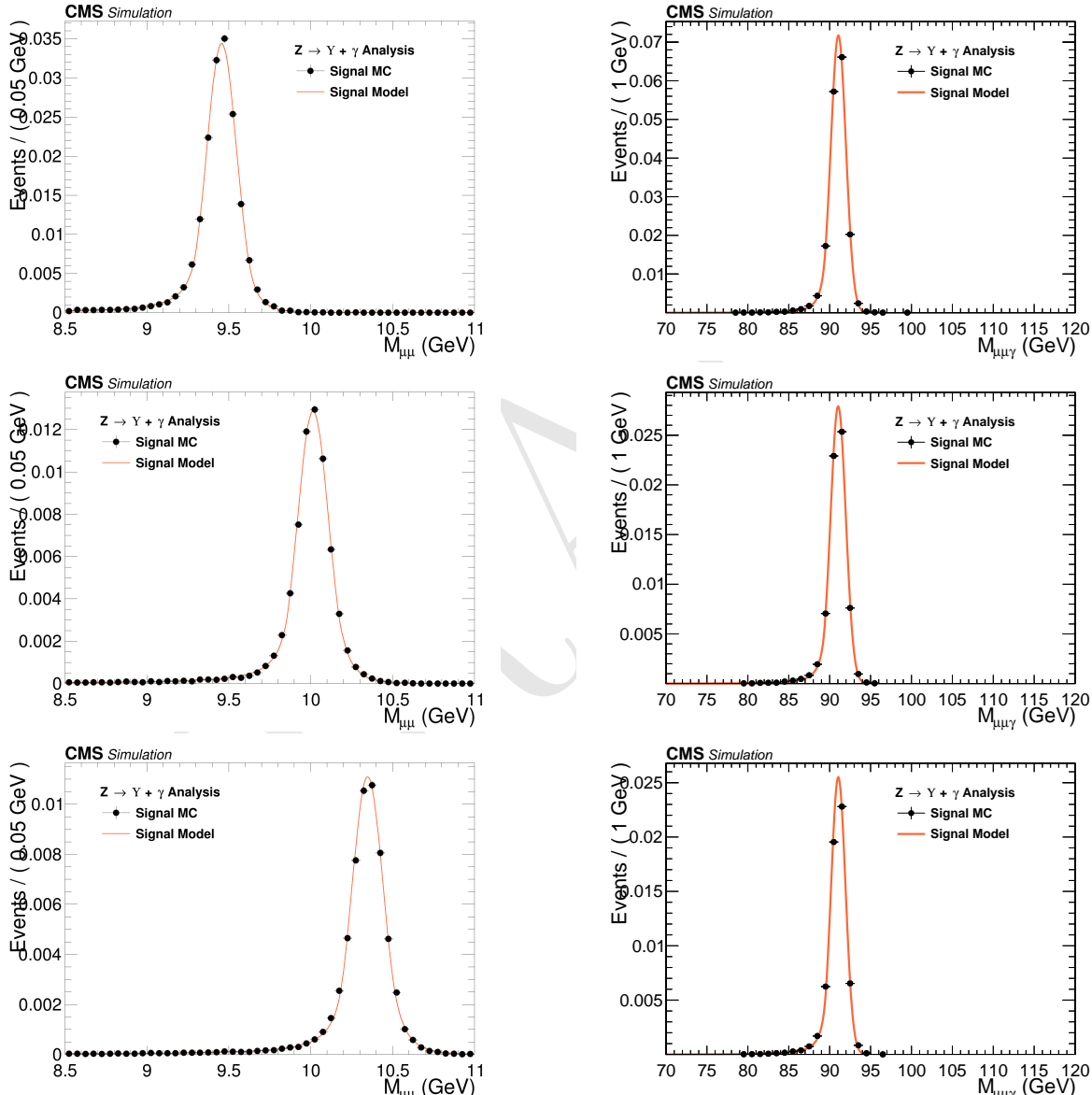


Figure 4.61: Signal Modeling for the  $Z \rightarrow \Upsilon(1S, 2S, 3S) + \gamma$  analysis for EB High R9 category.  $m_{\mu\mu}$  mass distribution (left) and  $m_{\mu\mu\gamma}$  mass distribution (right). From top to bottom:  $\Upsilon(1S)$ ,  $\Upsilon(2S)$ ,  $\Upsilon(3S)$ .

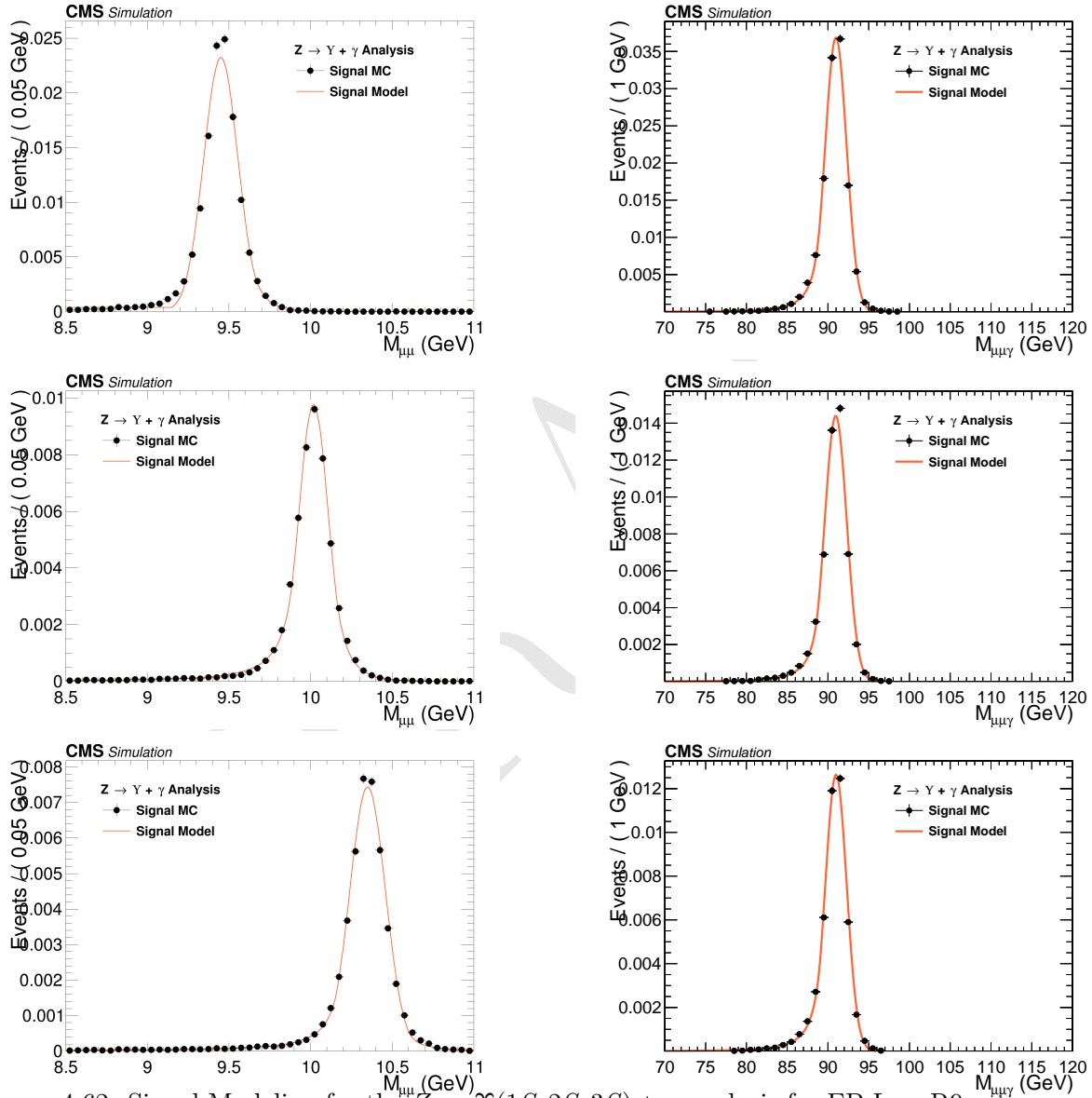


Figure 4.62: Signal Modeling for the  $Z \rightarrow \Upsilon(1S, 2S, 3S) + \gamma$  analysis for EB Low R9 category.  $m_{\mu\mu}$  mass distribution (left) and  $m_{\mu\mu\gamma}$  mass distribution (right). From top to bottom:  $\Upsilon(1S)$ ,  $\Upsilon(2S)$ ,  $\Upsilon(3S)$ .

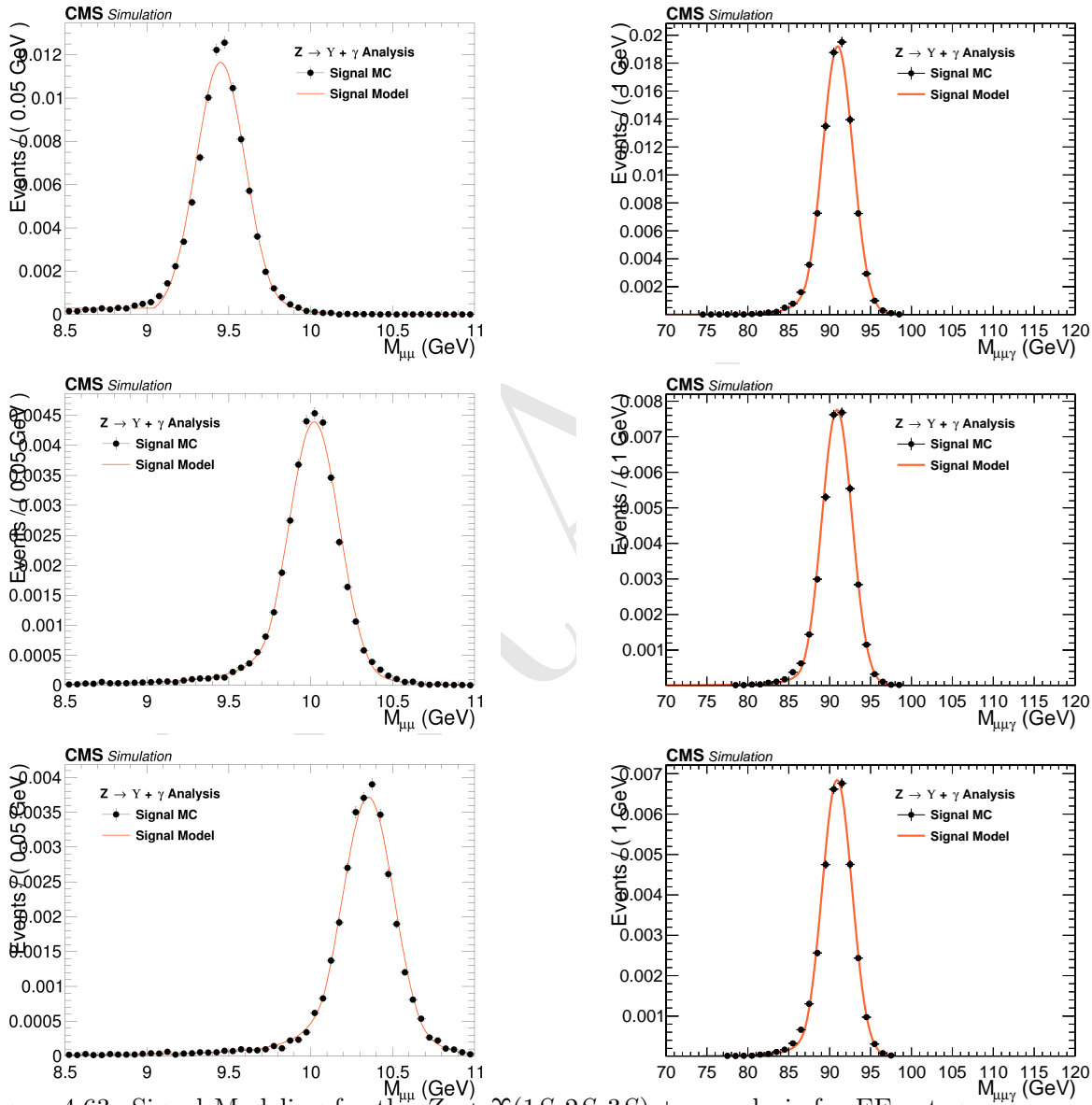


Figure 4.63: Signal Modeling for the  $Z \rightarrow \Upsilon(1S, 2S, 3S) + \gamma$  analysis for EE category.  $m_{\mu\mu}$  mass distribution (left) and  $m_{\mu\mu\gamma}$  mass distribution (right). From top to bottom:  $\Upsilon(1S)$ ,  $\Upsilon(2S)$ ,  $\Upsilon(3S)$ .

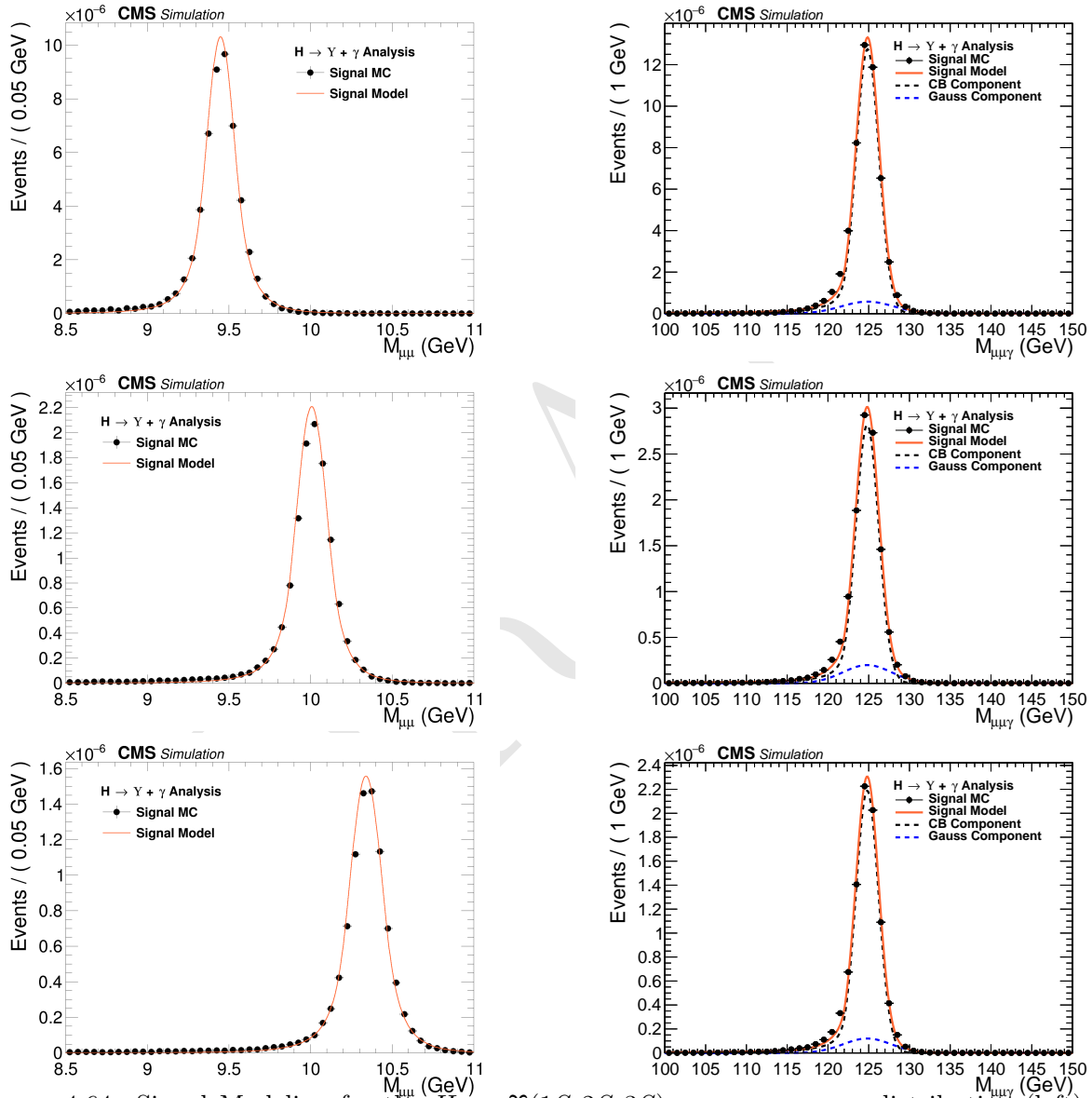


Figure 4.64: Signal Modeling for the  $H \rightarrow Y(1S, 2S, 3S) + \gamma$ .  $m_{\mu\mu}$  mass distribution (left) and  $m_{\mu\mu\gamma}$  mass distribution (right). From top to bottom:  $Y(1S)$ ,  $Y(2S)$ ,  $Y(3S)$ .

1039 **4.10 Systematic uncertainties**

- 1040 Two sources of systematics are considered: the ones that affect the predicted yields<sup>8</sup> and the ones  
1041 that affect the shape of the pdfs used to compose the signal and background model.
- 1042 Those that affect the predicted yields, presented in Section 4.7.2, it is considered integrated lumi-  
1043 nosity measurement [32], the pile-up description in the Monte-Carlo simulations, the corrections  
1044 applied to the simulated events in order to compensate for the differences in performance of the  
1045 some selection criteria, such as trigger, object reconstruction and identification, the  $\Upsilon$  polarization  
1046 and the theoretical uncertainties, such as the effects of the *parton density functions* (PDF) to the  
1047 signal cross section [41, 61, 62], the variations of the renormalization and factorization scales [63–  
1048 67], and the prediction of the decay branching ratios.
- 1049 For the systematics on the signal modeling, it is considered possible imprecisions of the momentum  
1050 scale and resolution. They are measured on how they affect the mean ( $\mu$ ) and the standard deviation  
1051 ( $\sigma$ ) of the signal model. For the background modeling, since it is derived from data, the choice of  
1052 the *pdf* (Probability distribution function) is the only systematic uncertainties considered. It is  
1053 treated by the Discrete Profiling method, as described in section 4.8.
- 1054 The two kinds of systematics uncertainties are described in details below.

1055 **4.10.1 Uncertainties on the predicted yields**

- 1056 The theoretical sources of uncertainties includes: parton distribution functions uncertainties, strong  
1057 coupling constant ( $\alpha_s$ ) uncertainty and uncertainty on the  $H \rightarrow \gamma\gamma$  branching fraction (used to derive  
1058 the Higgs Dalitz Decays cross-section). The values for these theoretical uncertainties are taken from  
1059 the Higgs Combination Group [44] and also from [66, 68].
- 1060 An uncertainty value of 2.5% is used on the integrated luminosity of the data samples, as recom-  
1061 mended by CMS [32]. To evaluate the impact of the pile-up reweighting in the final result, the  
1062 The total inelastic cross section of 69.2  $mb$  is varied by  $\pm 4.6\%$  and the analysis is ran with these  
1063 extreme values. The systematic uncertainty quoted is the maximum difference in the yields with  
1064 respect to nominal value, as recommended by CMS.
- 1065 The impact of the trigger scale factor is evaluated by running this analysis with  $\pm 1\sigma$  on the  
1066 Trigger Efficiency Scale factors (section 4.5.1). The systematic uncertainty quoted is the maximum  
1067 difference in the yields with respect to nominal value.
- 1068 For the final state object identification and isolation associated uncertainty, the scale factors, pro-  
1069 vided by CMS, to match the performance of MC and Data samples are varied in  $\pm 1\sigma$ . The  
1070 systematic uncertainty quoted is the maximum difference in the yields with respect to nominal  
1071 value. This procedure is applied on the scale factors for the Photon MVA ID and the Electron Veto  
1072 (section 4.5.3) and for Muon Identification and Isolation(section 4.5.2).
- 1073 Finally, the  $\Upsilon$  Polarization is assessed applying the extremes scenarios of the  $\Upsilon$  polarization (Trans-  
1074 verse and Longitudinal Polarization to the signal samples (section 4.2). The systematic uncertainty  
1075 quoted is the maximum difference in the yields with respect to nominal (Unpolarized) yield. This  
1076 procedure is applied only for the Z decay. For the Higgs decay, the only polarization considered is  
1077 the transverse polarization.
- 1078 The effect of all systematic uncertainties in the signal and peaking background yields are summarized  
1079 on table 4.8, for the Z decay and table 4.9, for the Higgs decay. Clearly, the main contribution to the

---

8Number of events, per process, after full selection and corrected by the expected SM cross sections.

1080 systematics uncertainties on the yields is Polarization of the  $\Upsilon(nS)$  (only for the Z decay), around  
 1081 15%.

#### 1082 4.10.2 Uncertainties that affect the signal fits

1083 Smearing and scaling corrections are applied on simulated events since the resolution of Monte  
 1084 Carlo is better than that on data and the detector might not catch all the possible differences in  
 1085 the detector performance, with respect to the data observation. They need to be estimated and  
 1086 included on the systematics. The corrections are:

- 1087 • **Muon Momentum Scale and Resolution:** extracted by running the analysis with different  
 1088 setups of the official CMS Muon scaling and smearing package [69]. The deviations, with  
 1089 respect to the default correction are summed in quadrature. Once the nominal parameters  
 1090 (mean or sigma) are obtained, the default corrections are shifted by  $\pm 1\sigma$  and the fits are  
 1091 re-done, with the parameters of interest free to float and all others fixed. The systematic  
 1092 uncertainty quoted is the maximum difference of the parameter with respect to nominal value.
- 1093 • **Photon Energy Scale and Resolution:** extracted by running the analysis with different  
 1094 sets of corrections, provided by the CMS <sup>9</sup>. Once the nominal mean is obtained, the sets  
 1095 are changed and the fits are re-done, with the mean free to float and all others parameters  
 1096 fixed. The corrections are shifted by  $\pm 1\sigma$  on each source of systematics (following standard  
 1097 CMS recommendations). The quoted as systematic uncertainty is the quadrature sum of the  
 1098 maximum deviation within each set.

1099 The effective systematic uncertainty associated with the scale and resolution are the quadrature  
 1100 sum of the muon and photon contributions. The effect of all systematic uncertainties in the Signal  
 1101 fits are summarized on table 4.10, for the Z and Higgs decay.

---

<sup>9</sup>CMS has not published, yet, a paper on the Run2 performance of the Photon reconstruction (This document is under internal review process.). Just as a reference, we cite the Run1 paper [70].

Source	Uncertainty			
	Signal		Peaking Background	
	$Z \rightarrow \Upsilon(1S)\gamma$	$Z \rightarrow \Upsilon(2S)\gamma$	$Z \rightarrow \Upsilon(3S)\gamma$	$Z \rightarrow \mu\mu\gamma_{FSR}$
Integrated luminosity				
All Categories	2.5%			
SM Z boson $\sigma$ (scale)				
All Categories	3.5%		5.0%	
SM Z boson $\sigma$ (PDF + $\alpha_s$ )				
All Categories	1.73%		5.0%	
Pileup Reweighting				
Inclusive	0.65%	0.68%	0.71%	0.62%
EB High R9	1.01%	1.1%	1.04%	1.06%
EB Low R9	0.17%	0.08%	0.13%	0.11%
EE 1.07%	0.98%	1.26%	0.78%	
Trigger				
Inclusive	4.45%	4.46%	4.49%	4.71%
EB High R9	3.5%	3.5%	3.52%	3.71%
EB Low R9	3.55%	3.54%	3.58%	3.72%
EE 7.52%	7.58%	7.56%	8.13%	
Muon Identification				
Inclusive	4.82%	4.81%	4.8%	4.52%
EB High R9	4.45%	4.45%	4.44%	4.2%
EB Low R9	4.65%	4.62%	4.63%	4.32%
EE 5.75%	5.75%	5.74%	5.44%	
Photon Identification				
Inclusive	1.1%	1.1%	1.09%	1.09%
EB High R9	1.1%	1.09%	1.09%	1.11%
EB Low R9	1.1%	1.1%	1.09%	1.08%
EE 1.1%	1.1%	1.1%	1.09%	
Electron Veto				
Inclusive	1.02%	1.02%	1.02%	1.03%
EB High R9	1.2%	1.2%	1.2%	1.2%
EB Low R9	1.2%	1.2%	1.2%	1.2%
EE 0.45%	0.45%	0.45%	0.45%	
Polarization				
Inclusive	15.36%	14.78%	14.84%	-
EB High R9	15.6%	14.88%	14.87%	-
EB Low R9	15.01%	14.31%	14.4%	-
EE 15.39%	15.27%	15.39%	-	

Table 4.8: A summary table of systematic uncertainties in the Z boson decaying in  $\Upsilon(1S, 2S, 3S) + \gamma$ , affecting the final yields of the MC samples.

Source	Uncertainty			
	Signal			Peaking Background
	$H \rightarrow \Upsilon(1S)\gamma$	$H \rightarrow \Upsilon(2S)\gamma$	$H \rightarrow \Upsilon(3S)\gamma$	$H \rightarrow \gamma\gamma^*$
Integrated luminosity	2.5%			
SM Higgs $\sigma$ (scale)	$+4.6\% / -6.7\%$			
SM Higgs $\sigma$ (PDF + $\alpha_s$ )	3.2%			
SM BR $H \rightarrow \gamma\gamma^*$	-			6.0%
Pileup Reweighting	0.61%	0.68%	0.56%	0.9%
Trigger	5.61%	5.47%	5.5%	6.12%
Muon Identification	4.39%	4.36%	4.34%	4.33%
Photon Identification	1.21%	1.22%	1.22%	1.2%
Electron Veto	1.04%	1.04%	1.04%	1.04%

Table 4.9: A summary table of systematic uncertainties in the Higgs boson decaying in  $\Upsilon(1S, 2S, 3S) + \gamma$ , affecting the final yields of the MC samples.

		Z $\rightarrow \Upsilon(nS) + \gamma$			H $\rightarrow \Upsilon(nS) + \gamma$
		Inclusive	EB High R9	EB Low R9	EE
$\Upsilon(1S)$	Mean - Scale				
	Muon Unc.	0.06%	0.05%	0.06%	0.11%
	Photon Unc.	0.21%	0.13%	0.19%	0.26%
	<b>Total Unc.</b>	0.22%	0.14%	0.2%	0.28%
	Sigma - Resolution				
	Muon Unc.	1.12%	0.84%	1.55%	1.14%
	Photon Unc.	2.14%	2.48%	1.95%	2.79%
	<b>Total Unc.</b>	2.42%	2.61%	2.49%	3.01%
	Mean - Scale				
$\Upsilon(2S)$	Muon Unc.	0.07%	0.05%	0.06%	0.13%
	Photon Unc.	0.25%	0.11%	0.2%	0.19%
	<b>Total Unc.</b>	0.26%	0.12%	0.21%	0.23%
	Sigma - Resolution				
	Muon Unc.	1.21%	1.54%	2.65%	1.66%
	Photon Unc.	1.85%	2.67%	3.56%	3.6%
	<b>Total Unc.</b>	2.21%	3.08%	4.44%	3.97%
	Mean - Scale				
	Muon Unc.	0.06%	0.06%	0.06%	0.09%
$\Upsilon(3S)$	Photon Unc.	0.22%	0.14%	0.25%	0.17%
	<b>Total Unc.</b>	0.23%	0.15%	0.26%	0.19%
	Sigma - Resolution				
	Muon Unc.	1.78%	2.38%	2.1%	2.25%
	Photon Unc.	2.51%	4.14%	2.23%	4.08%
	<b>Total Unc.</b>	3.08%	4.77%	3.07%	4.66%
	Mean - Scale				
	Muon Unc.	0.06%	0.06%	0.06%	0.09%
	Photon Unc.	0.22%	0.14%	0.25%	0.23%

Table 4.10: A summary table of systematic uncertainties in the Z (H) decaying in  $\Upsilon(1S, 2S, 3S) + \gamma$ , affecting the signal fits.

## 4.11 Modeling Cross checks

In order to test the applicability of the statistical (signal and background) modeling proposed in this study, a cross-check procedure is performed by generating a set of pseudo-experiments (toys datasets) based on the signal plus background model, for each decay channel ( $H/Z \rightarrow \Upsilon(1S, 2S, 3S, ) + \gamma$ ) with some signal injected.

The procedure consists of resample from the signal plus background a number of events, including some extra (injected signal). The amount of injected signal is controlled by the  $\mu_{true}$  variable, where  $\mu_{true} = X$  means inject  $X$  times the expected signal.

Once generated, the toy dataset is refitted to the signal plus background model and the signal strength ( $\mu_{fit}$ ) and its error  $\sigma_{fit}$  are extracted. This procedure is repeated 10000 times and only for the inclusive category. Figures 4.66, 4.65, 4.68 and 4.67 show examples of those fits for the Higgs and Z decay.

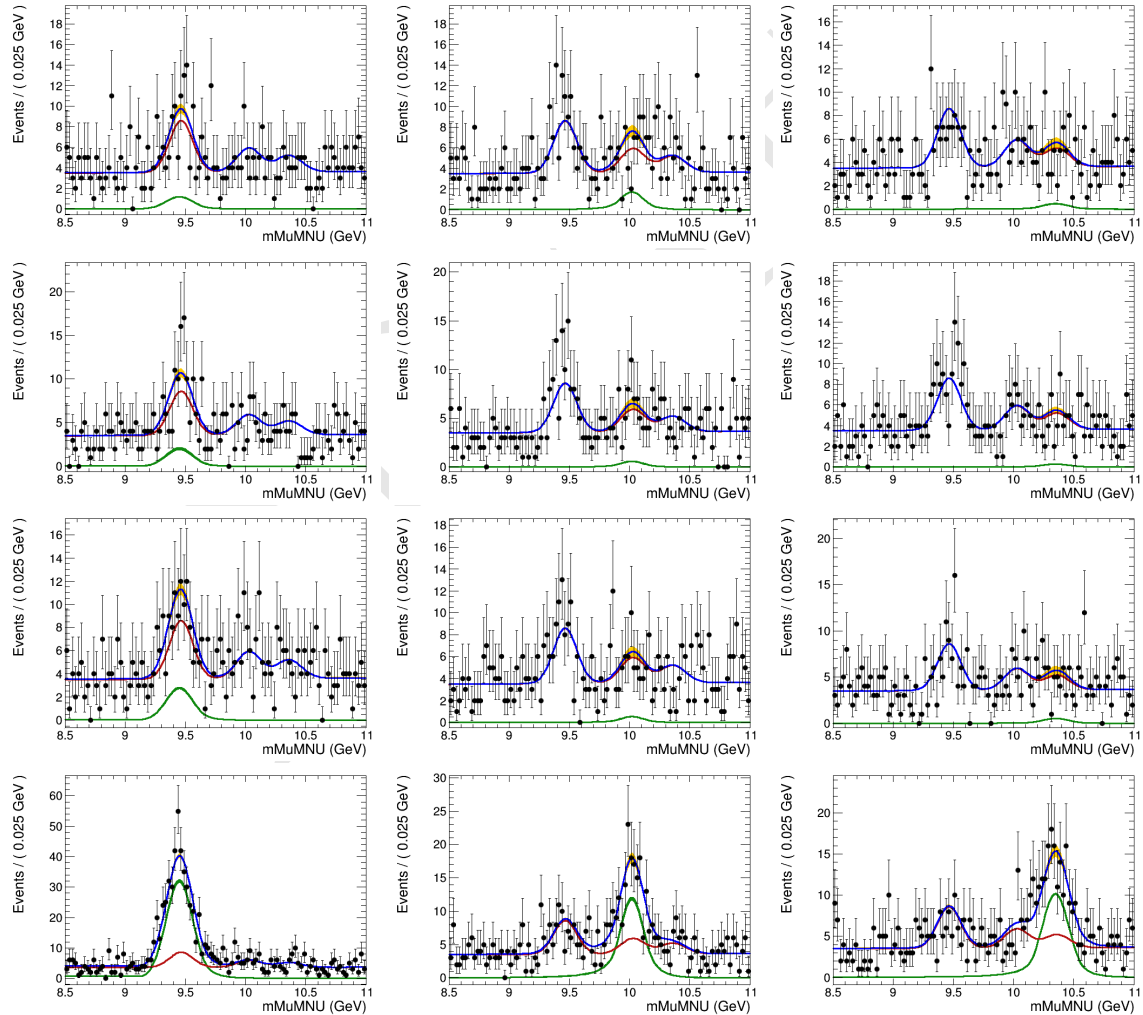


Figure 4.65: Examples of the toy datasets fit ( $M_{\mu\mu}$ ), for the Z decay analysis, after the toy dataset refit, for 1S, 2S and 3S (left to right), with  $\mu_{true}$  equals to 20, 50, 100, 1000 (top to bottom). The red lines corresponds to the background model (B), the green lines to signal model (S), the blue lines to the total (S+B) and the dots is the toy dataset.

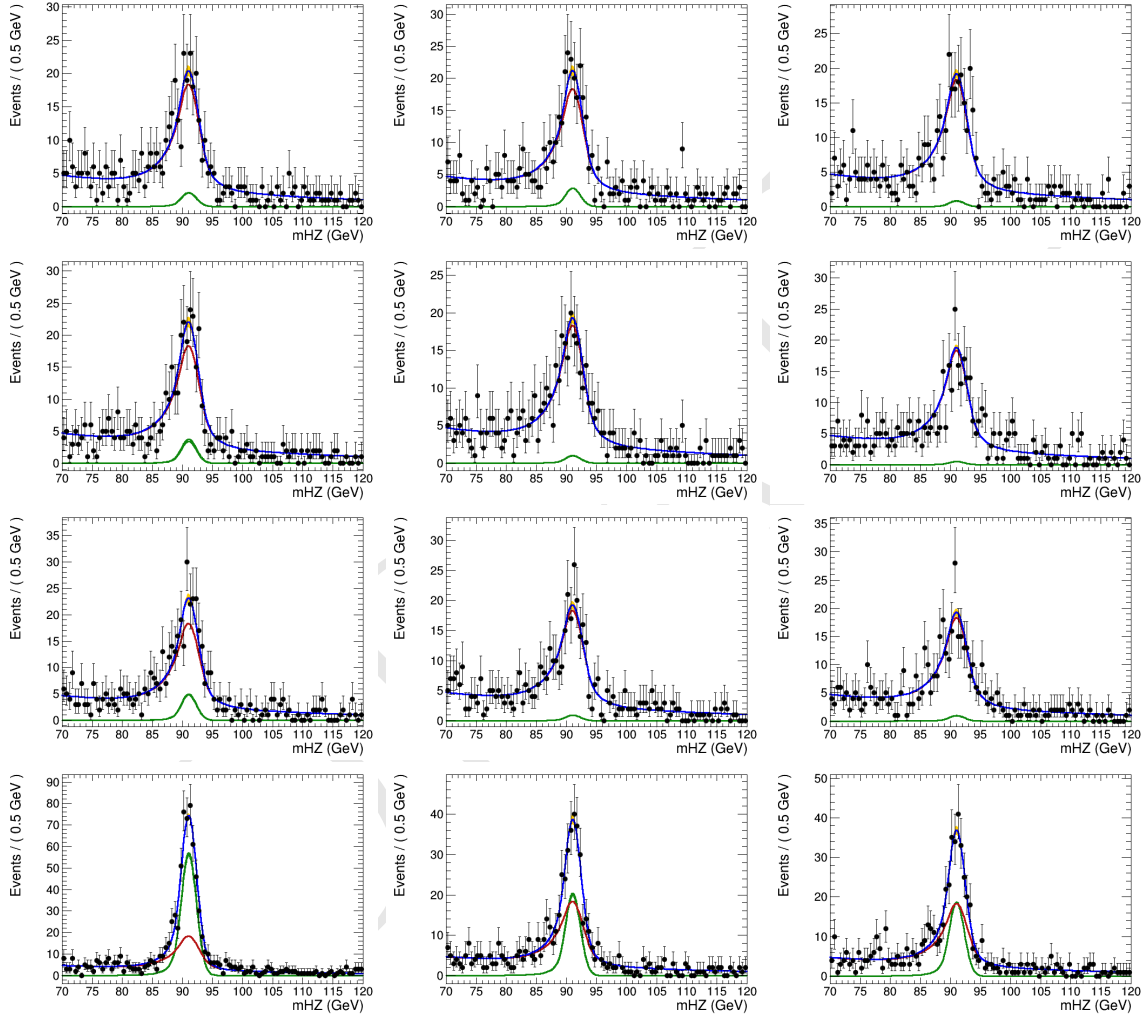


Figure 4.66: Examples of the toy datasets fit ( $M_{\mu\mu\gamma}$ ), for the Z decay analysis, after the toy dataset refit, for 1S, 2S and 3S (left to right), with  $\mu_{true}$  equals to 20, 50, 100, 1000 (top to bottom). The red lines corresponds to the background model (B), the green lines to signal model (S), the blue lines to the total (S+B) and the dots is the toy dataset.

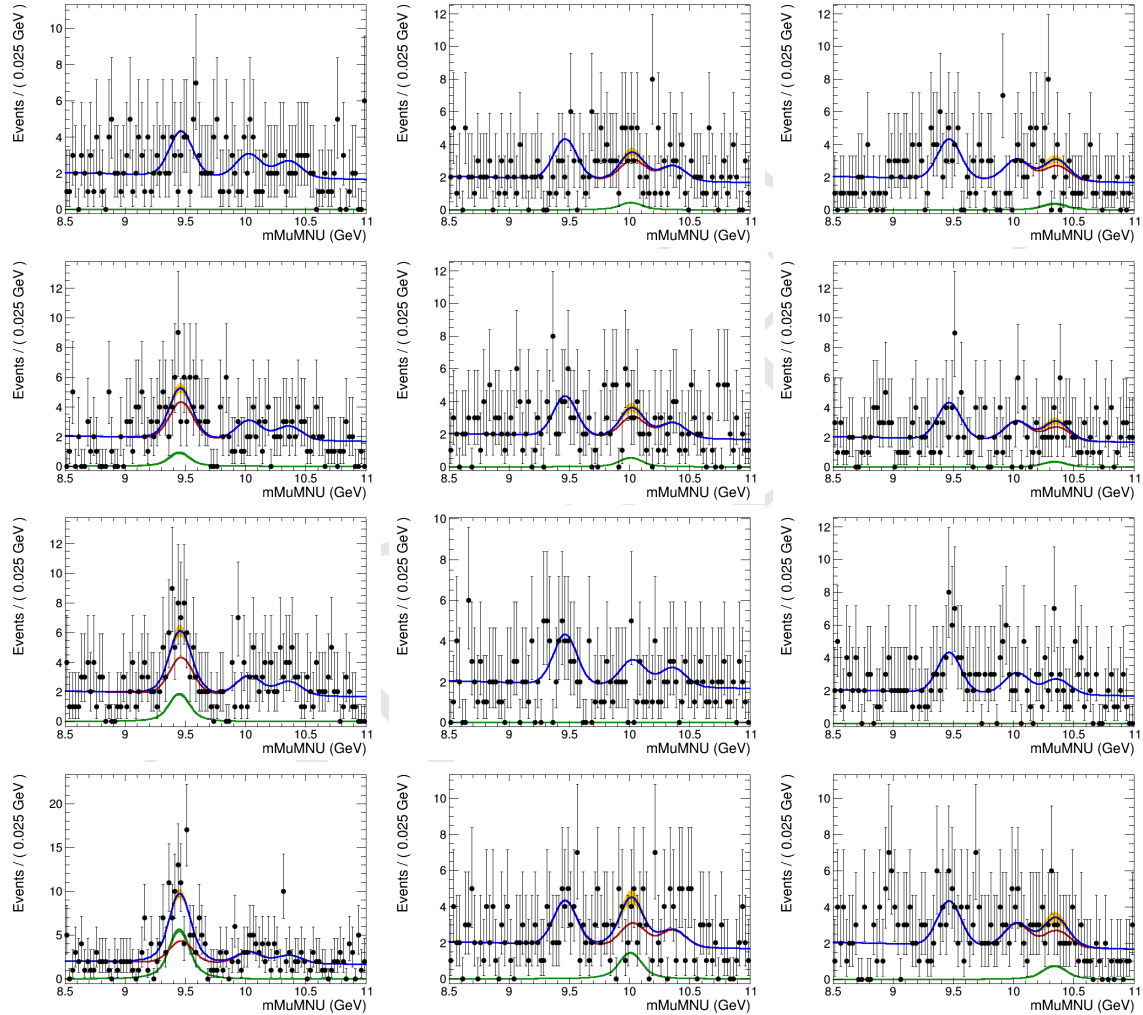


Figure 4.67: Examples of the toy datasets fit ( $M_{\mu\mu}$ ), for the Higgs decay analysis, after the toy dataset refit, for 1S, 2S and 3S (left to right), with  $\mu_{true}$  equals to 100000, 200000, 300000, 1000000 (top to bottom). The red lines corresponds to the background model (B), the green lines to signal model (S), the blue lines to the total (S+B) and the dots is the toy dataset.

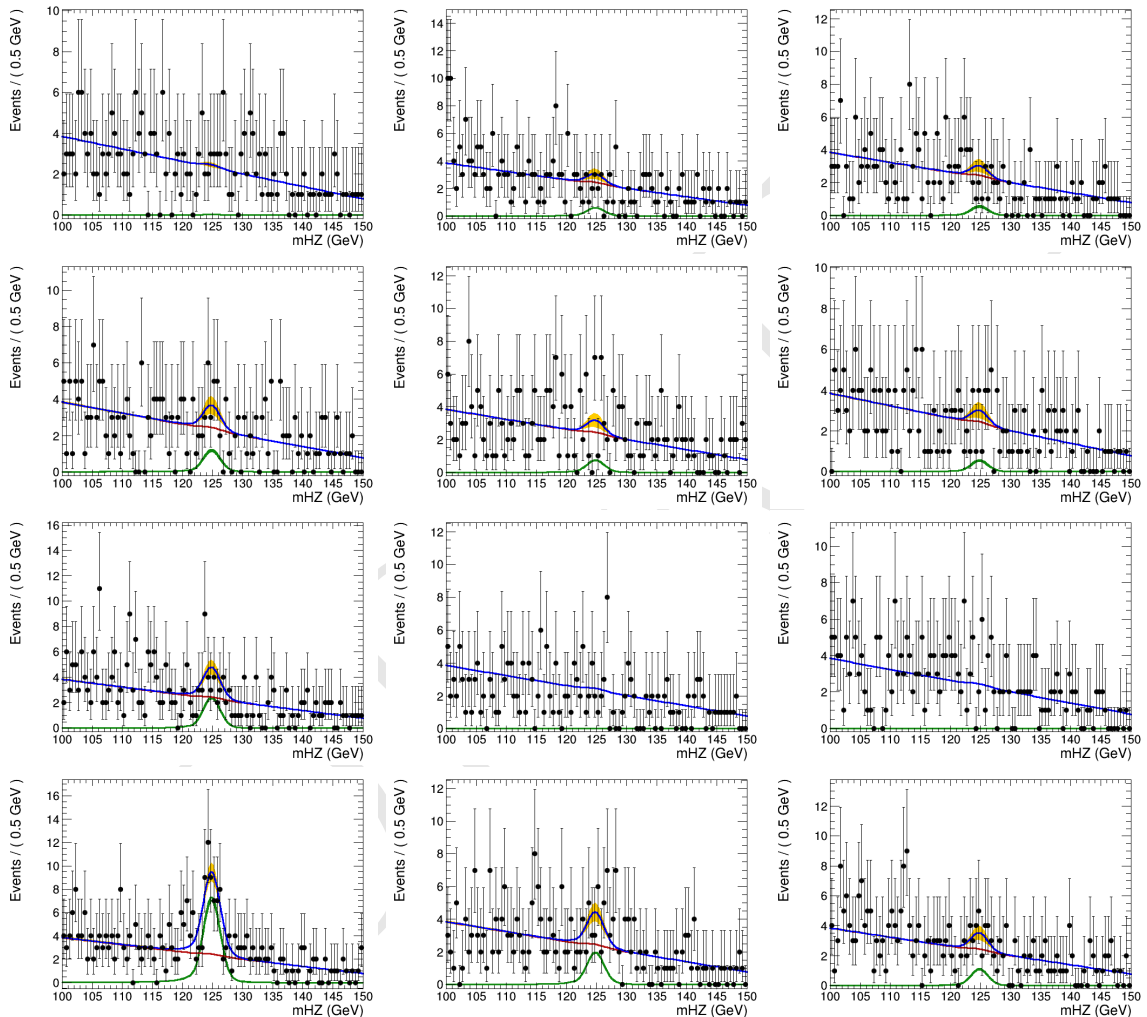


Figure 4.68: Examples of the toy datasets fit ( $M_{\mu\mu\gamma}$ ), for the Higgs decay analysis, after the toy dataset refit, for 1S, 2S and 3S (left to right), with  $\mu_{true}$  equals to 100000, 200000, 300000, 1000000 (top to bottom). The red lines corresponds to the background model (B), the green lines to signal model (S), the blue lines to the total (S+B) and the dots is the toy dataset.

1114 It is expected that the pulls distribution for the fitted signal strength ( $\frac{\mu_{fit} - \mu_{true}}{\sigma_{fit}}$ ) should follow a  
 1115 Gaussian distribution centered in 0 and with  $\sigma$  around 1. Figures 4.69 and 4.70 present those pulls  
 1116 distributions for the Z and Higgs decays, respectively.

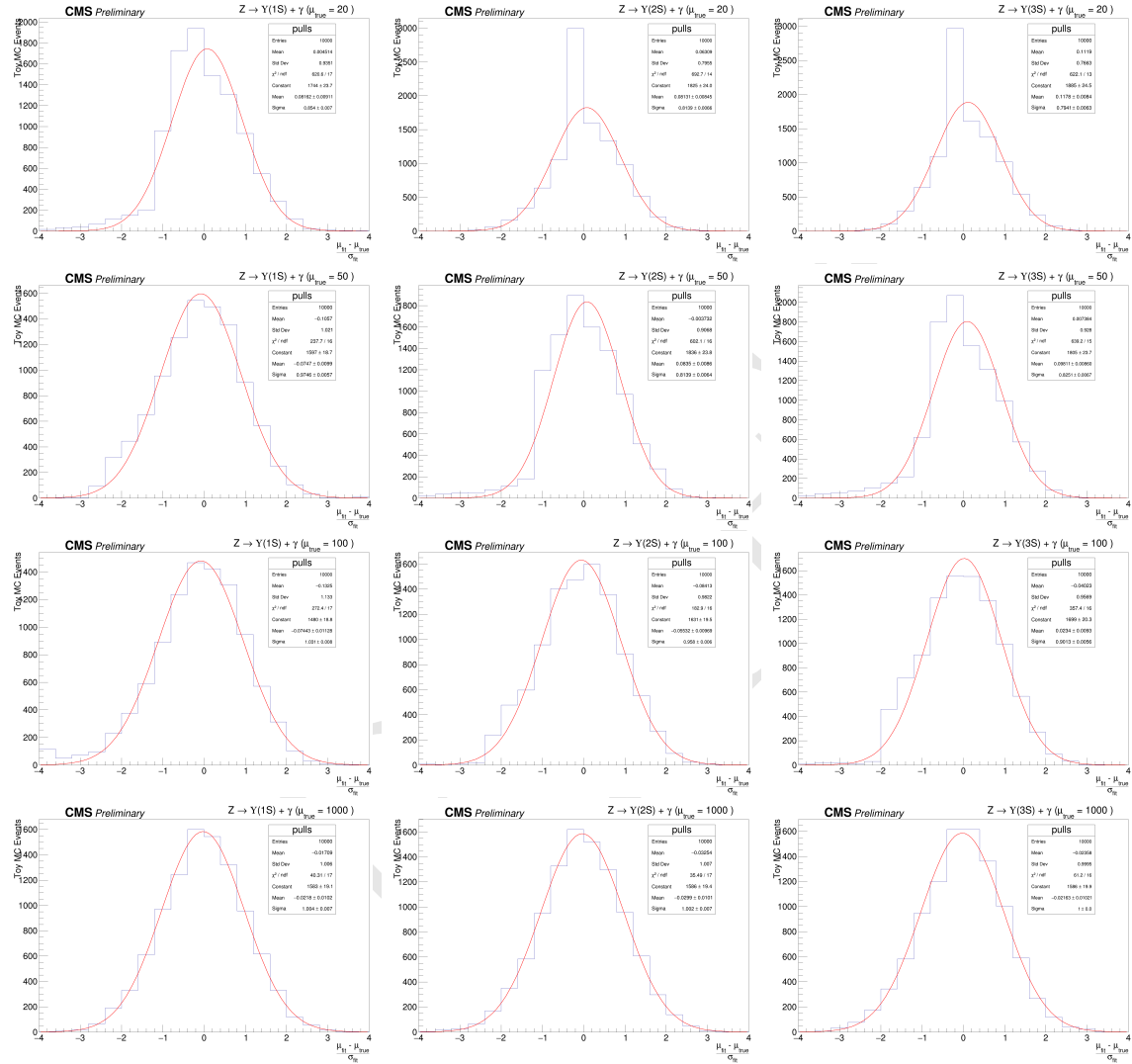


Figure 4.69: Distribution of pulls ( $\frac{\mu_{fit} - \mu_{true}}{\sigma_{fit}}$ ), for the Z decay analysis, after the toy dataset refit, for 1S, 2S and 3S (left to right), with  $\mu_{true}$  equals to 20, 50, 100, 1000 (top to bottom).

1117 As a general conclusion on this cross check, as long as the toy MC generation is able to inject enough  
 1118 signal to be fit, the final modeling of this analysis is able to recover a Gaussian pulls distribution.  
 1119 This, of course, depends on the Υ state to be considered. For the Z decay, between  $\mu_{true} = 50$   
 1120 and  $\mu_{true} = 100$  (around a hundred of events passing full selection), while for the Higgs decay, it  
 1121 is needed only a few events after full selection, even though it means hundreds of thousands times  
 1122 the expected signal, since the very small cross sections for the decay, as shown in Table 4.1.

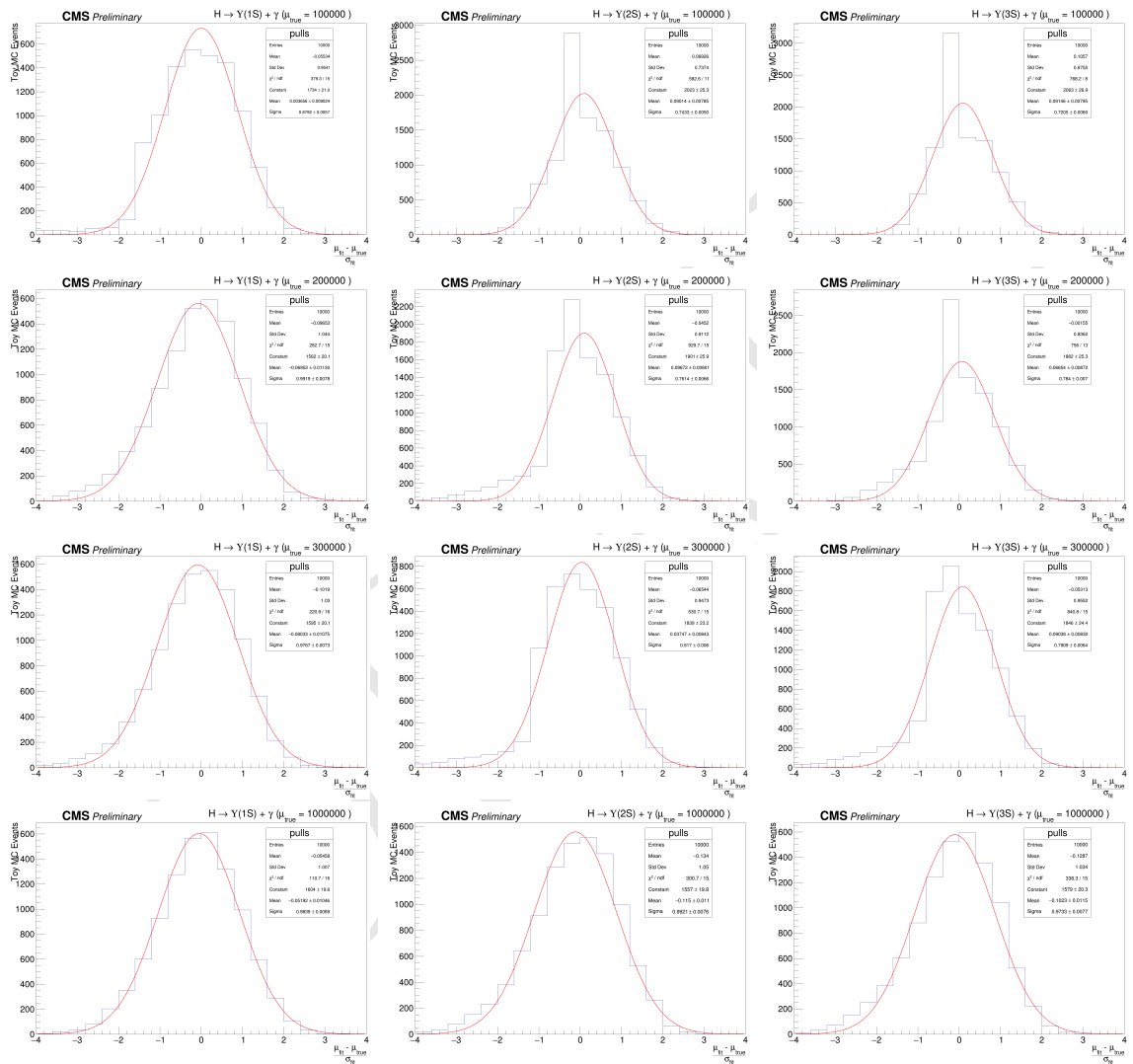


Figure 4.70: Distribution of pulls ( $\frac{\mu_{fit} - \mu_{true}}{\sigma_{fit}}$ ), for the Higgs decay analysis, after the toy dataset refit, for 1S, 2S and 3S (left to right), with  $\mu_{true}$  equals to 100000, 200000, 300000, 1000000 (top to bottom).

# 1123 5 Results and conclusion

1124 A two-dimensional (2D) unbinned maximum-likelihood fit to the  $m_{\mu^+\mu^-\gamma}$  and  $m_{\mu^+\mu^-}$  distributions  
1125 was used to compare the data with background and signal predictions. Search has been performed for  
1126 a SM Higgs and Z boson decaying into a  $\Upsilon(1S, 2S, 3S)\gamma$ , with  $\Upsilon(1S, 2S, 3S)$  subsequently decaying  
1127 into  $\mu^+\mu^-$  using data obtained from  $35.9 \text{ fb}^{-1}$  of  $pp$  collisions at  $\sqrt{s} = 13 \text{ TeV}$ .  
1128 Since no excess has been observed above the background, the  $CL_s$  formalism is applied, in order to  
1129 establish an upper limit in the branching fractions for each channel.

## 1130 5.1 The $CL_s$ formalism for upper limits setting at CMS

1131 The  $CL_s$  formalism [71] consist in a modified frequentist approach to obtain an upper limit for a  
1132 certain parameter of a model, with respect to the data, when there is no significant excess that could  
1133 justify an observation. It is based on the profile-likelihood-ratio test statistic [72] and asymptotic  
1134 approximations [73]. It is a standard upper limit setting procedure for the LHC experiments [74].  
1135 When searching for non-observed phenomena, it is often usual to derive the results as a function of  
1136 the signal strength modifier  $\mu$ , which is a free parameter of the full model (signal + background).  
1137 It can be define such as, the expectation value for the number of events in a bin <sup>1</sup> is:

$$E[n] = \mu s + b, \quad (5.1)$$

1138 where,  $s$  and  $b$  are the expected number of signal e background events, respectively.

1139 The Neyman–Pearson lemma [72] states the likelihood ratio is the optimal test between a null  
1140 hypothesis and an alternative one (i.e. background-only and signal-plus-background models). On  
1141 top on this, one could build a likelihood ratio test as:

$$q(\mu) = -2 \ln \left( \frac{\mathcal{L}(\text{data}|\mu s + b)}{\mathcal{L}(\text{data}|b)} \right), \quad (5.2)$$

1142 where the denominator and numerator defines the likelihoods for the background-only and signal-  
1143 plus-background models, respectively. The was the hypothesis test used by LEP and Tevatron  
1144 experiments (the former one, with some modifications to include the nuisances effects).

1145 With these two models, i.e. their *pdfs*, one can throw toy MC events in order to construct a  
1146 distribution of  $q(\mu)$ , namely  $f(q(\mu)|\mu)$ . The *p*-value of  $f(q(\mu)|\mu)$ , as below, can be used to chose  
1147 between each model.

$$p_\mu = \int_{q(\mu)_{\text{data}}}^{\infty} f(q(\mu)|\mu) dq(\mu), \quad (5.3)$$

1148 where  $q(\mu)_{\text{data}}$  is the observed value of  $q(\mu)$  on data, for a given  $\mu$ .

---

<sup>1</sup>A set of common analysis criteria.

If  $p_\mu$  is less than  $\alpha$  (usually 0.05 or 0.1) the background-only model can be excluded in favor of the signal-plus-background model. For the propose of a confidence interval estimation, the argument can be reversed and one could look for all the values of  $\mu$  that would not be excluded with Confidence Level (CL)  $1 - \alpha$ .

The problem with this definition is that, when the expected signal strength is very small, e.g. a invariant mass distribution in the TeV scale, the null hypothesis and the alternative one are almost indistinguishable. In this situation, a downward fluctuation of the background might lead us to exclude the alternative hypothesis (signal) in a region of low experimental sensitivity region. Putting in number, if we expect 50 background events and 2 signal events, but we observe 40 events, the signal would be easily excluded.

In order to take this effect into account, a modified frequentist approach for upper limits setting, the  $CL_s$  was proposed during the Higgs search era at LEP. Lets start by considering a profile likelihood ratio [75] as below:

$$\lambda(\mu) = \frac{\mathcal{L}(\text{data}|\mu, \hat{\theta})}{\mathcal{L}(\text{data}|\hat{\mu}, \hat{\theta})}, \quad (5.4)$$

where,  $\mathcal{L}(\text{data}|\mu, \hat{\theta})$  is the profile likelihood function.

Defining  $\mu$  and the investigated signal strength,  $\hat{\theta}$  is the nuisances that maximizes the likelihood for a given  $\mu$  (fixed) while  $\hat{\mu}$  and  $\hat{\theta}$  are the signal strength and nuisances that, overall, maximizes the likelihood. The advantage of the

CMS and ATLAS have a common set of statistical guidelines [76] to ensure the compatibility of the published results. Following these recommendations, the statistics test based on 5.4 is:

$$\tilde{q}_\mu = -2\ln[\lambda(\mu)], \text{ with } 0 \leq \hat{\mu} \leq \mu. \quad (5.5)$$

The left side restriction ( $0 \leq \hat{\mu}$ ) ensure us the proper physical interpretation of  $\mu$  as a positive define signal strength, i.e., the observation a process would, for a given bin, increase the number of events. The right side restriction  $\hat{\mu} \leq \mu$  secure the interpretation of  $\tilde{q}_\mu$ 's  $p$ -value as a one-sided confidence interval. This is required for a upper limit definition.

The advantage of using the profile likelihood ratio is that, even though it takes into account the effect of nuisances in the likelihood, it is possible to prove that, with the use of Wilk's Theorem [58], that a statistic test defined as  $\tilde{q}_\mu$ , asymptotically follows a chi-square distribution with one degree of freedom (the signal strength) [73]. Thus,  $\tilde{q}_\mu$  is said to be approximately independent of any nuisance and allow a fast computation of its  $p$ -value without the need of toy MC strategies (which can computationally demanding, depending on the complexity of the models), event though this is not the standard CMS/ATLAS recommendation.

Based on  $\tilde{q}_\mu$ , defined at 5.5, one should compute the  $\tilde{q}_\mu^{\text{obs}}$ , also the  $\hat{\theta}_\mu^{\text{obs}}$  and  $\hat{\theta}_{\mu=0}^{\text{obs}}$ , which corresponds to the observed value of  $\tilde{q}_\mu$  on data, the maximum likelihood estimator for the nuisances assuming some signal strength  $\mu$  and assuming a background-only model, respectively. Then, the distributions of  $f(\tilde{q}_\mu|\mu, \hat{\theta}_\mu^{\text{obs}})$  and  $f(\tilde{q}_\mu|\mu = 0, \hat{\theta}_{\mu=0}^{\text{obs}})$  are generated tossing pseudo-random toy MC. Figure 5.1 presents an example of these two distributions.

The  $CL_s$  value is defined as:

$$CL_s = \frac{p_{s+b}(\mu)}{1 - p_b}, \quad (5.6)$$

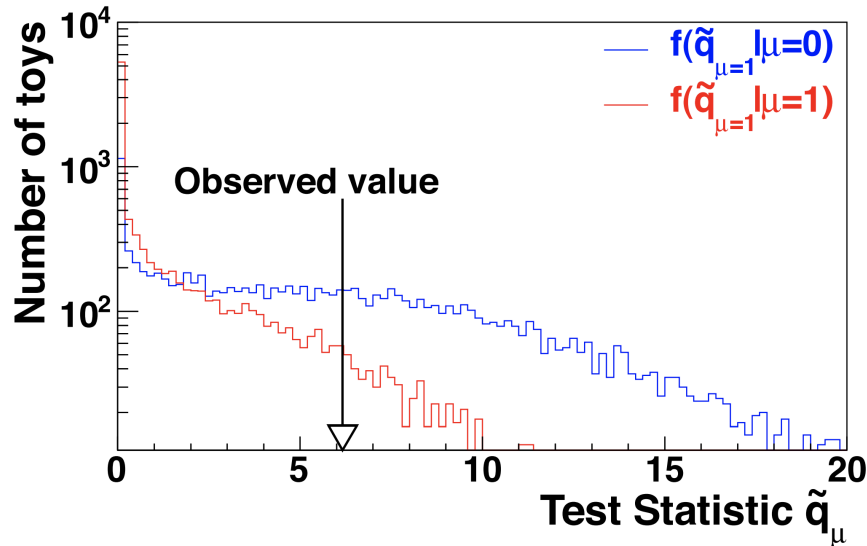


Figure 5.1: Example of  $f(\tilde{q}_\mu | \mu, \hat{\theta}_\mu^{\text{obs}})$   $f(\tilde{q}_\mu | \mu = 0, \hat{\theta}_{\mu=0}^{\text{obs}})$  distributions generated with toy MC.  
Source: [76].

1185 where:

$$p_{s+b}(\mu) = \int_{\tilde{q}_\mu^{\text{obs}}}^{\infty} f(\tilde{q}_\mu | \mu, \hat{\theta}_\mu^{\text{obs}}) d\tilde{q}_\mu \quad (5.7)$$

and

$$p_b = \int_{-\infty}^{\tilde{q}_\mu^{\text{obs}}} f(\tilde{q}_\mu | \mu = 0, \hat{\theta}_{\mu=0}^{\text{obs}}) d\tilde{q}_\mu \quad (5.8)$$

1186 Scanning different values of  $\mu$ , within  $0 \leq \hat{\mu} \leq \mu$ , one would exclude the ones which  $CL_s < \alpha$ . CMS  
1187 and ATLAS recommends a CL level  $(1 - \alpha)$  of 95%.

1188 The main advantage of the  $CL_s$  approach is that the presence of the denominator  $1 - p_b$  in 5.6  
1189 penalizes the exclusion of regions in which the experiment is no sensitive. Figure 5.2 helps to  
1190 illustrate this. One can notice that a small value of  $p_{s+b}$  (yellow area) is balanced by large value  
1191 of  $p_b$  (green area). When the experimental sensitivity is higher, the two distributions tend to be  
1192 far away from each other. Thus leading to a smaller compensation factor ( $p_b$ ) and enhancing the  
1193 chance of a exclusive  $CL_s$  value.

1194 The expected expected upper limit and its  $\pm 1\sigma$  and  $\pm 2\sigma$  are determined by generating a large  
1195 number of toy mc events, for the background-only model ( $\mu = 0$ ), with nuisances free to float,  
1196 and for each simulation finding  $\mu_{95\%}$ , which defines the confidence level. Once enough samples are  
1197 generated, one should scan, from left to right, the cumulative distribution of  $\mu_{95\%}$ . The median  
1198 defines the expected value and the quantiles for 16%, 84% and 2.5%, 97.5% defines the  $\pm 1\sigma$  and  
1199  $\pm 2\sigma$ , respectively.

## 1200 5.2 Branching fraction upper limits

1201 The result are summarized on table 5.1.

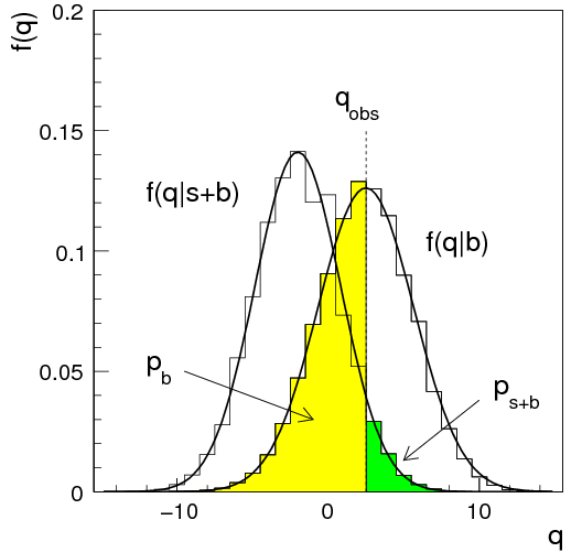


Figure 5.2: Example of  $f(\tilde{q}_\mu|\mu, \hat{\theta}_\mu^{\text{obs}})$ ,  $f(\tilde{q}_\mu|\mu = 0, \hat{\theta}_{\mu=0}^{\text{obs}})$  distributions generated with toy MC. In the figure,  $q$  must be read as  $\tilde{q}$ . The green area shows the  $p_{s+b}$  defined in 5.7, while the yellow one shows  $p_b$  defined in 5.8. Source: [73].

1202 The observed(expected) exclusion limit at 95% confidence level on the  $\mathcal{B}(Z \rightarrow \Upsilon(1S, 2S, 3S)\gamma) =$   
 1203  $2.9, 2.7, 1.4 (1.6^{+0.8}_{-0.5}, 2.0^{+1.0}_{-0.6}, 1.8^{+1.0}_{-0.6}) \times 10^{-6}$ , and on the  $\mathcal{B}(H \rightarrow \Upsilon(1S, 2S, 3S)\gamma) = 6.9, 7.4, 5.8$   
 1204  $(7.3^{+4.0}_{-2.4}, 8.1^{+4.6}_{-2.8}, 6.8^{+3.9}_{-2.3}) \times 10^{-4}$ .

1205 As stated before, this analysis was done, for the Z decay, taking into account a mutually exclusive  
 1206 categorization of events, based on the reconstructed photon properties ( $\eta_{SC}$  and R9 value), as  
 1207 described in section 4.7.

1208 At table 5.2 we present the results obtained when there is no categorization of events (Inclusive  
 1209 category).

1210 It is worth to remember that the categorization takes places only for the Z decay. For the Higgs  
 1211 decay, no categorization is imposed.

1212 By taking, or not, into account any categorization, the numbers presented in both tables (5.1 and  
 1213 5.2), are compatible within themselves and with the results published by the ATLAS collabora-  
 1214 tion [77].

95% C.L. Upper Limit			
	$\mathcal{B}(Z \rightarrow \Upsilon\gamma) [\times 10^{-6}]$		
	$\Upsilon(1S)$	$\Upsilon(2S)$	$\Upsilon(3S)$
Expected	$1.6^{+0.8}_{-0.5}$	$2.0^{+1.0}_{-0.6}$	$1.8^{+1.0}_{-0.6}$
Observed	2.9	2.7	1.4
SM Prediction [ $\times 10^{-8}$ ]	4.8	2.4	1.9
	$\mathcal{B}(H \rightarrow \Upsilon\gamma) [\times 10^{-4}]$		
	$\Upsilon(1S)$	$\Upsilon(2S)$	$\Upsilon(3S)$
Expected	$7.3^{+4.0}_{-2.4}$	$8.1^{+4.6}_{-2.8}$	$6.8^{+3.9}_{-2.3}$
Observed	6.9	7.4	5.8
SM Prediction [ $\times 10^{-9}$ ]	5.2	1.4	0.9

Table 5.1: Summary table for the limits on branching ratio of  $Z \rightarrow \Upsilon(1S, 2S, 3S)\gamma$  and  $H \rightarrow \Upsilon(1S, 2S, 3S)\gamma$  decays.

95% C.L. Upper Limit - $\mathcal{B}(Z \rightarrow \Upsilon\gamma) [\times 10^{-6}]$			
	without categorization		
	$\Upsilon(1S)$	$\Upsilon(2S)$	$\Upsilon(3S)$
Expected	$1.7^{+0.9}_{-0.5}$	$2.1^{+1.1}_{-0.7}$	$1.9^{+1.0}_{-0.6}$
Observed	2.6	2.3	1.2
	with categorization		
	$\Upsilon(1S)$	$\Upsilon(2S)$	$\Upsilon(3S)$
Expected	$1.6^{+0.8}_{-0.5}$	$2.0^{+1.0}_{-0.6}$	$1.8^{+1.0}_{-0.6}$
Observed	2.9	2.7	1.4

Table 5.2: Summary table for the limits on branching ratio of  $Z \rightarrow \Upsilon(1S, 2S, 3S)\gamma$ , for the two possible categorization scenarios.

DRAFT

# 1215 6 CMS Resistive Plate Chambers - RPC

- 1216 In the course of this PhD study, there were a lot of opportunities to work for the RPC project, in  
1217 the context of the CMS Collaboration. The main activities consists of shifts for the RPC operation  
1218 and data certification, upgrade and maintenance of the online software, R&D activities for the RPC  
1219 upgrade and detector maintenance during the LHC Long Shutdown 2 (2019 to 2020).
- 1220 In this chapter, it is presented a summary of the Resistive Plate Chamber technology and the  
1221 contributions to the RPC project at CMS.

## 1222 6.1 Resistive Plate Chambers

- 1223 The seminal paper on the Resistive Plate Chamber (RPC) technology was presented by R. Santonico  
1224 and R. Cardarelli, in which they described a "dc operated particle detector (...) whose constituent  
1225 elements are two parallel electrode Bakelite plates between" [78]. The key idea behind the RPC,  
1226 with respect to other similar gaseous detectors, is the use of two resistive plates as anode and  
1227 cathode, which makes possible to have a small localized region of dead time, achieving very good  
1228 time resolution.
- 1229 The working principle for RPCs relies on the idea that an ionizing particle crossing the detector, tends  
1230 to interact with the gap between the two plates (filled with some specific gas mixture) and form a  
1231 ionizing cascade process, in which the produced charged particles are driven by the strong uniform  
1232 electrical field produced by the two plates.
- 1233 The gas mixture is a key component of a RPC. Even though the first RPCs were produced with  
1234 a mixture of argon and butane, nowadays RPCs use a mixture of gases that would enhance an  
1235 ionization caused by the incident particle and quench secondary (background) effects.
- 1236 Another feature of the RPCs is its construction simplicity and low cost. This allows the use of RPC to  
1237 cover larger areas at a reasonable cost.
- 1238 An extensive review of the RPC technology and its applications can be found at [79].

### 1239 6.1.1 Principles and operation modes

- 1240 The core of a RPC chamber is a gap made with two parallel high resistivity plates, separated  
1241 by some regular distance (typically millimeters), filled with a proper gas mixture and under  
1242 appropriate high voltage (HV) applied on the plates (electrodes, from here on). When an ionizing  
1243 particle crosses the gap, there is a high enough chance the the particle will interact with the gas  
1244 and produce a newly created positive ion and an electron. This pair will travel in opposite directions,  
1245 according to the electric field from the electrodes. During this process, the electron will gain kinetic  
1246 energy and inelastically interact with other neighboring atoms/molecules, creating excitations in their  
1247 energy levels and, potentially, also ionizing them. The secondary ionization electrons will also follow  
1248 the same course, creating an **Avalanche** of positive and negative particles/ions traveling towards the

1249 electrodes. This process is proportional to the applied electric field. Figure 6.1 illustrates the  
 1250 avalanche production.

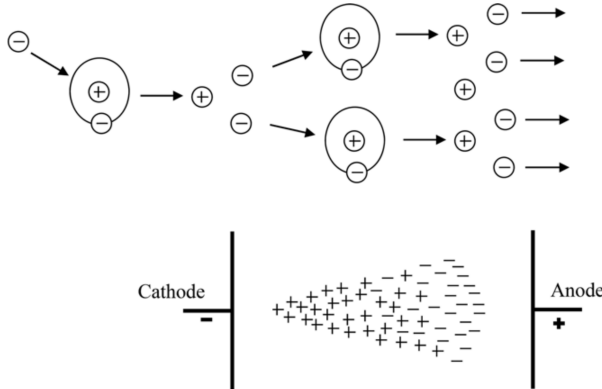


Figure 6.1: The Avalanche production process inside a RPC gap. (Top) The initial process and the secondary electron/ion generation. (Bottom) The overall charge distribution of an Avalanche between the electrodes. Source: [80].

1251 The number of particle composing the avalanche can be expressed as (assuming constant pres-  
 1252 sure) [80]:

$$n_e = n_0 e^{\alpha d} = n_0 A, \quad (6.1)$$

1253 where  $n_0$  is the number of initial electrons initiating the avalanche,  $A$  is the *gas gain*, or *multiplication*  
 1254 *factor* and  $d$  is the distance since the avalanche creation. This is also known as Townsend theory  
 1255 for discharges and  $\alpha$  is the first Townsend coefficient.

1256 When the positive ions bunch reaches the cathode, under certain conditions (if the first ionization  
 1257 energy of the ion is greater than the work function of the cathode), the recombination of the ion  
 1258 with the electrode material might release electrons which will also follow the electric field. The  
 1259 relative probability (with respect to the primary electron emission) of this emission to happen ( $\gamma_+$ )  
 1260 is called the the second Townsend coefficient.

$$n_+ = n_0 A \gamma_+. \quad (6.2)$$

1261 Another process which can occur is the secondary photoelectron productions, described by a similar  
 1262 equation as above:  $n_{pe} = n_0 A \gamma_{ph}$ . This production is mostly related to de-excitation of molecules  
 1263 and atoms in vicinity of the avalanche. The produced photons might initiate new ionization process.

1264 As an alternative to the Townsend theory, Raether, Meek, and Loeb, proposed the *streamer-leader*  
 1265 *theory* [81]. This theory is valid when there is a high enough concentration of ions  
 1266 produced. This critical value is called Raether limit.

$$n_0 A > 10^8 \text{ electrons} \quad (6.3)$$

1267 In this limit, the electric field created by the space distribution is high enough to be same order  
 1268 of the external field. In the vicinity of the head (or tail) of the avalanche the field gets disturbed  
 1269 and intensified. The intensification of the field enhances the ionization effect and give rise to  
 1270 secondary avalanches (photoelectrons). The intensified field also makes the photoelectrons produced  
 1271 travel towards the head (positive ions). Their antikuaption generates more UV radiation and more

secondary avalanches. This whole process is called **Streamer**. If no quenching is imposed, the streamer might evolve to a spark, fully discharging on the electrodes. If the concentration of electrons is high enough, the avalanche tail (electrons) might also give rise to a streamer (namely, negative streamer). Figure 6.2 illustrates the different subprocess related to streamer production.

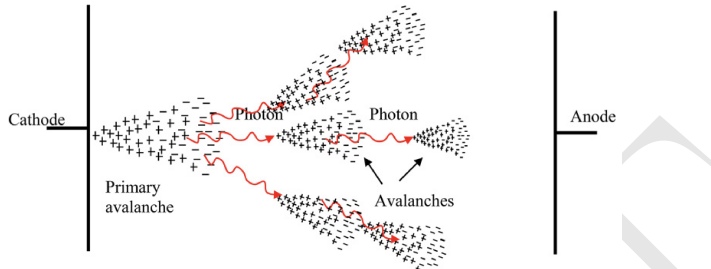


Figure 6.2: Streamer formation process. The distorted electric field around the high positive charge concentration enhances the ionization process, initiating secondary avalanches. Source: [80].

- A RPC where most of the charge multiplication process happens in the form of a streamer is said to be working in **Streamer Mode**. The advantage of the streamer mode is the high induced charge which is easily caught by non-sensitive readout electronics. On the other hand, the streamer mode, because of its highly associated charge, will have an impact in the rate capability of the detector (the local dead time will be higher).
- Because of the high background environment of LHC, the CMS RPC operates in **Avalanche Mode**, where discharge is highly quenched and very well localized. On the other hand, a very sensitive readout electronics is required to cope with the high rate demanded.
- A good review of electrical discharge on gases can be found at [80].

## 6.2 CMS Resistive Plate Chambers

At CMS, the Resistive Plate Chamber are installed in both the barrel and endcap region, forming a redundant system with the DT (barrel) and CSC (endcap). As described in the CMS Muon Technical Design Report (Muon-TDR) [82], the RPC are composed of 423 Endcap chambers and 633 barrel chambers. Figure 6.3 presents a picture of the CMS RPCs installed on station RE+4 of the Endcap.

Each chamber consists of two gas gaps (double gap), 2 mm tick each, made of Bakelite (phenolic resin) with bulk resistivity of  $10^{10} - 10^{11} \Omega m$ . The choice of the bulk resistivity of the electrode has high impact on the rate capability of the detector.

Each gap has its external surface is coated with a thin layer of graphite paint, which acts as conductive material, distributing the applied high-voltage (HV). On top of the graphite a PET film is used for isolation. A sheet of copper strips is sandwiched between the gaps. Everything is wrapped in aluminum case.

The double gap configuration increases the efficiency of the chamber, since the signal is picked up from the OR combination of the two gaps. A chamber with only one gap working, loses around 15% of efficiency, even though, this can be recovered by increasing the HV applied during operation mode (working point - WP).

A characteristic that differentiate the CMS RPC from previous RPC application in HEP is the operation mode. A RPC at CMS, operates in avalanche mode, while previous experiments used

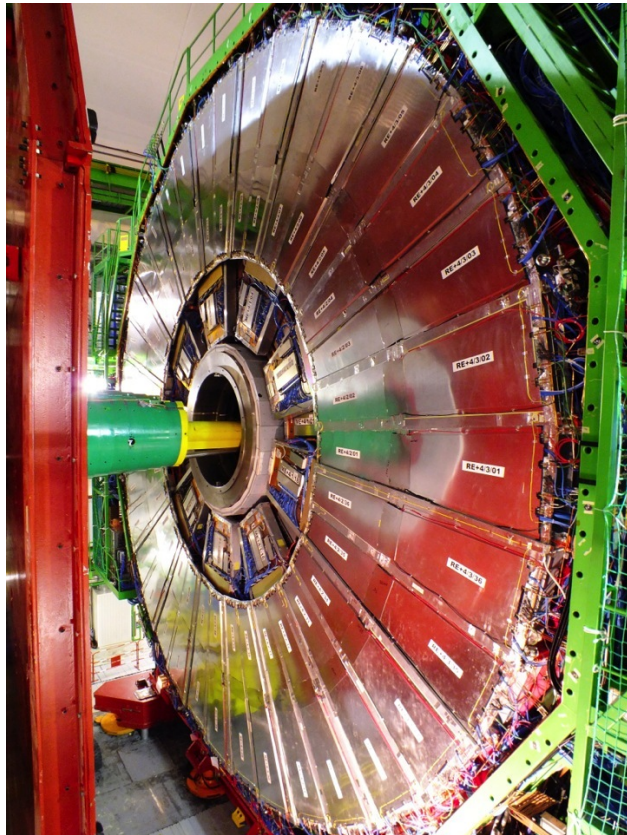


Figure 6.3: RPC chamber on installed on station RE+4 of CMS Endcap. Source: [83].

1304 the streamer mode. Both modes are related to the applied HV, in commitment with the strength of  
 1305 the generated signal, and are capable of generate a well localized signal, which can be picked up by  
 1306 the readout electronics, but the avalanche mode offer a higher rate capability around  $1 \text{ kHz/cm}^2$ ,  
 1307 while the streamer mode goes up to  $100 \text{ Hz/cm}^2$ . The high rate capability is a key factor in order  
 1308 to cope with requirements of the LHC luminosity, specially in the high background regions.

1309 Besides the rate capability, the key factors that driven the CMS RPC design were: high efficiency ( $>$   
 1310 95%), low cluster size ( $> 2$ ) for better spatial resolution (this reflects in the momentum resolution)  
 1311 and good timing in order to do the readout of the signal within the 25 ns of a LHC bunch cross  
 1312 (BX) and provide it to the CMS trigger system. These requirements have implications in the choice  
 1313 of material, dimensions, electronics and gas mixture.

1314 In the barrel, along the radial direction, there are 4 muon layers (called stations), MB1 to MB4.  
 1315 MB1 and MB2 is composed of a DT chamber sandwiched between two RPC chambers (RB1 and  
 1316 RB2) with rectangular shape. The stations MB3 and MB4 have only one RPC (RB3 and RB4) are  
 1317 composed by two RPC chambers (named - and + chambers with the increase of  $\phi$ ) attached to one  
 1318 DT chamber, except in sector 9 and 11, where there is only one RPC. RE4, sector 10 is a special  
 1319 case, since it is composed of four chambers (-, -, + and ++). These stations are replicated along  
 1320 the z direction in five different wheels of the CMS (W-2, W-1, W0, W+1 and W+2) and in twelve  
 1321 azimuthally distributed sectors (S1 to S12). Figure 6.4 show the different barrel stations and wheel.

1322 In the endcap, the RPC chambers have a trapezoidal shape and are distributed in four disks (or  
 1323 stations) each side (RE $\pm$ 4, RE $\pm$ 3, RE $\pm$ 2, RE $\pm$ 1), each one with 72 chambers. CMS split up its  
 1324 disks in 3 rings, along the radial direction, and 36 sector in the azimuthal angle. RPCs are present  
 1325 in the two outer rings (R2 and R3), in all 36 sectors. The RE $\pm$ 4 are special cases, since these  
 1326 chambers were installed only in 2014, a design choice was made the mechanically attached R2 and

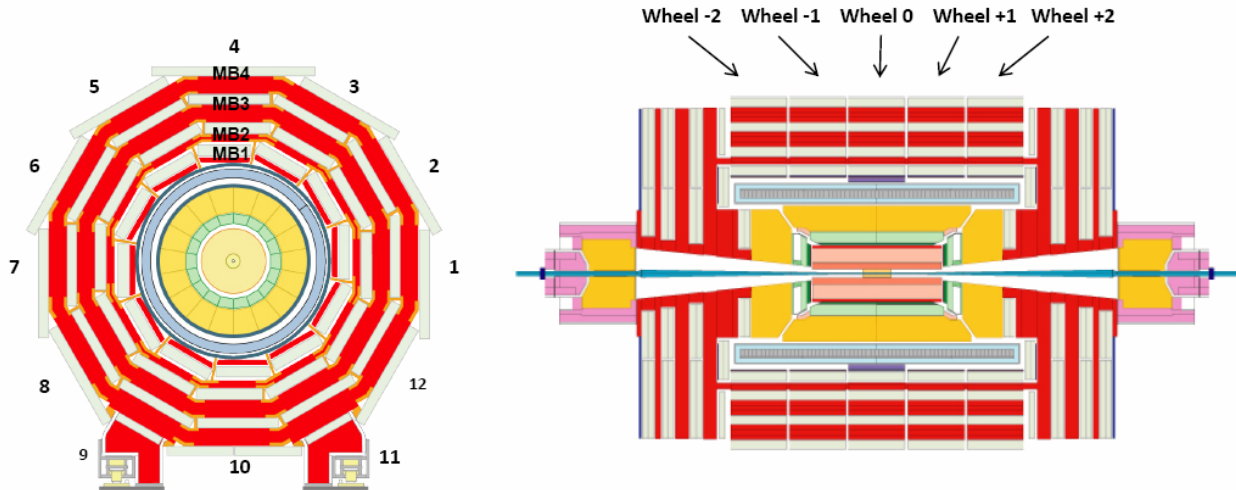


Figure 6.4: R- $\phi$  (left) and R-Z (right) projections of the barrel Muon System.

1327 R3 chambers, each sector, in what is called, a super-module. Figure 6.5 show the different endcap  
1328 disks.

1329 The length of the strips is chosen, for both barrel and endcap, in such a way to control the area of  
1330 each strip, in order to reduce the fake muons, due to random coincidence. This has to do with the  
1331 time-of-flight and signal propagation along the strip. In the barrel, each chamber readout is divided  
1332 in two regions (rolls), called forward and backward (along increasing  $|\eta|$ )<sup>1</sup>. In the endcap, the strips  
1333 are divided in 3 regions, called partitions A, B and C (from inside the detector to outside).

1334 The gas mixture used in the CMS RPCs is composed by C2H2F4 (Freon R-134a, tetrafluoroethane),  
1335 C4H10 (isobutane), SF6 (sulphur hexafluoride) (95.2 : 4.5 : 0.3 ratio) and with controlled humidity  
1336 of 40% at 20-22 °C. The Freon is used to enhance the ionization and charge multiplication that  
1337 characterizes the avalanche, while the isobutane is introduced for quenching proposes, in order to  
1338 reduce the secondary ionizations that could lead to formation of streamers and the SF6 is used  
1339 to reduce the electron background. The choice of Freon over other gases, i.e. argon-based and  
1340 helium-based, was motivated by previous studies [84, 85].

1341 Since its R&D, the RPC have shown good performance over aging. This is even historical over  
1342 previous RPC experiments [86–92]. Even the most recent studies of aging, taking into account  
1343 future LHC conditions (High-Luminosity LHC - HL-LHC) plus a safety margin of 3 times the  
1344 expected background ( $600 \text{ Hz/cm}^2$ ) have shown good aging hardness [93].

### 1345 6.2.1 Performance

1346 The RPCs, for the CMS experiment, contribute mainly with triggering inputs, due to its very good  
1347 time resolution. The important parameters which are monitored to evaluate the RPC performance  
1348 are the efficiency and cluster size. The former is related to the ratio of the registered hits over the  
1349 number of muons that passed through the chamber, while the former one is the number adjacent  
1350 strip (minimal readout unit) that were fired (activated) per hit. Figures 6.6 and 6.7 present the  
1351 historical distribution of efficiency and cluster size as a function of the integrated luminosity collect  
1352 during Run2.

<sup>1</sup>Some chamber are divided in three rolls, forward, middle and backward, for trigger propose.

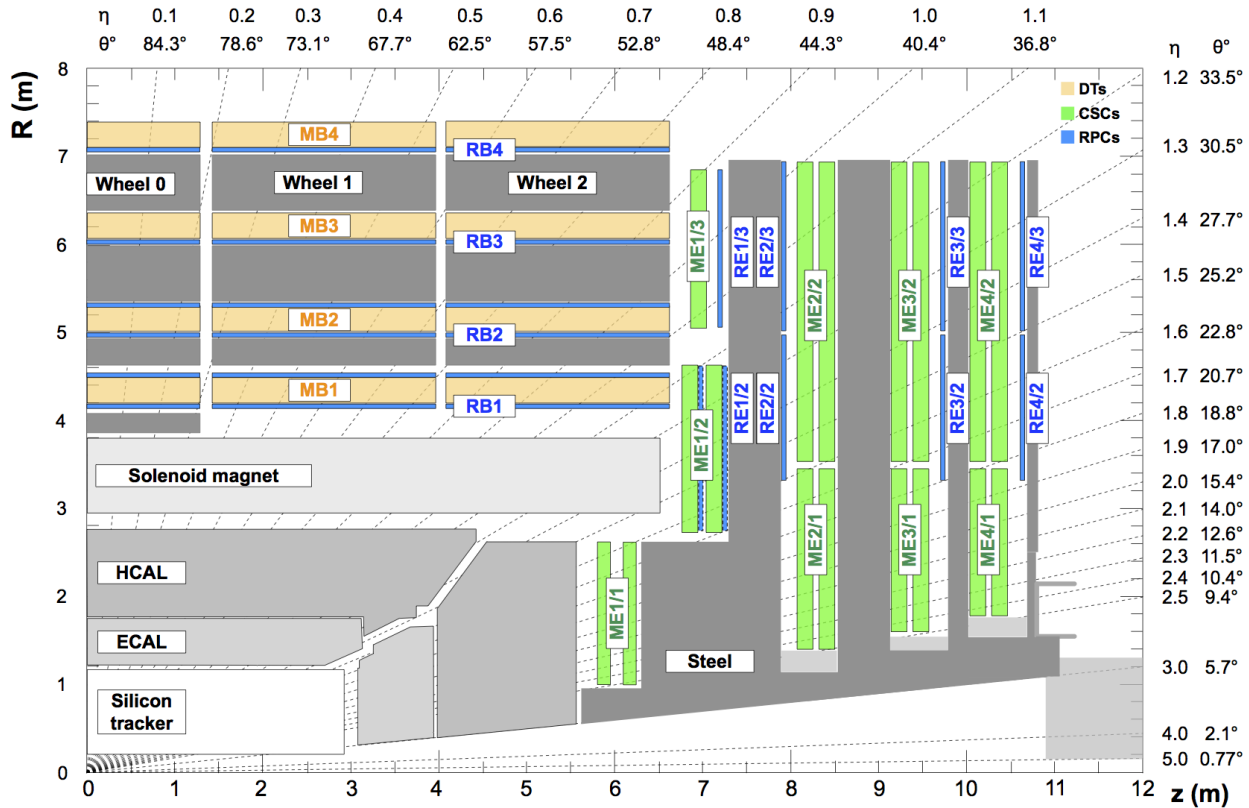


Figure 6.5: R-Z projections of the endcap Muon System (positive Z side). This is the same configuration for the  $36\phi$  sectors.

1353 In general, the RPC system operates with efficiency above 95% and cluster size smaller than 3  
 1354 (a good parameter established during the design phase). The importance of the efficiency is a  
 1355 less complicated concept to catch, on the other hand, the cluster size might not be so straight  
 1356 forward. The optimal regime of RPCs operation at CMS is the avalanche mode, in which the  
 1357 electrical discharge is constrained in a millimeter level size region. Another operation mode is the  
 1358 streamer mode, in which the initial discharge might trigger secondary ones, e.g. by the emission of  
 1359 unquenched photons. A streamer discharge is capable of fire neighbor strips, increasing the cluster  
 1360 size. Operating in avalanche mode is fundamental to keep the RPCs capable of dealing with the  
 1361 high background environment of CMS.

1362 To keep the mean cluster size under control ( $< 3$ ) is important to guarantees enough spatial reso-  
 1363 lution for the measurements (the geometrical position of a hit is the midpoint of the cluster) and  
 1364 ensures that the system has enough rate capability to operate, since a RPC with a high sensitive  
 1365 front-end electronics (necessary for the avalanche mode operation) could be degraded by pileup of  
 1366 dead time on many channels, including electronics noise, streamers, darks counts and other sources  
 1367 of background.

1368 A third important parameter to be measured and controlled in a RPC system, under the LHC  
 1369 conditions, is the current due to the high voltage applied. This current is known to be proportional  
 1370 to the total charge released in each electrical discharges and to the hit rate on the chamber. The  
 1371 voltage applied is divided, as in a series circuit, between the electrodes and the gap. At increasing  
 1372 background, the current also increases and, since the applied voltage is constant, the voltage across  
 1373 the gap is reduced in favor of the voltage across the electrodes. This reduction of effective voltage  
 1374 on the gas, might have an impact on its gain, imposing a reduction on the detector sensitivity.

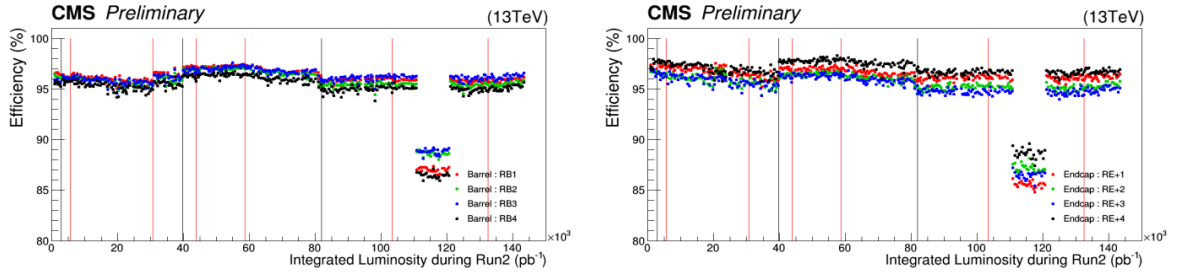


Figure 6.6: RPC efficiencies (per chamber) over Run2 Integrated Luminosity for Barrel (left) and Endcap (right). Red lines indicates technical stops (TS) while grey ones indicates Year-End-Technical stops (YETS). The drop in the efficiency around  $110 \text{ pb}^{-1}$  is related to a known operation mistake. Source: [94].

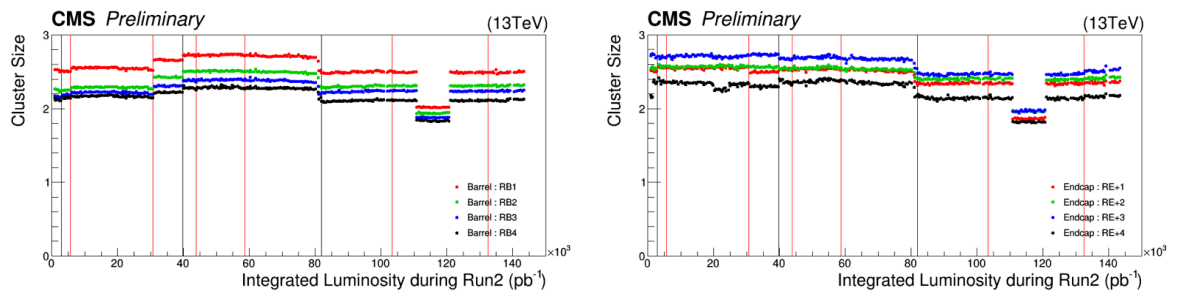


Figure 6.7: RPC cluster size (CLS - per chamber) over Run2 Integrated Luminosity for Barrel (left) and Endcap (right). Red lines indicates technical stops (TS) while grey ones indicates Year-End-Technical stops (YETS). The drop in the cluster size around  $110 \text{ pb}^{-1}$  is related to a known operation mistake. Source: [94].

Figure 6.8 presents the ohmic currents <sup>2</sup> in different regions of the detector, from 16<sup>th</sup> of April, 2018 to 2<sup>nd</sup> of December, 2018. It is clear how the stations subjected to higher background ( $RE \pm 4 - 40 \text{ Hz/cm}^2$ ) are subjected to a degrading factor that increases with the luminosity (background rate) and decreases when the detector is powered off. This effect is supposed to be related with the Hydrogen Fluoride (HF) production inside the gap, due to the electrical discharges. HF is a conductivity molecule, which can potentially attach to the internal surface of the gap, reducing the overall resistivity. The HF production can be controlled by properly tuning the gas flow as a function of the background that the chamber is subjected. HF concentration can also lead to permanent degradation of the gap, due to its chemical properties. Keeping the currents levels as low as possible is important for aging proposes.

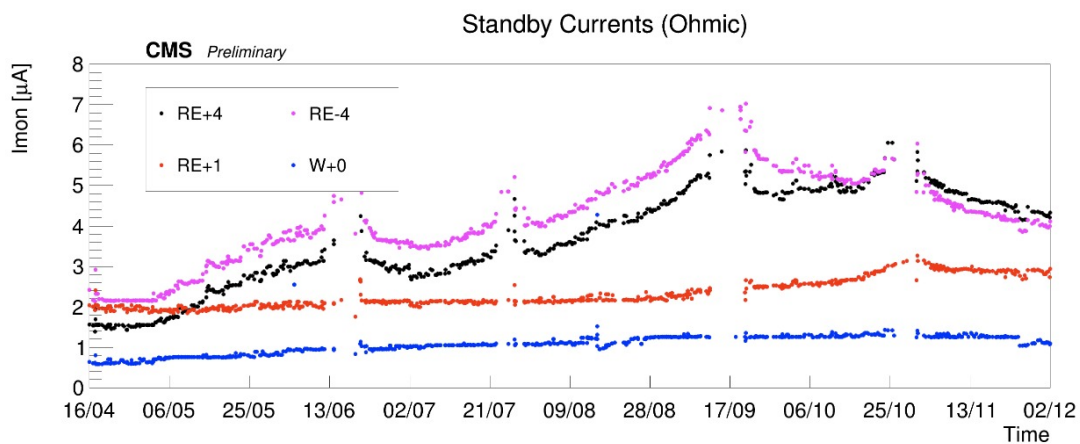


Figure 6.8: Ohmic current history of W+0, RE+1, RE+4 and RE-4. The blank regions, from time to time, corresponds to technical stops (TS), when the detector is off. Source: [94].

A review of the RPC performance during Run2 can be found at [94].

### 6.3 Contribution to the CMS RPC project

During the course of this study, a head collaboration of our research group and the CMS RPC project was established. Many contributions were given to the project as part of the graduation as a experimental particle physicist, with focus on getting acquaintance with a subsystem technology and give a meaningful collaboration to the detector operation. Those are considered by the community important steps on the student graduation.

Bellow it is described the contributions given to the CMS RPC project.

#### 6.3.1 RPC Operation - Shifts and Data Certification

The first activities done for the CMS RPC project were shifts for data certification of data taken. This certification is done by specialized people for different CMS subsystems and physics objects groups <sup>3</sup>.

<sup>2</sup>Current at 6500 V, which is below the typical working point of a CMS RPC (around 9500 V). In this region, no charge multiplication effect take place and chamber current is governed only by Ohm's Law.

<sup>3</sup>Groups of reconstruction and performance experts for different high-level reconstructed objects from CMS, i.e. muons, taus, jets/MET, electrons/photons

1397 This certification is done in order to ensure the quality of the date recorded based on the well  
 1398 functionality of each system during the data taking and the reconstruction of the physics objects in  
 1399 the expected matter. A certain collection of data (run) is said certificate when all subsystems and  
 1400 object experts agrees on this.

1401 Figure 6.9 shows, as an example of the luminosity delivered by the LHC, recorded one by CMS and  
 1402 the certified (validated), from the 22nd of April, 2016 to the 27th of October, 2016. Only certified  
 1403 data is available for physics analysis.

1404 Shifts are a continuous weekly activity (specially during the data taking period), performed in a  
 1405 weekly basis, in order to ensure the availability of certified data, as soon as possible.

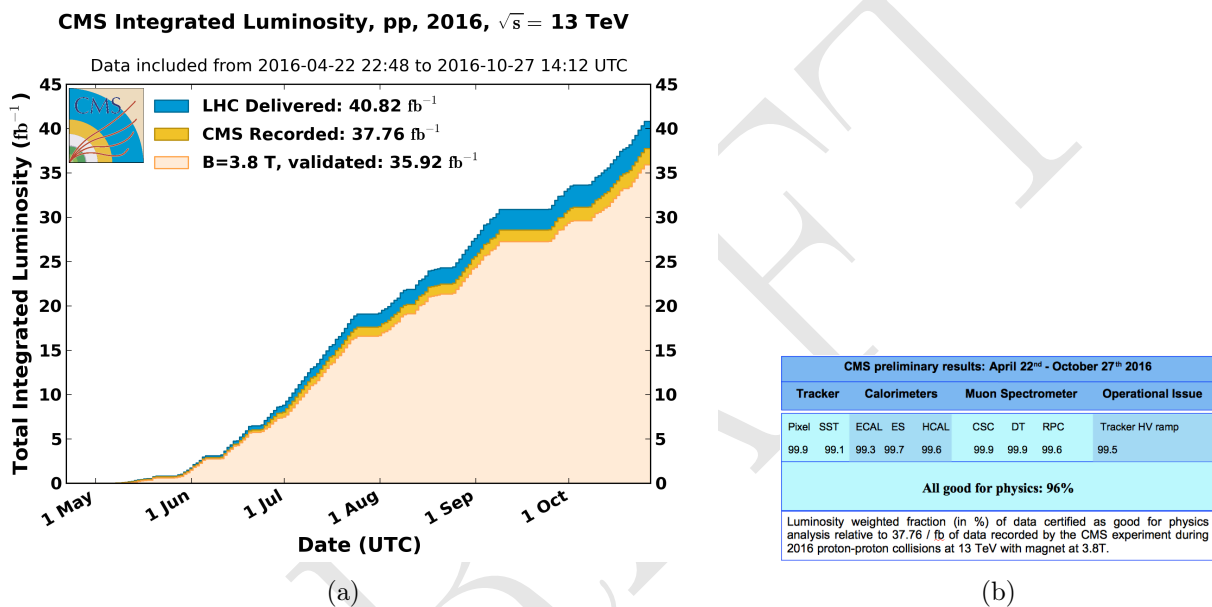


Figure 6.9: (a) Luminosity delivered by the LHC, recorded one by CMS and the certified (validated), from the 22nd of April, 2016 to the 27th of October, 2016. (b) Efficiency of the certification process for each subsystem, from the 22nd of April, 2016 to the 27th of October, 2016. Total CMS efficiency is above 90%. Source: [95]

## 1406 6.4 RPC Online Software

1407 On what concerns the Online Software (OS) of the CMS RPC system, the main contribution given  
 1408 was the upgrade of the Trigger Supervisor libraries.

1409 The Trigger Supervisor is a web-based software, which run over the xDAQ backend and provides,  
 1410 through a modules organized in a tree system, called cells, a standard interface for the operation and  
 1411 monitoring of different system at CMS. In principle only systems which contribute directly to the  
 1412 L1 trigger should have a Trigger Supervisor implementation. This was the case for the RPC during  
 1413 the Run1. Since Run2, RPC contributes to the trigger indirectly, by providing data to the muon  
 1414 processors (CPPF, OMTF and TwinMux). The Trigger Supervisor implementation is a legacy from  
 1415 that period.

1416 Each subsystem is responsible for its own implementation of the Trigger Supervisor, based on the  
 1417 functionalities that it wants to have (requirements). The xDAQ [96] is a middleware, developed by  
 1418 CERN and widely used at CMS, as a tool for control and monitoring of data acquisition system in

1419 a distributed environment. It is capable of providing a software layer for direct access of hardware  
 1420 functionalities and monitoring.

1421 The upgrade made (figure 6.10), consists in upgrade the higher level of the RPC online software.  
 1422 In summary, up to 2017, the online software, was using Scientific Linux 6 as operational system,  
 1423 which executed xDAQ 12, in turn, servers as backend for Trigger Supervisor 2. A upgrade of  
 1424 the operational system to Centos 7, demanded the upgrade to xDAQ 14. On top of that, Trigger  
 1425 Supervisor 2 would not work and had to be updated to Trigger Supervisor 5 in order to be functional  
 1426 in 2018.

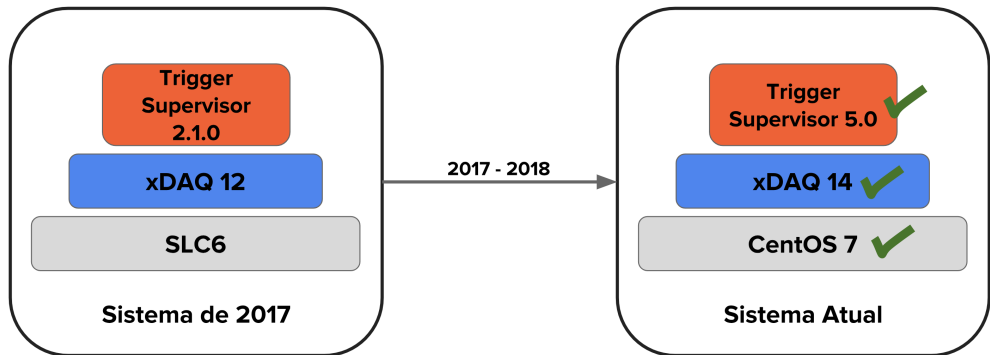


Figure 6.10: Upgrade of the RPC online software.

1427 Between versions 2 and 5 of Trigger Supervisor, part of the source-code had to be reworked, keep  
 1428 the majority of the code structures. Most of the changes were made in the front-end of the system.  
 1429 The standard JavaScript library Dojo [97], used in version2, was deprecated in favor of Google's  
 1430 Polymer[98]. The main reason for this change was to isolate C++ code from HTML, which was  
 1431 impossible with Dojo. This implied to rewrite all the screen of the RPC Trigger Supervisor imple-  
 1432 mentation, as in figure 6.11.

1433 The upgrade was done in time to ensure the control and operation of the RPC for 2018 data taking.

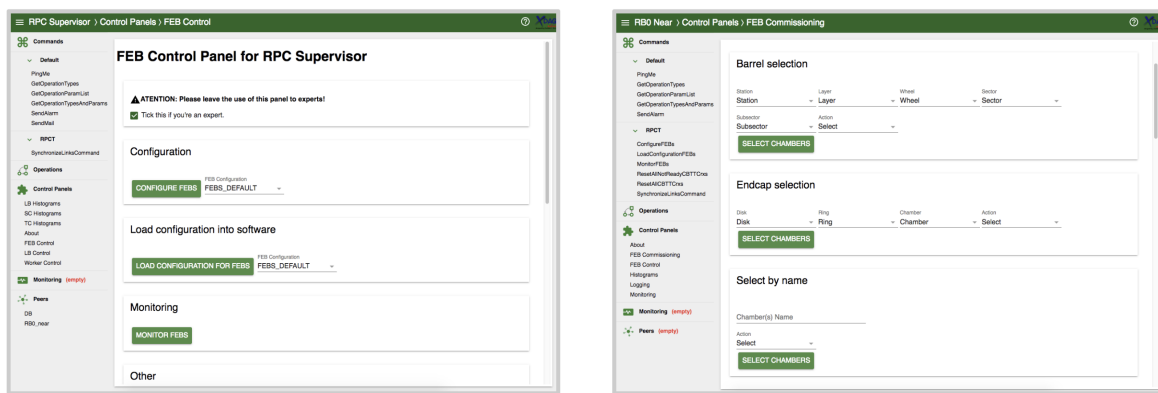


Figure 6.11: Example of the updated screens, using Trigger Supervisor 5.

#### 1434 6.4.1 iRPC R&D

1435 For the next 4 year of CMS activities it is foreseen the upgrade of the the Muon Systems [82].  
 1436 These upgrades are planed in order to extend the pseudorapidity coverage ( $\eta$ ) and to guarantee the  
 1437 operation conditions of the present system in the HL-LHC (High Luminosity LHC) era. The RPC  
 1438 (Resistive Plate Chambers) [82] subsystem, it will have maintenance of the present chambers and

1439 installation of new chambers in the region of  $|\eta| < 1.8$  para  $|\eta| < 2.4$  [99]. These new chambers  
 1440 (iRPC) will be added in the most internal part of the muon spectrometer, RE3/1 e RE4/1, as in  
 1441 Figure 6.12.

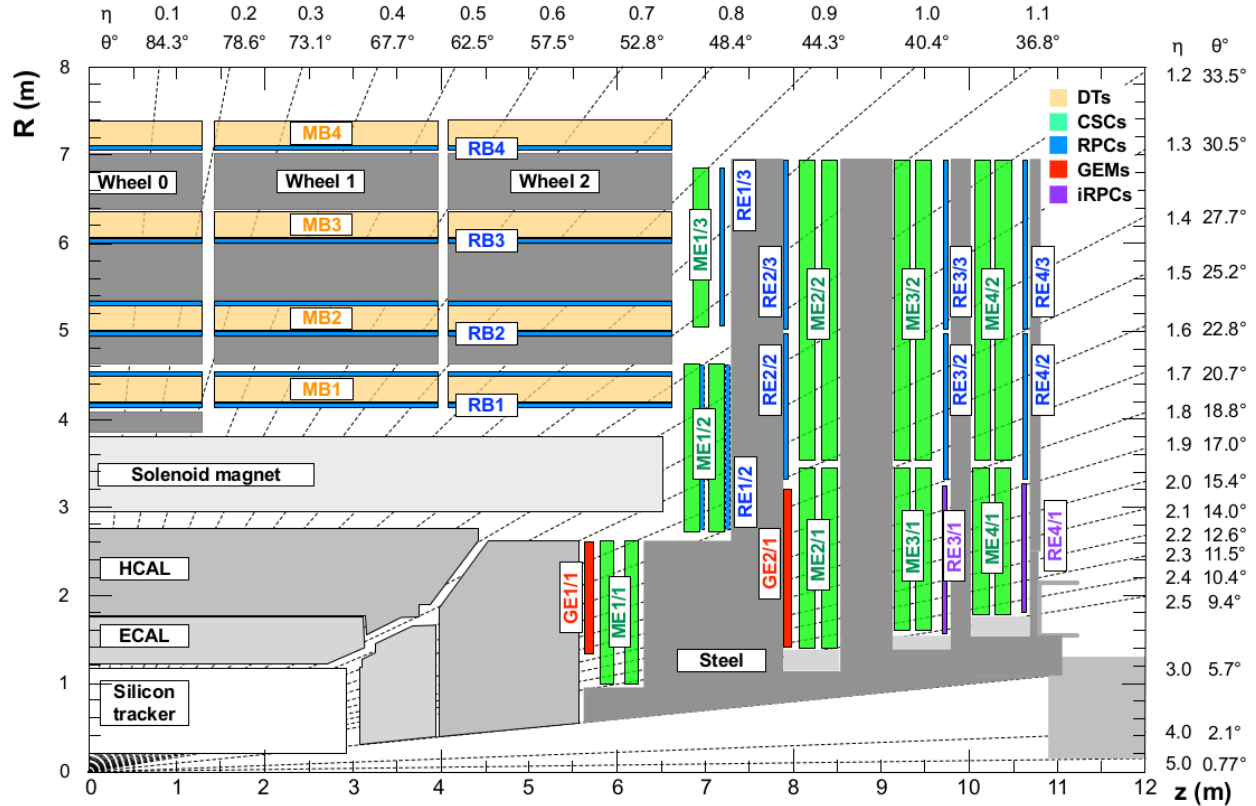


Figure 6.12:  $\eta$  projection of the Muon System subdetectors. In purple, is labeled the iRPCS to be installed during the CMS upgrade.

1442 Even thought this region is covered by the CSC detectors CSC (Cathode Strip Chambers), there  
 1443 are some loss of efficiency due the the system geometry. The installation of additional chambers will  
 1444 mitigate this problem and potentially increase the global efficiency of the muon system. The new  
 1445 chamber, called iRPC (*improved RPC*), will be different them the present one. For a luminosity of  
 1446  $5 \times 10^{34} \text{ cm}^{-2} \text{s}^{-1}$  the neutrons, photons, electrons and positrons background in the high  $|\eta|$  region  
 1447 is expected to be around  $700 \text{ Hz/cm}^2$  (for the chambers in RE3-4/1). Applying a safety factor  
 1448 of 3, the new chambers should support up to  $2 \text{ Hz/cm}^2$  of gamma radiation and still keep more  
 1449 than 95% of efficiency. Studies indicate, so far, that the use of High Pressure Laminates (HPL) for  
 1450 the double gap chambers is the most suitable choice. In order to reduce the aging and increase the  
 1451 rate capability, the electrodes and the gap size should be reduced in comparison with the present  
 1452 system.

1453 One of the challenges for the R&D of the iRPC chambers is measuring the their performance in  
 1454 a high radiation environment, as the one for HL-LHC. For this, the CMS RPC project uses the  
 1455 Gamma Irradiation Facility (GIF++) [100], at CERN. The GIF++ is located at the H4 beam line  
 1456 in EHN1 providing high energy charged particle beams (mainly muon beam with momentum up to  
 1457 100 GeV/c), combined with a 14 TBq 137-Cesium source. In the GIFF++ it is possible to achieve  
 1458 the HL-LHC total dose in a much reasonable amount of time. With the shutdown of LHC, the  
 1459 muon beam source is also off and will stay like this for 3 years. This means that the only muon  
 1460 sources for studies in GIF++ are cosmic muons.

In order to create a trigger system for iRPC R&D, the usual procedure is to use scintillators, on the top and on the bottom of the chamber. This is effective, but in a high gamma radiation environment, scintillators can be very sensitive which could lead to an undesirable amount of fake triggers which can degrade the measurements. Also, if one wants to covers a large area with scintillators, this can be expensive and they will not provide any means of tracking to measuring not only the global, but also the local chamber performance.

To provide a solution, the CMS RPC got in agreement with the LHCb [101] Muon Project to use their Multiwire Proportional Chambers (MWPC) [102], which were removed from LHCb, to be replaced by new chambers, and use them as trigger and/or tracking system at GIF++. This chambers, by design, have relatively low gamma sensitivity, already have some 1-dimensional resolution ( $O(cm)$ ) and, the biggest advantage, with respect to any other gaseous particle detector option: LHCb has hundreds of vacant chambers. Any other detector would have to be build.

Not going in details of the MWPC technology nor the LHCb chamber construction [103], these chambers have a total active area of  $968 \times 200 mm^2$  divided 2 layers (top and bottom) of 24 wire pads ( $40 \times 200 mm^2$ ) composed of around 25 wires/channel, grouped by construction. Each chamber is equipped with 3 FEBs (Front-End Boards) with 16 pads each.

A channel is a logical combination of a top layer (pads) and a bottom layer readout. These readouts can be combined in AND or OR logics. One can have 8 channels per FEB, each channel being a logical combination of top and bottom pads. In this mode they are called AND2 and OR2. It is also possible to have the FEB configured in a 2 channels mode, each one corresponding to one sixth of the total readout pads. In this mode, all the pads can be combined in OR (called OR8) or they can be AND'ed in top and bottom pads and then group in OR (called OR4AND2). Figures 6.13 and 6.14 presents a logical diagram for each readout mode.

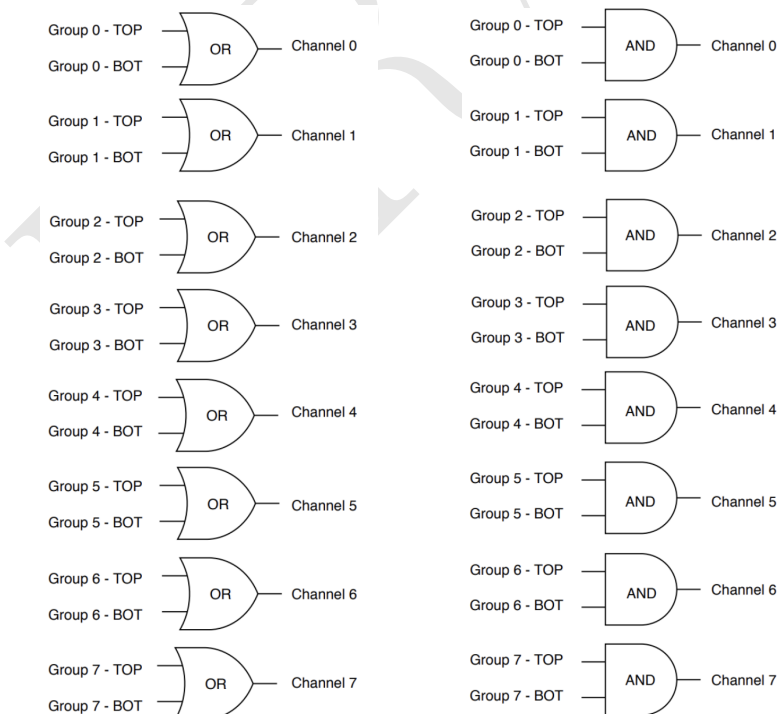


Figure 6.13: FEB configured 8 channels modes. Group should be understood as wire pad. Left: Logical diagram for OR2. Right: Logical diagram for AND2.

The nominal gas mixture for these chambers is Ar/CO<sub>2</sub>/CF<sub>4</sub> (40:55:5). For a matter of simplicity, it was used an already available similar gas line in the same building, used by CMS CSC (Cathode

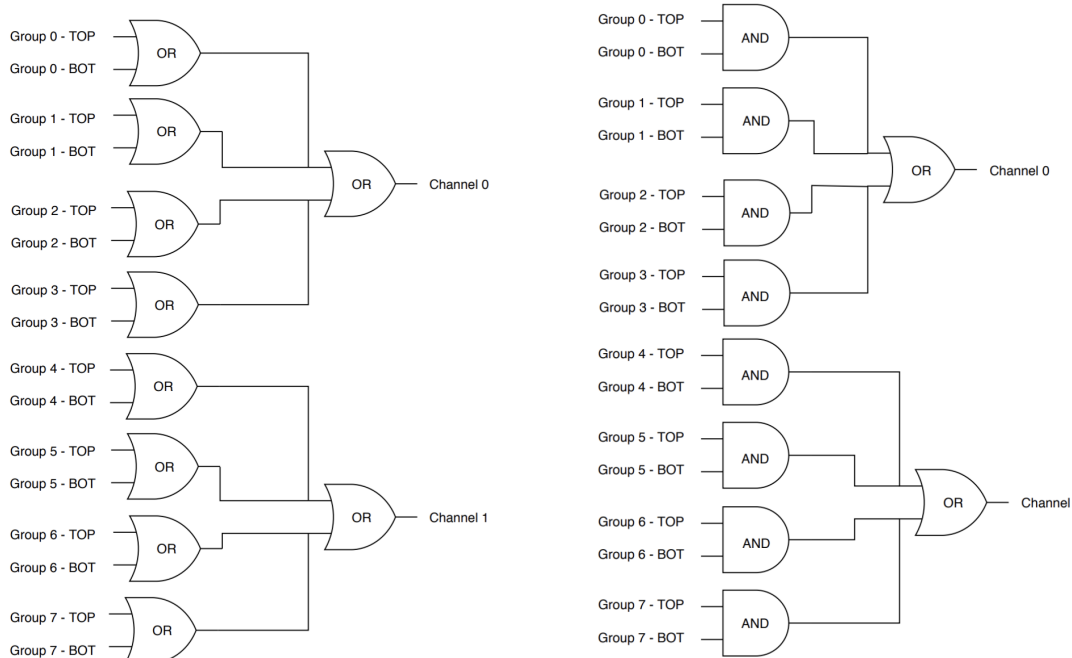


Figure 6.14: FEB configured 2 channels modes. Left: Logical diagram for OR8. Group should be understood as wire pad. Right: Logical diagram for OR4AND2.

1486 Strip Chamber) [82], which has a similar composition (40:50:10). Optimal conditions are obtained  
1487 with 2 to 4 liters/hour of gas flux and 2.65 kV of applied voltage.

1488 Figure 6.15 shows the setup that was prepared for commissioning of this chambers. It was mounted  
1489 two chambers on top of another (chambers A and B) above an RPC R&D chamber and two other  
1490 chambers on the bottom (chambers C and D). These four MWPC will be used as telescope for  
1491 the RPC chamber. All the services were mounted in rack, as in Figure 6.15. This includes power  
1492 supply (low voltage and high voltage), distribution panel, VME crate and boards for FEB control,  
1493 computer for control (high voltage, and FEB control) and NIM crate and boards for LVDS to NIM  
1494 signal conversion, logics and counting.

1495 Due to the short amount of time available for the commissioning, only two measurements mea-  
1496 surements were made with these chambers. They were meant to be a proof of concept for future  
1497 activities.

1498 The first measurement was to measure the coincidence rate of two chambers as a function of the  
1499 distance between the two top planes (Figure 6.16). This measurements were done with nominal  
1500 working point, with one FEB configured in 2 channels mode with 7 pC threshold, in (160 mm x  
1501 160 mm) area per chamber. One can observe that, if we go for a telescope trigger in the order of  
1502 1 meter of separation between the chamber, the logical combination chosen has negligible effect in  
1503 the coincidence rate. Also, the fits can be used to estimate the rate in a configuration with chamber  
1504 on the roof and under the floor. This could be the case of a universal trigger, to be mounted in  
1505 GIF++ with these chamber.

1506 The second measurement consist on evaluate the impact of  $\gamma$  background by placing a small Cs-137  
1507 source on top of the chamber A (Figure 6.17). For this measurement, the distance between top  
1508 planes of each pair of chamber (A to B and C to D) is 65 mm, while the distance between the top  
1509 planes of A and C is 570 mm. It is clear the the  $\gamma$  source has an impact on chamber A rate, but  
1510 this is negligible when we take into account the coincidence between two chambers.

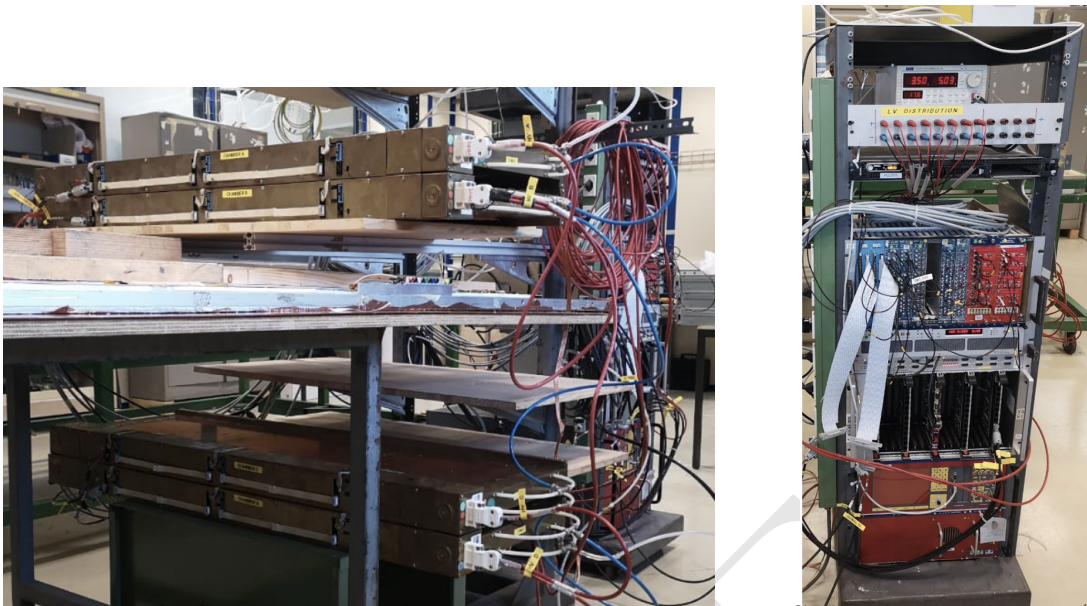


Figure 6.15: Left: Setup mounted for commissioning. Two MWPC chamber on the top (chambers A and B) and two (chambers C and D) on the bottom with a RPC R&D in the middle. Right: Rack with all the services for the operation of these chambers.

1511 This two measurements were enough to validate this chambers as possible trigger pro RPC R&D  
 1512 with cosmic muons in the laboratory and at GIF++. The next steps would be use this MWPC  
 1513 chamber to implement a tracking system from triggering. This would demand some developments,  
 1514 since, due to bandwidth restrictions, the signal from each FEB would have to go to a programmable  
 1515 fast electronics, i.e. a FPGA, which would reconstruct muon tracks and provide the trigger to the  
 1516 DAQ system. This can be done by placing the two pair of chambers (AB and CD) in orthogonal  
 1517 configuration and read the signal in a CAEN V2495 board [104].

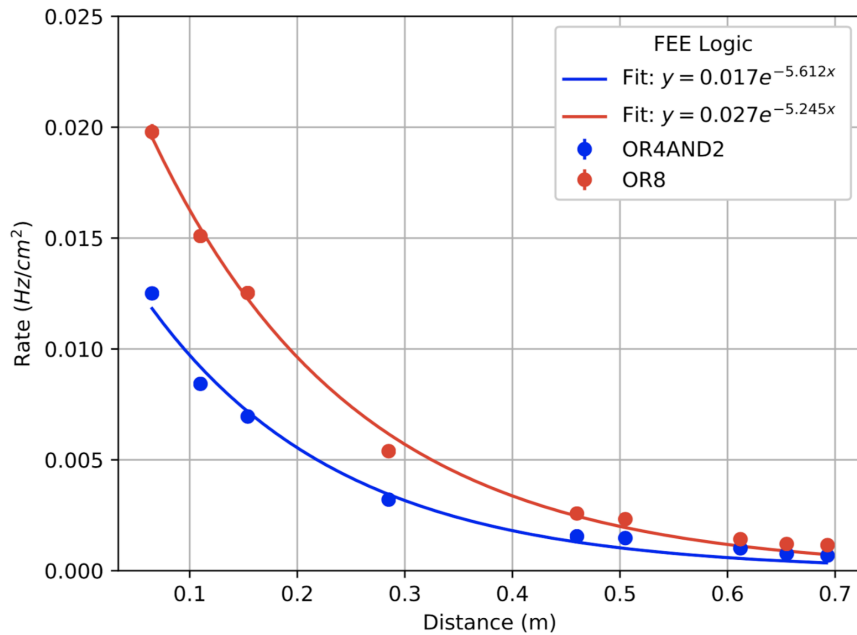


Figure 6.16: Coincidence rate of two chambers with respect to an arbitrary distance between the two top planes. Measured in 10 minutes, for 2 logical combinations (OR8 and OR4AND2). Applied high voltage: 2.65 kV. Threshold: 7 pC. Active area: readout of 160 mm x 160 mm per chamber.

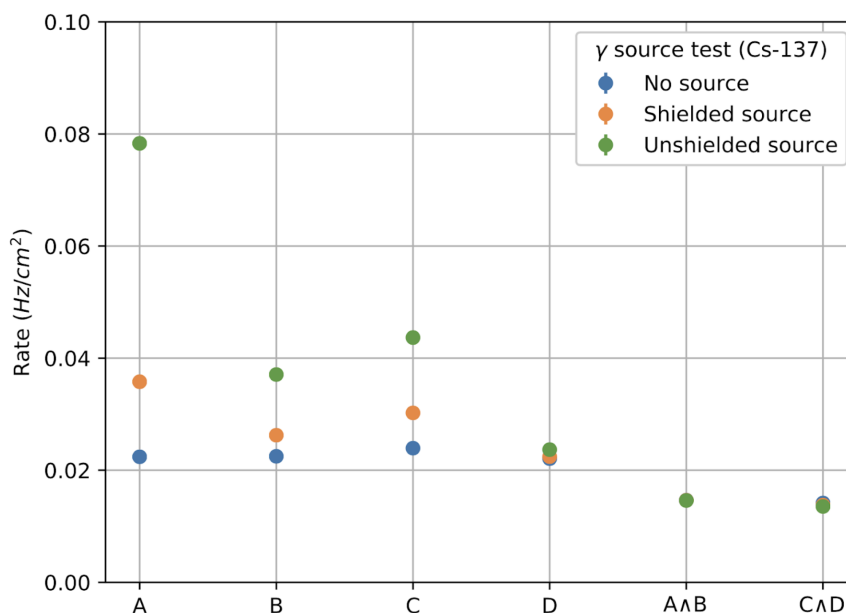


Figure 6.17: Individual rates (chambers A, B, C and D) and coincidence rates for two chambers (A AND B, C AND D), for without  $\gamma$  source (blue), a shielded  $\gamma$  source (orange) and an unshielded  $\gamma$  source (green). Source sitting on top of chamber A. Applied high voltage: 2.65 kV. Threshold: 7 pC. Active area: readout of 160 mm x 320 mm per chamber. Logical combination: AND2

### 1518 6.4.2 LS2 and the RPC Standard Maintenance

1519 In December 2018, the LS2 (Long Shutdown 2) was started. This a period in which the LHC and  
 1520 its detectors (CMS included) stop their operation for maintenance and upgrade. The LS2 will go  
 1521 up to 2021, when LHC and CMS restart the data taking with the Run3.

1522 During the LS2 it is being installed services for the new chambers (gas pipes, low voltage (LV), cables,  
 1523 signal and control optical fibers, high voltage (HV) cable and support equipment, and HV/LV power  
 1524 supplies), as well as continuity to the to the RPC R&D studies, besides the reparation of broken  
 1525 elements of the present system, i.e. chamber in the barrel region which present gas leak problems,  
 1526 maintenance of the LV and HV connectivity and power system, maintenance of the control system  
 1527 of problematic chambers (Front-Ends boards, cabling and Distribution Boards) and the dismount  
 1528 and reinstallation of four stations in the endcap (RE4) on both sides of CMS [105].

1529 What concerns the standard maintenance of the present RPC system, the main LS2 activities in  
 1530 which the student was involved, can be divided in three main tasks: (a) HV maintenance, (b) LV  
 1531 and control maintenance and (c) detector commissioning.

#### 1532 HV maintenance

1533 A key factor of and RPC performance is the applied high voltage (HV). The CMS RPC achieve  
 1534 their optimal performance with, around, 9.5 kV applied in each gap. This voltage is in the range  
 1535 of the dielectric breakdown of many gases, which could lead to potential current leakages, if some  
 1536 part of the system is damaged, poorly operated or badly installed. If the currents are high enough  
 1537 this can make impossible the operation of the chamber. In cases like this, during the operation  
 1538 period (data taking), the problematic HV channel is identified and turned off (each chamber has  
 1539 two channels, one for each layer of gaps). Chambers in this situation are said to be operating in  
 1540 single gap mode (SG).

1541 The goal for the HV maintenance is to, now that the CMS is off and the chambers are accessible,  
 1542 identify which part of the HV supply system is causing the current leak and fix it the best way  
 1543 possible. Usually the problem is beyond the power supply, very often connectors or the gap itself  
 1544 are damaged.

1545 The CMS RPCs uses two kind of HV connectors, monopolar and tripolar connector. The monopolar  
 1546 are used to connect the chamber to the power supply. If mounted properly, rarely they present  
 1547 problems. The connection to the chamber is made by tripolar connectors, in which the ground and  
 1548 the HV for both gaps arrives to the chamber in a single connector, for simplicity and to save space in  
 1549 the patch panel. Unfortunately these connectors are relatively fragile, and they could be a potential  
 1550 source of leak, specially if they were poorly mounted, badly operated or with aging itself. Also,  
 1551 since this was a connector made exclusively for the CMS RPC system, some design choices had to  
 1552 be improved after the installation of other chamber. Those installed with old batches of tripolar  
 1553 connectors are sensitive ones. The reparation of this connectors consists in isolate the connector  
 1554 from the chamber and power it up to 15 kV (maximum voltage allowed by the system). If the tested  
 1555 connector is broken one will observe a very fast increase in the current of the HV channel. The only  
 1556 solution to this kind of problem is to replace the connector.

1557 On the other hand, if the connector is powered isolated and pass the test, the problem beyond  
 1558 the connector (assuming that the power system have already been tested), i.e. inside the chamber.  
 1559 When a chamber is in SG mode it means that a full layer is off, but not necessarily all the gaps  
 1560 in that layer are bad (a RPC can have up to three per layer). In this situation, the procedure  
 1561 consists in cutting the cables that comes from the gaps to the chamber side connector one by one  
 1562 and identify which gap of the problematic layer is the broken by powering it. Once identified, this

1563 gap should be isolated and the other ones reconnected. The broken gap is unrecoverable, since it is  
 1564 inside the chamber, but 5% to 10 % of efficiency can be retaken, without changing the applied HV  
 1565 and increasing the longevity of the chamber.

1566 Another contribution to the HV maintenance was the proposal of a procedure to replace the prob-  
 1567 lematic tripolar connector by a monopolar (also called jupiter) connector, which are known for being  
 1568 much more stable and reliable. The figure 6.18 (left) show the designed adapter for the chamber  
 1569 patch panel which would make this change possible. Figure 6.18 (right) shows a tryout of a cham-  
 1570 ber in which this procedure was tested. The proposal was presented to the RPC community and  
 1571 approved to be used from now on. Technical drawings and instructions were provided.

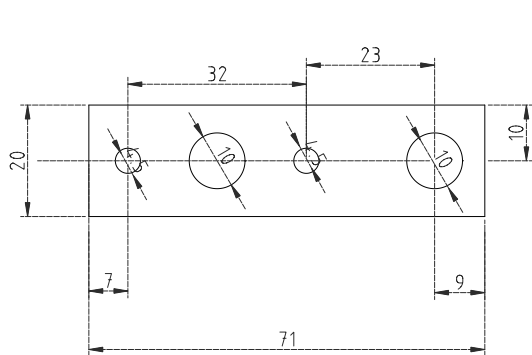


Figure 6.18: Left: Proposed adapter for the chamber patch panel which makes it possible to replace a tripolar by a jupiter HV connector. Right: Tryout of the proposed HV connector replacement.

## 1572 LV and control maintenance

1573 The low voltage (LV) and control maintenance consists in making sure that the Front-End Boards  
 1574 (FEBs) are powered and configurable, which means that the LV power system is working from  
 1575 supply board to the cable, that the signal cables are in good state and properly connected to the  
 1576 chamber and to the link boards and that the on-detector electronics (FEBs and Distribution Boards  
 1577 - DBs) are working fine.

1578 Usually, this system is very reliable. The weak point, in most of the cases, is the detector electronics.  
 1579 When a FEB [106] (as in Figure 6.19) is problematic it can present regions of very high noise or no  
 1580 signal at all (silent), which can not be recovered by the threshold control. In cases like this, when  
 1581 the FEB is accessible, it can be replaced in order to recover efficiency in the problematic chamber.  
 1582 This procedure is done by extracting the chamber from inside the detector (only for barrel chamber)  
 1583 and opening its cover to have access to the problematic component. Removed boards are sent back  
 1584 to production labs for refurbishment.

1585 The most usual problem is a chamber in which the threshold control was lost. For those chambers,  
 1586 most probably, the problem is in the distribution board of the chamber, which is a piece of hardware  
 1587 responsible for distributing the LV power to the FEBs (3 to 6 per chamber) and sending the threshold  
 1588 control signal to the FEBs via I2C line. If a chamber has no threshold control, it means that the  
 1589 RPC operation has no control over the signal selection, which can potentially induce performance  
 1590 issues.

1591 For the barrel this maintenance happens concomitantly with the gas leak reparations on the barrel  
 1592 chamber, since both demands the chamber extraction, which is a complex procedure in terms of  
 1593 operation and demands specialized equipment and manpower. For technical reasons, the gas leak  
 1594 extractions have precedence over LV ones.

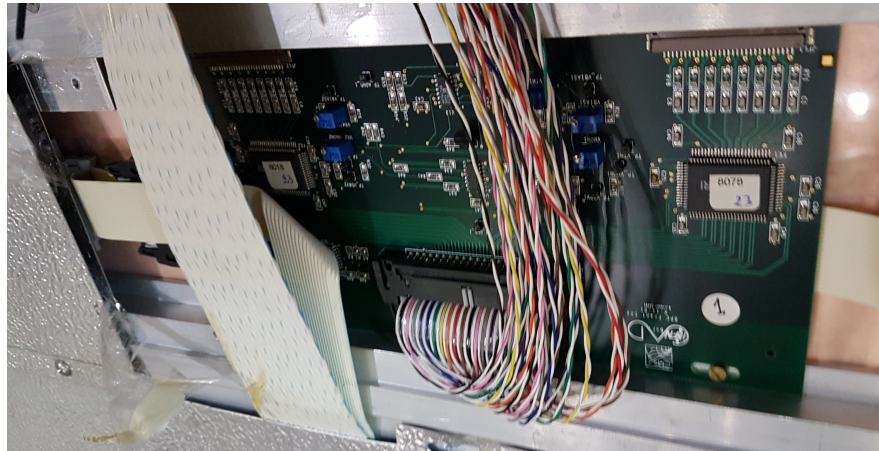


Figure 6.19: RPC Front-end board (FEB) used in the barrel chambers.

## 1595 Detector commissioning

1596 All the LS2 activities demands uncabling of the chamber to be repaired and possibly some neighbor  
 1597 chambers. Also, it can involve the replacement of components of the chamber. To avoid damage to  
 1598 the system a compromising procedure is needed after all this activities. Given the responsibilities  
 1599 of the commissioning it was necessary to: (a) make sure that the the RPC system keep tracks of all  
 1600 the interventions, (b) maintain all the algorithms used in the commissioning procedure, (c) together  
 1601 with the RPC Coordination, define a pool of people and a schedule to the commissioning of the  
 1602 system and (d) follow-up, with other CMS RPC experts, the availability of materials and resources  
 1603 for the commissioning operations.

1604 Besides the organizational tasks, the commissioning demanded to establish procedures to ensure the  
 1605 connectivity and functionality of HV and LV connections. For the HV, it is needed to make sure  
 1606 that the chambers are properly connected, without miscabling<sup>4</sup> and that the currents at stand-by  
 1607 HV and working point HV are compatible with the ones in the end of last data-taking (end of  
 1608 2018). This activity will start in November/2019, when the CMS RPC Standard Gas Mixture will  
 1609 be available again.

1610 For the LV point of view, the LV power cable and signal cables should also be properly connected,  
 1611 and presenting a noise profile compatible with last data-taking. One key point for this task is to  
 1612 make sure that that there are no miscabling of signal cable. One RPC chamber can have from 6  
 1613 to 18 signal cable, which are connected very close one to another. There is a good chance that a  
 1614 chamber, after reparation, have its signal cables mixed. In order to diagnose situations like this, it  
 1615 was validated a algorithm present in the RPC Online Software, but never used since LS1, which,  
 1616 by changing the threshold of each component of the RPC system, from very high to very low values  
 1617 (component by component), can spot miscabled chambers. Since the control line is independent of  
 1618 the signal line, a misclabeled will present a different noise from what is expected.

1619 Besides the validation of this algorithm, it was also implemented a web system (Figure 6.20),  
 1620 developed in Flask [107] wich automatize the execution of the algorithm, making transparent to the  
 1621 shifter (or the one performing the commissioning) the procedure to get miscabling report.

1622 The LV commissioning is ongoing, since it happens, as much as possible, right after the chamber  
 1623 reparation.

---

<sup>4</sup>Mixed cable connections.

### FEB Connectivity Test - Analysis

Worker	Date (YY-MM-DD)	Time (HH:MM:SS)	Hash	
RBP2_Far	2019-06-20	23:43:19	387534dst	<a href="#">Run Analyzer</a>
RBP1_Far	2019-06-20	20:12:20	458306dst	<a href="#">Run Analyzer</a>
RBP1_Far	2019-06-20	20:04:46	336162dst	<a href="#">Run Analyzer</a>
RBP1_Near	2019-06-20	19:02:00	377863dst	<a href="#">Run Analyzer</a>
RBP1_Near	2019-06-19	18:59:00	858950dst	<a href="#">Run Analyzer</a>
RBP1_Far	2019-06-19	18:58:26	994787dst	<a href="#">Run Analyzer</a>
YEN3_Far	2019-05-07	10:28:23	176278dst	<a href="#">Run Analyzer</a>
YEN3_Near	2019-05-07	10:28:08	347504dst	<a href="#">Run Analyzer</a>
YEN1_Far	2018-12-07	15:03:24	575561	<a href="#">Run Analyzer</a>
RB0_Far	2018-12-07	14:45:42	101463	<a href="#">Run Analyzer</a>
RBP1_Far	2018-12-07	09:12:00	477689	<a href="#">Run Analyzer</a>

Figure 6.20: RPC FEB Commissioning Analyzer.

DRAFT

<sub>1624</sub> 7 Conclusion

<sub>1625</sub> FAZER!

DRAFT

DRAFT

# 1626 Bibliography

- 1627 [1] Wikimedia Commons. *Standard Model*. 2020. URL: [https://en.wikipedia.org/wiki/File:Standard\\_Model\\_of\\_Elementary\\_Particles.svg](https://en.wikipedia.org/wiki/File:Standard_Model_of_Elementary_Particles.svg).
- 1628 [2] C. Patrignani et al. “Review of Particle Physics”. In: *Chin. Phys.* C40.10 (2016), p. 100001. DOI: 10.1088/1674-1137/40/10/100001.
- 1629 [3] A. Salam and J. C. Ward. “On a gauge theory of elementary interactions”. In: *Il Nuovo Cimento (1955-1965)* 19.1 (1961), pp. 165–170. DOI: 10.1007/BF02812723. URL: <https://doi.org/10.1007/BF02812723>.
- 1630 [4] G. Aad et al. “Observation of a new particle in the search for the Standard Model Higgs boson with the ATLAS detector at the LHC”. In: *Physics Letters B* 716.1 (2012), pp. 1–29. ISSN: 0370-2693. DOI: <https://doi.org/10.1016/j.physletb.2012.08.020>. URL: <http://www.sciencedirect.com/science/article/pii/S037026931200857X>.
- 1631 [5] Serguei Chatrchyan et al. “Observation of a new boson at a mass of 125 GeV with the CMS experiment at the LHC”. In: *Phys. Lett.* B716 (2012), pp. 30–61. DOI: 10.1016/j.physletb.2012.08.021. arXiv: 1207.7235 [hep-ex].
- 1632 [6] Geoffrey Bodwin et al. “Higgs boson decays to quarkonia and the  $H\bar{c}c$  coupling”. In: *Phys. Rev. D* 88 (5 Sept. 2013), p. 053003. DOI: 10.1103/PhysRevD.88.053003. URL: <https://link.aps.org/doi/10.1103/PhysRevD.88.053003>.
- 1633 [7] Geoffrey T. Bodwin et al. “Relativistic corrections to Higgs boson decays to quarkonia”. In: *Phys. Rev. D* 90 (11 Dec. 2014), p. 113010. DOI: 10.1103/PhysRevD.90.113010. URL: <https://link.aps.org/doi/10.1103/PhysRevD.90.113010>.
- 1634 [8] G. Aad, B. Abbott, et al. “Combined Measurement of the Higgs Boson Mass in  $pp$  Collisions at  $\sqrt{s} = 7$  and 8 TeV with the ATLAS and CMS Experiments”. In: *Phys. Rev. Lett.* 114 (19 May 2015), p. 191803. DOI: 10.1103/PhysRevLett.114.191803. URL: <https://link.aps.org/doi/10.1103/PhysRevLett.114.191803>.
- 1635 [9] Cédric Delaunay et al. “Enhanced Higgs boson coupling to charm pairs”. In: *Phys. Rev. D* 89 (3 Feb. 2014), p. 033014. DOI: 10.1103/PhysRevD.89.033014. URL: <https://link.aps.org/doi/10.1103/PhysRevD.89.033014>.
- 1636 [10] M. A. PÉREZ, G. TAVARES-VELASCO, and J. J. TOSCANO. “NEW PHYSICS EFFECTS IN RARE Z DECAYS”. In: *International Journal of Modern Physics A* 19.02 (2004), pp. 159–178. DOI: 10.1142/S0217751X04017100.
- 1637 [11] Grossman, Yuval and König, Matthias and Neubert, Matthias. “Exclusive radiative decays of W and Z bosons in QCD factorization”. In: *Journal of High Energy Physics* 2015.4 (Apr. 2015), p. 101. ISSN: 1029-8479. DOI: 10.1007/JHEP04(2015)101. URL: [https://doi.org/10.1007/JHEP04\(2015\)101](https://doi.org/10.1007/JHEP04(2015)101).
- 1638 [12] Geoffrey T. Bodwin et al. “Z-boson decays to a vector quarkonium plus a photon”. In: *Phys. Rev. D* 97 (1 Jan. 2018), p. 016009. DOI: 10.1103/PhysRevD.97.016009. URL: <https://link.aps.org/doi/10.1103/PhysRevD.97.016009>.
- 1639 [13] Geoffrey T. Bodwin et al. “Addendum: New approach to the resummation of logarithms in Higgs-boson decays to a vector quarkonium plus a photon [Phys. Rev. D 95, 054018 (2017)]”. In: *Phys. Rev. D* 96 (11 Dec. 2017), p. 116014. DOI: 10.1103/PhysRevD.96.116014. URL: <https://link.aps.org/doi/10.1103/PhysRevD.96.116014>.

- [14] Gino Isidori, Aneesh V. Manohar, and Michael Trott. “Probing the nature of the Higgs-like boson via  $h \rightarrow Vf$  decays”. In: *Physics Letters B* 728 (2014), pp. 131–135. ISSN: 0370-2693. DOI: <https://doi.org/10.1016/j.physletb.2013.11.054>. URL: <http://www.sciencedirect.com/science/article/pii/S037026931300960X>.
- [15] Alexander L. Kagan et al. “Exclusive Window onto Higgs Yukawa Couplings”. In: *Phys. Rev. Lett.* 114 (10 Mar. 2015), p. 101802. DOI: 10.1103/PhysRevLett.114.101802. URL: <https://link.aps.org/doi/10.1103/PhysRevLett.114.101802>.
- [16] Dao-Neng Gao. “A note on Higgs decays into Z boson and  $J/\psi(\Upsilon)$ ”. In: *Physics Letters B* 737 (2014), pp. 366–368. ISSN: 0370-2693. DOI: <https://doi.org/10.1016/j.physletb.2014.09.019>. URL: <http://www.sciencedirect.com/science/article/pii/S0370269314006698>.
- [17] A. M. Sirunyan et al. “Observation of Higgs Boson Decay to Bottom Quarks”. In: *Phys. Rev. Lett.* 121 (12 Sept. 2018), p. 121801. DOI: 10.1103/PhysRevLett.121.121801. URL: <https://link.aps.org/doi/10.1103/PhysRevLett.121.121801>.
- [18] G Apollinari et al. *High-Luminosity Large Hadron Collider (HL-LHC): Preliminary Design Report*. CERN Yellow Reports: Monographs. Geneva: CERN, 2015. DOI: 10.5170/CERN-2015-005. URL: <https://cds.cern.ch/record/2116337>.
- [19] The ATLAS Collaboration et al. “The ATLAS Experiment at the CERN Large Hadron Collider”. In: *Journal of Instrumentation* 3.08 (Aug. 2008), S08003–S08003. DOI: 10.1088/1748-0221/3/08/s08003. URL: <https://doi.org/10.1088%2F1748-0221%2F3%2F08%2Fs08003>.
- [20] G. Aad et al. “Search for Higgs and Z Boson Decays to  $J/\psi\gamma$  and  $\Upsilon(nS)\gamma$  with the ATLAS Detector”. In: *Phys. Rev. Lett.* 114 (12 Mar. 2015), p. 121801. DOI: 10.1103/PhysRevLett.114.121801. URL: <https://link.aps.org/doi/10.1103/PhysRevLett.114.121801>.
- [21] Morad Aaboud et al. “Searches for exclusive Higgs and Z boson decays into  $J/\psi\gamma$ ,  $\psi(2S)\gamma$ , and  $\Upsilon(nS)\gamma$  at  $\sqrt{s} = 13$  TeV with the ATLAS detector”. In: *Phys. Lett. B* 786 (2018), pp. 134–155. DOI: 10.1016/j.physletb.2018.09.024. arXiv: 1807.00802 [hep-ex].
- [22] S. Chatrchyan et al. “The CMS experiment at the CERN LHC”. In: *JINST* 3 (2008), S08004. DOI: 10.1088/1748-0221/3/08/S08004.
- [23] Albert M Sirunyan et al. “Search for rare decays of Z and Higgs bosons to  $J/\psi$  and a photon in proton-proton collisions at  $\sqrt{s} = 13$  TeV”. In: *Eur. Phys. J.* C79.2 (2019), p. 94. DOI: 10.1140/epjc/s10052-019-6562-5. arXiv: 1810.10056 [hep-ex].
- [24] Albert M Sirunyan et al. “Search for Higgs and Z boson decays to  $J/\psi$  or  $\Upsilon$  pairs in proton-proton collisions at  $\sqrt{s} = 13$  TeV”. In: *Phys. Lett. B* 797.arXiv:1905.10408. CMS-HIG-18-025-003 (May 2019). All figures and tables can be found at <http://cms-results.web.cern.ch/cms-results/public-results/publications/HIG-18-025> (CMS Public Pages), 134811. 31 p. DOI: 10.1016/j.physletb.2019.134811. URL: <https://cds.cern.ch/record/2676242>.
- [25] Albert M. Sirunyan et al. “Observation of the  $Z \rightarrow \psi\ell^+\ell^-$  decay in pp collisions at  $\sqrt{s} = 13$  TeV”. In: *Phys. Rev. Lett.* 121.arXiv:1806.04213. CMS-BPH-16-001-003 (June 2018). Submitted to *Phys.Rev.Lett.*, 141801. 17 p. DOI: 10.1103/PhysRevLett.121.141801. URL: <https://cds.cern.ch/record/2623687>.
- [26] S. Chatrchyan et al. “The CMS experiment at the CERN LHC”. In: *JINST* 3 (2008), S08004. DOI: 10.1088/1748-0221/3/08/S08004.
- [27] Serguei Chatrchyan et al. “Description and performance of track and primary-vertex reconstruction with the CMS tracker”. In: *JINST* 9 (2014), P10009. DOI: 10.1088/1748-0221/9/10/P10009. arXiv: 1405.6569 [physics.ins-det].
- [28] Vardan Khachatryan et al. “Performance of electron reconstruction and selection with the CMS detector in proton-proton collisions at  $\sqrt{s} = 8$  TeV”. In: *JINST* 10 (2015), P06005. DOI: 10.1088/1748-0221/10/06/P06005. arXiv: 1502.02701 [physics.ins-det].
- [29] Vardan Khachatryan et al. “Performance of photon reconstruction and identification with the CMS detector in proton-proton collisions at  $\sqrt{s} = 8$  TeV”. In: *JINST* 10 (2015), P08010. DOI: 10.1088/1748-0221/10/08/P08010. arXiv: 1502.02702 [physics.ins-det].

- [30] A M Sirunyan et al. “Performance of the CMS muon detector and muon reconstruction with proton-proton collisions at  $\sqrt{s} = 13$  TeV”. In: *JINST* 13 (2018), P06015. DOI: 10.1088/1748-0221/13/06/P06015. arXiv: 1804.04528 [physics.ins-det].
- [31] Vardan Khachatryan et al. “The CMS trigger system”. In: *JINST* 12 (2017), P01020. DOI: 10.1088/1748-0221/12/01/P01020. arXiv: 1609.02366 [physics.ins-det].
- [32] *CMS Luminosity Measurements for the 2016 Data Taking Period*. Tech. rep. CMS-PAS-LUM-17-001. Geneva: CERN, 2017. URL: <https://cds.cern.ch/record/2257069>.
- [33] S. Agostinelli et al. “GEANT4—a simulation toolkit”. In: A506 (2003), pp. 250–303. DOI: 10.1016/S0168-9002(03)01368-8.
- [34] Paolo Nason. “A New method for combining NLO QCD with shower Monte Carlo algorithms”. In: *JHEP* 11 (2004), p. 040. DOI: 10.1088/1126-6708/2004/11/040. arXiv: hep-ph/0409146 [hep-ph].
- [35] Stefano Frixione, Paolo Nason, and Carlo Oleari. “Matching NLO QCD computations with Parton Shower simulations: the POWHEG method”. In: *JHEP* 11 (2007), p. 070. DOI: 10.1088/1126-6708/2007/11/070. arXiv: 0709.2092 [hep-ph].
- [36] Simone Alioli et al. “A general framework for implementing NLO calculations in shower Monte Carlo programs: the POWHEG BOX”. In: *JHEP* 06 (2010), p. 043. DOI: 10.1007/JHEP06(2010)043. arXiv: 1002.2581 [hep-ph].
- [37] Abdelhak Djouadi. “The anatomy of electroweak symmetry breaking: Tome I: The Higgs boson in the Standard Model”. In: *Physics Reports* 457.1 (2008), pp. 1–216. ISSN: 0370-1573. DOI: <https://doi.org/10.1016/j.physrep.2007.10.004>. URL: <http://www.sciencedirect.com/science/article/pii/S0370157307004334>.
- [38] Torbjörn Sjöstrand, Stephen Mrenna, and Peter Skands. “A brief introduction to PYTHIA 8.1”. In: *Computer Physics Communications* 178.11 (2008), pp. 852–867. ISSN: 0010-4655. DOI: <https://doi.org/10.1016/j.cpc.2008.01.036>. URL: <http://www.sciencedirect.com/science/article/pii/S0010465508000441>.
- [39] Torbjörn Sjöstrand et al. “An Introduction to PYTHIA 8.2”. In: *Comput. Phys. Commun.* 191 (2015), pp. 159–177. DOI: 10.1016/j.cpc.2015.01.024. arXiv: 1410.3012 [hep-ph].
- [40] Vardan Khachatryan et al. “Event generator tunes obtained from underlying event and multiparton scattering measurements”. In: *Eur. Phys. J. C*76.3 (2016), p. 155. DOI: 10.1140/epjc/s10052-016-3988-x. arXiv: 1512.00815 [hep-ex].
- [41] The NNPDF collaboration et al. “Parton distributions for the LHC run II”. In: *Journal of High Energy Physics* 2015.4 (Apr. 2015), p. 40. ISSN: 1029-8479. DOI: 10.1007/JHEP04(2015)040. URL: [https://doi.org/10.1007/JHEP04\(2015\)040](https://doi.org/10.1007/JHEP04(2015)040).
- [42] J. Alwall et al. “The automated computation of tree-level and next-to-leading order differential cross sections, and their matching to parton shower simulations”. In: *Journal of High Energy Physics* 2014.7 (July 2014), p. 79. ISSN: 1029-8479. DOI: 10.1007/JHEP07(2014)079. URL: [https://doi.org/10.1007/JHEP07\(2014\)079](https://doi.org/10.1007/JHEP07(2014)079).
- [43] Ali Abbasabadi et al. “Radiative Higgs boson decays  $H \rightarrow f\bar{f}\gamma$ ”. In: *Phys. Rev. D* 55 (9 May 1997), pp. 5647–5656. DOI: 10.1103/PhysRevD.55.5647. URL: <https://link.aps.org/doi/10.1103/PhysRevD.55.5647>.
- [44] D. de Florian et al. *Handbook of LHC Higgs Cross Sections: 4. Deciphering the Nature of the Higgs Sector*. CERN Yellow Reports: Monographs. 869 pages, 295 figures, 248 tables and 1645 citations. Working Group web page: <https://twiki.cern.ch/twiki/bin/view/LHCPhysics/LHCHXSWG>. Oct. 2016. DOI: 10.23731/CYRM-2017-002. URL: <https://cds.cern.ch/record/2227475>.
- [45] Ye Li and Frank Petriello. “Combining QCD and electroweak corrections to dilepton production in the framework of the FEWZ simulation code”. In: *Phys. Rev. D* 86 (9 Nov. 2012), p. 094034. DOI: 10.1103/PhysRevD.86.094034. URL: <https://link.aps.org/doi/10.1103/PhysRevD.86.094034>.

- [46] John M. Campbell and R.K. Ellis. “MCFM for the Tevatron and the LHC”. In: *Nuclear Physics B - Proceedings Supplements* 205-206 (2010). Loops and Legs in Quantum Field Theory, pp. 10–15. ISSN: 0920-5632. DOI: <https://doi.org/10.1016/j.nuclphysbps.2010.08.011>. URL: <http://www.sciencedirect.com/science/article/pii/S0920563210001945>.
- [47] Vardan Khachatryan et al. “Search for a Higgs boson decaying into  $\gamma^*\gamma \rightarrow \ell\ell\gamma$  with low dilepton mass in pp collisions at  $\sqrt{s} = 8$  TeV”. In: *Phys. Lett. B* 753 (2016), pp. 341–362. DOI: [10.1016/j.physletb.2015.12.039](https://doi.org/10.1016/j.physletb.2015.12.039). arXiv: 1507.03031 [hep-ex].
- [48] N. Brambilla, S. Eidelman, B.K. Heltsley, et al. “Heavy quarkonium: progress, puzzles, and opportunities”. In: *The European Physical Journal C* 71.2 (Feb. 2011), p. 1534. ISSN: 1434-6052. DOI: [10.1140/epjc/s10052-010-1534-9](https://doi.org/10.1140/epjc/s10052-010-1534-9). URL: <https://doi.org/10.1140/epjc/s10052-010-1534-9>.
- [49] Sandro Palestini. “Angular distribution and rotations of frame in vector meson decays into lepton pairs”. In: *Phys. Rev. D* 83 (3 Feb. 2011), p. 031503. DOI: [10.1103/PhysRevD.83.031503](https://doi.org/10.1103/PhysRevD.83.031503). URL: <https://link.aps.org/doi/10.1103/PhysRevD.83.031503>.
- [50] A.M. Sirunyan et al. “Particle-flow reconstruction and global event description with the CMS detector”. In: *Journal of Instrumentation* 12.10 (2017), P10003. URL: <http://stacks.iop.org/1748-0221/12/i=10/a=P10003>.
- [51] Matteo Cacciari, Gavin P. Salam, and Gregory Soyez. “The anti- $k_t$  jet clustering algorithm”. In: *JHEP* 04 (2008), p. 063. DOI: [10.1088/1126-6708/2008/04/063](https://doi.org/10.1088/1126-6708/2008/04/063). arXiv: 0802.1189 [hep-ex].
- [52] Matteo Cacciari, Gavin P. Salam, and Gregory Soyez. “FastJet User Manual”. In: *Eur. Phys. J. C* 72 (2012), p. 1896. DOI: [10.1140/epjc/s10052-012-1896-2](https://doi.org/10.1140/epjc/s10052-012-1896-2). arXiv: 1111.6097 [hep-ph].
- [53] Albert M Sirunyan et al. “Measurements of properties of the Higgs boson decaying into the four-lepton final state in pp collisions at  $\sqrt{s} = 13$  TeV”. In: *JHEP* 11 (2017), p. 047. DOI: [10.1007/JHEP11\(2017\)047](https://doi.org/10.1007/JHEP11(2017)047). arXiv: 1706.09936 [hep-ex].
- [54] V. Khachatryan et al. “Observation of the diphoton decay of the Higgs boson and measurement of its properties”. In: *The European Physical Journal C* 74.10 (Oct. 2014), p. 3076. ISSN: 1434-6052. DOI: [10.1140/epjc/s10052-014-3076-z](https://doi.org/10.1140/epjc/s10052-014-3076-z). URL: <https://doi.org/10.1140/epjc/s10052-014-3076-z>.
- [55] S. Bernstein. “Démonstration du théorème de Weierstrass fondée sur le calcul des probabilités”. In: *Commun. Soc. Math. Kharkov* 13.1–2 (1912).
- [56] John Erthal Gaiser. “Charmonium Spectroscopy From Radiative Decays of the  $J/\psi$  and  $\psi'$ ”. PhD thesis. SLAC, 1982. URL: <http://www-public.slac.stanford.edu/sciDoc/docMeta.aspx?slacPubNumber=slac-r-255.html>.
- [57] P. D. Dauncey et al. “Handling uncertainties in background shapes: the discrete profiling method”. In: *JINST* 10.04 (2015), P04015. DOI: [10.1088/1748-0221/10/04/P04015](https://doi.org/10.1088/1748-0221/10/04/P04015). arXiv: 1408.6865 [physics.data-an].
- [58] S. S. Wilks. “The Large-Sample Distribution of the Likelihood Ratio for Testing Composite Hypotheses”. In: *Ann. Math. Statist.* 9.1 (Mar. 1938), pp. 60–62. DOI: [10.1214/aoms/1177732360](https://doi.org/10.1214/aoms/1177732360). URL: <https://doi.org/10.1214/aoms/1177732360>.
- [59] Higgs to Gamma Gamma Working Group. *Further measurement of  $H \rightarrow \gamma\gamma$  at  $\sqrt{13}$  TeV*. CMS Note 2016/209. CERN, 2016. URL: [http://cms.cern.ch/icMS/jsp/db\\_notes/noteInfo.jsp?cmsnoteid=CMS%20AN-2016/209](http://cms.cern.ch/icMS/jsp/db_notes/noteInfo.jsp?cmsnoteid=CMS%20AN-2016/209).
- [60] *Updated measurements of Higgs boson production in the diphoton decay channel at  $\sqrt{s} = 13$  TeV in pp collisions at CMS*. Tech. rep. CMS-PAS-HIG-16-020. Geneva: CERN, 2016. URL: <http://cds.cern.ch/record/2205275>.
- [61] D. de Florian et al. “Handbook of LHC Higgs Cross Sections: 4. Deciphering the Nature of the Higgs Sector”. In: (2016). DOI: [10.23731/CYRM-2017-002](https://doi.org/10.23731/CYRM-2017-002). arXiv: 1610.07922 [hep-ph].
- [62] Jon Butterworth et al. “PDF4LHC recommendations for LHC Run II”. In: *J. Phys. G* 43 (2016), p. 023001. DOI: [10.1088/0954-3899/43/2/023001](https://doi.org/10.1088/0954-3899/43/2/023001). arXiv: 1510.03865 [hep-ph].

- [63] A. D. Martin et al. “Parton distributions for the LHC”. In: *Eur. Phys. J.* C63 (2009), pp. 189–285. DOI: 10.1140/epjc/s10052-009-1072-5. arXiv: 0901.0002 [hep-ph].
- [64] Hung-Liang Lai et al. “New parton distributions for collider physics”. In: *Phys. Rev.* D82 (2010), p. 074024. DOI: 10.1103/PhysRevD.82.074024. arXiv: 1007.2241 [hep-ph].
- [65] Sergey Alekhin et al. “The PDF4LHC Working Group Interim Report”. In: (2011). arXiv: 1101.0536 [hep-ph].
- [66] Michiel Botje et al. “The PDF4LHC Working Group Interim Recommendations”. In: (2011). arXiv: 1101.0538 [hep-ph].
- [67] Richard D. Ball et al. “Impact of Heavy Quark Masses on Parton Distributions and LHC Phenomenology”. In: *Nucl. Phys.* B849 (2011), pp. 296–363. DOI: 10.1016/j.nuclphysb.2011.03.021. arXiv: 1101.1300 [hep-ph].
- [68] Giampiero Passarino. “Higgs Boson Production and Decay: Dalitz Sector”. In: *Phys. Lett.* B727 (2013), pp. 424–431. DOI: 10.1016/j.physletb.2013.10.052. arXiv: 1308.0422 [hep-ph].
- [69] A.M. Sirunyan et al. “Performance of the CMS muon detector and muon reconstruction with proton-proton collisions at  $\sqrt{s}=13$  TeV”. In: *Journal of Instrumentation* 13.06 (June 2018), P06015–P06015. DOI: 10.1088/1748-0221/13/06/p06015. URL: <https://doi.org/10.1088%2F1748-0221%2F13%2F06%2Fp06015>.
- [70] Vardan Khachatryan et al. “Performance of photon reconstruction and identification with the CMS detector in proton-proton collisions at  $\sqrt{s} = 8$  TeV”. In: *JINST* 10.CMS-EGM-14-001. CMS-EGM-14-001. CERN-PH-EP-2015-006 (Feb. 2015). Comments: Submitted to JINST, P08010. 59 p. DOI: 10.1088/1748-0221/10/08/P08010. URL: <http://cds.cern.ch/record/1988093>.
- [71] A L Read. “Presentation of search results: the CL<sub>s</sub> technique”. In: *Journal of Physics G: Nuclear and Particle Physics* 28.10 (Sept. 2002), pp. 2693–2704. DOI: 10.1088/0954-3899/28/10/313. URL: <https://doi.org/10.1088%2F0954-3899%2F28%2F10%2F313>.
- [72] J. Neyman and E. S. Pearson. “On the Problem of the Most Efficient Tests of Statistical Hypotheses”. In: *Philosophical Transactions of the Royal Society of London. Series A, Containing Papers of a Mathematical or Physical Character* 231 (1933), pp. 289–337. ISSN: 02643952. URL: <http://www.jstor.org/stable/91247>.
- [73] Glen Cowan et al. “Asymptotic formulae for likelihood-based tests of new physics”. In: *The European Physical Journal C* 71.2 (Feb. 2011), p. 1554. ISSN: 1434-6052. DOI: 10.1140/epjc/s10052-011-1554-0. URL: <https://doi.org/10.1140/epjc/s10052-011-1554-0>.
- [74] *Procedure for the LHC Higgs boson search combination in Summer 2011*. Tech. rep. CMS-NOTE-2011-005. ATL-PHYS-PUB-2011-11. Geneva: CERN, Aug. 2011. URL: <https://cds.cern.ch/record/1379837>.
- [75] David H. Annis. “Kendall’s Advanced Theory of Statistics, Vol. 1: Distribution Theory (6th ed.). Alan Stuart and J. Keith Ord; Kendall’s Advanced Theory of Statistics, Vol. 2A: Classical Inference and the Linear Model (6th ed.). Alan Stuart and J. Keith Ord, and Steven F. Arnold”. In: *Journal of the American Statistical Association* 101 (2006), pp. 1721–1721. URL: <https://EconPapers.repec.org/RePEc:bes:jnlasa:v:101:y:2006:p:1721-1721>.
- [76] *Procedure for the LHC Higgs boson search combination in Summer 2011*. Tech. rep. CMS-NOTE-2011-005. ATL-PHYS-PUB-2011-11. Geneva: CERN, Aug. 2011. URL: <https://cds.cern.ch/record/1379837>.
- [77] M. Aaboud et al. “Searches for exclusive Higgs and Z boson decays into  $J/\psi\gamma$ ,  $\psi(2S)\gamma$ , and  $\Upsilon(nS)\gamma$  at  $\sqrt{s} = 13$  TeV with the ATLAS detector”. In: *Physics Letters B* 786 (Nov. 2018), pp. 134–155. ISSN: 0370-2693. DOI: 10.1016/j.physletb.2018.09.024. URL: <http://dx.doi.org/10.1016/j.physletb.2018.09.024>.
- [78] R. Santonico and R. Cardarelli. “Development of resistive plate counters”. In: *Nuclear Instruments and Methods in Physics Research* 187.2 (1981), pp. 377–380. ISSN: 0167-5087. DOI:

- 1869 https://doi.org/10.1016/0029-554X(81)90363-3. URL: http://www.sciencedirect.com/science/article/pii/0029554X81903633.

1870 [79] Marcello Abbrescia, Paulo Fonte, and Vladimir Peskov. *Resistive gaseous detectors: designs, performance, and perspectives*. Weinheim: Wiley-VCH, 2018. DOI: 10.1002/9783527698691.

1871 [80] A Beroual and I Fofana. "The background of air gap discharge theory". In: *Discharge in Long Air Gaps*. 2053-2563. IOP Publishing, 2016, 2-1 to 2-22. ISBN: 978-0-7503-1236-3. DOI: 10.1088/978-0-7503-1236-3ch2. URL: http://dx.doi.org/10.1088/978-0-7503-1236-3ch2.

1872 [81] Leonard B. Loeb and John M. Meek. "The Mechanism of Spark Discharge in Air at Atmospheric Pressure. I". In: *Journal of Applied Physics* 11.6 (1940), pp. 438–447. DOI: 10.1063/1.1712792. eprint: https://doi.org/10.1063/1.1712792. URL: https://doi.org/10.1063/1.1712792.

1873 [82] *The CMS muon project: Technical Design Report*. Technical Design Report CMS. Geneva: CERN, 1997. URL: https://cds.cern.ch/record/343814.

1874 [83] Dong Hyun, Kim. "Work on CMS Muon Detector (RPC) during Long Shutdown 1 (LS1) - Point 5, Cessy, CMS cavern". CMS Collection. May 2015. URL: https://cds.cern.ch/record/2016815.

1875 [84] P. Bernardini et al. "Precise measurements of drift velocities in helium gas mixtures". In: *Nuclear Instruments and Methods in Physics Research Section A: Accelerators, Spectrometers, Detectors and Associated Equipment* 355.2 (1995), pp. 428–433. ISSN: 0168-9002. DOI: https://doi.org/10.1016/0168-9002(94)01144-3. URL: http://www.sciencedirect.com/science/article/pii/0168900294011443.

1876 [85] E. Gorini et al. "Drift velocity measurements in C2H2F4 based mixtures". In: *Proceedings of the 4th International Workshop on Resistive Plate Chamber and Related Detectors, in Napoli, Italy, 15-16 October* (1997).

1877 [86] G. Bressi et al. "AN APPARATUS TO SEARCH FOR FREE NEUTRON ANTI-NEUTRON OSCILLATIONS". In: *Nucl. Instrum. Meth. A* 261 (1987), pp. 449–461. DOI: 10.1016/0168-9002(87)90353-6.

1878 [87] H.L. Ge et al. "The production of residual nuclides in Pb irradiated by 400 MeV/u carbon ions". In: *Nucl. Instrum. Meth. B* 337 (2014), pp. 34–38. DOI: 10.1016/j.nimb.2014.07.024.

1879 [88] M. Abbrescia et al. "A Horizontal muon telescope implemented with resistive plate chambers". In: *Nucl. Instrum. Meth. A* 336 (1993), pp. 322–329. DOI: 10.1016/0168-9002(93)91116-5.

1880 [89] L. Antoniazzi et al. "The E771 RPC muon detector". In: *Nucl. Instrum. Meth. A* 315 (1992), pp. 92–94. DOI: 10.1016/0168-9002(92)90686-X.

1881 [90] A. Di Ciaccio et al. "Muon tracking and hadron punchthrough measurements using resistive plate chambers". In: *Nucl. Instrum. Meth. A* 315 (1992), pp. 102–108. DOI: 10.1016/0168-9002(92)90688-Z.

1882 [91] R. de Asmundis. "Performances of the RPC trigger system in the L3 experiment". In: *3rd International Workshop on Resistive Plate Chambers and Related Detectors (RPC 95)*. 1995, pp. 139–155.

1883 [92] D. Boutigny et al. "BaBar technical design report". In: (Mar. 1995).

1884 [93] Andrea Gelmi. *Longevity studies for the CMS-RPC system*. Tech. rep. CMS-CR-2018-136. Geneva: CERN, July 2018. URL: https://cds.cern.ch/record/2634505.

1885 [94] M.A. Shah et al. "Experiences from the RPC data taking during the CMS RUN-2". In: *15th Workshop on Resistive Plate Chambers and Related Detectors*. May 2020. arXiv: 2005.12532 [physics.ins-det].

1886 [95] *Public CMS Data Quality Information*. twiki.cern.ch/twiki/bin/view/CMSPublic/DataQuality. Acessado em: 20/02/2018.

1887 [96] Johannes Guteleber, Steven Murray, and Luciano Orsini. "Towards a homogeneous architecture for high-energy physics data acquisition systems". In: *Computer Physics Communications* 153.2 (2003), pp. 155–163. ISSN: 0010-4655. DOI: https://doi.org/10.1016/

- 1920 S0010-4655(03)00161-9. URL: <http://www.sciencedirect.com/science/article/pii/S0010465503001619>.
- 1921 [97] *Dojo*. <https://dojotoolkit.org/>. Acessado em: 20/02/2018.
- 1922 [98] *Polymer Project*. Acessado em: 20/02/2018.
- 1923 [99] M. I. Pedraza-Morales. *RPC upgrade project for CMS Phase II*. 2018. arXiv: 1806.11503 [physics.ins-det].
- 1924 [100] Dorothea Pfeiffer et al. “The radiation field in the Gamma Irradiation Facility GIF++ at CERN”. In: *Nuclear Instruments and Methods in Physics Research Section A: Accelerators, Spectrometers, Detectors and Associated Equipment* 866 (2017), pp. 91–103. ISSN: 0168-9002. DOI: <https://doi.org/10.1016/j.nima.2017.05.045>. URL: <http://www.sciencedirect.com/science/article/pii/S0168900217306113>.
- 1925 [101] A. Augusto Alves Jr. et al. “The LHCb Detector at the LHC”. In: *JINST* 3 (2008), S08005. DOI: 10.1088/1748-0221/3/08/S08005.
- 1926 [102] Georges Charpak et al. “The Use of Multiwire Proportional Counters to Select and Localize Charged Particles”. In: *Nucl. Instrum. Meth.* 62 (1968), pp. 262–268. DOI: 10.1016/0029-554X(68)90371-6.
- 1927 [103] *LHCb Muon Group Home Page*. [Online; accessed 1-October-2019]. 2019. URL: <http://lhcb-muon.web.cern.ch/lhcb-muon/>.
- 1928 [104] *CAEN Programmable Logic Unit - V2495*. [Online; accessed 1-October-2019]. 2019. URL: <https://www.caen.it/products/v2495/>.
- 1929 [105] *Resistive Plate Chambers are getting dolled up*. <https://cms.cern/news/resistive-plate-chambers-are-getting-dolled>. Acessado em: 20/09/2019.
- 1930 [106] C. Binetti et al. “A new Front-End board for RPC detector of CMS”. In: (Sept. 1999).
- 1931 [107] *Flask (web framework)*. [Online; accessed 1-October-2019]. 2019. URL: <https://palletsprojects.com/p/flask/>.